Volume 69A
Number 3
May–June 1965

# Physics and Chemistry

U.S. DEPARTMENT OF COMMERCE

SECTION A

## JOURNAL OF RESEARCH

NATIONAL BUREAU OF STANDARDS

**Journal of Research**

**of the**

**National Bureau of Standards**

A. Physics and Chemistry

May–June • 1965

VOLUME • 69A

NUMBER • 3

Editor: C. W. Beckett

Associate Editors: D. D. Wagman
J. M. Richardson

Publication dates:
Feb. 1, Apr. 1, June 1, Aug. 1, Oct. 1, Dec. 1, 1965

**JOURNAL OF RESEARCH**

The National Bureau of Standards Journal of Research reports research and development in the fields of activity shown at right. Also included from time to time are survey articles on topics closely related to the Bureau's scientific and technical program.

The Journal is published in four separate sections as follows:

**A. Physics and Chemistry**

Contains papers of interest primarily to scientists working in these fields. Issued six times a year. Annual subscription: domestic, $4.00; foreign, $4.75. Single copy, 70c.

**B. Mathematics and Mathematical Physics**

Presents studies and compilations designed mainly for the mathematician and the theoretical physicist. Issued quarterly. Annual subscription: domestic, $2.25; foreign, $2.75. Single copy, 75c.

**C. Engineering and Instrumentation**

Reports research and development results of interest chiefly to the engineer and the applied scientist. Issued quarterly. Annual subscription: domestic, $2.25; foreign, $2.75. Single copy, 75c.

**D. Radio Science (formerly Radio Propagation)**

Published in cooperation with U.S. National Committee of URSI. Presents papers in radio propagation, communications, and radio science generally. Issued monthly. Annual subscription: domestic, $9.00; foreign, $11.50. Single copy, $1.00.

**The National Bureau of Standards** is a principal focal point in the Federal Government for assuring maximum application of the physical and engineering sciences to the advancement of technology in industry and commerce. Its responsibilities include development and maintenance of the national standards of measurement, and the provision of means for making measurements consistent with those standards; determination of physical constants and properties of materials; development of methods for testing materials, mechanisms, and structures, and making such tests as may be necessary, particularly for government agencies; cooperation in the establishment of standard practices for incorporation in codes and specifications; advisory service to government agencies on scientific and technical problems; invention and development of devices to serve special needs of the Government; assistance to industry, business and consumers in the development and acceptance of commercial standards and simplified trade practice recommendations; administration of programs in cooperation with United States business groups and standards organizations for the development of international standards of practice; and maintenance of a clearinghouse for the collection and dissemination of scientific, technical, and engineering information.

**Institute for Basic Standards.** Electricity. Metrology. Heat. Radiation Physics. Mechanics. Applied Mathematics. Atomic Physics. Physical Chemistry. Laboratory Astrophysics.* Radio Standards Laboratory: Radio Standards Physics; Radio Standards Engineering.** Office of Standard Reference Data.

**Institute for Materials Research.** Analytical Chemistry. Polymers. Metallurgy. Inorganic Materials. Reactor Radiations. Cryogenics.** Office of Standard Reference Materials.

**Central Radio Propagation Laboratory.**** Ionosphere Research and Propagation. Troposphere and Space Communications. Radio Systems. Upper Atmosphere and Space Physics.

**Institute for Applied Technology.** Textiles and Apparel Technology Center. Building Research. Industrial Equipment. Information Technology. Performance Test Development. Instrumentation. Transport Systems. Office of Technical Services. Office of Weights and Measures. Office of Engineering Standards. Office of Industrial Services.

*NBS Group, Joint Institute for Laboratory Astrophysics at the University of Colorado.
**Located at Boulder, Colo.

U.S. DEPARTMENT OF COMMERCE
John T. Connor, Secretary

NATIONAL BUREAU OF STANDARDS
A. V. Astin, Director

Order all publications from the Superintendent of Documents
U.S. Government Printing Office, Washington, D.C., 20402

Use of funds for printing this publication approved by the Director of the Bureau of the Budget (June 19, 1961).

JOURNAL OF RESEARCH of the National Bureau of Standards—A. Physics and Chemistry
Vol. 69A, No. 3, May–June 1965

# Electronic Structure and Magnetic Properties of the Neptunyl Ion

J. C. Eisenstein and M. H. L. Pryce[1]

(December 29, 1964)

The magnetic and spectroscopic properties of the neptunyl ion are reconsidered. The effect on the energy levels of covalency is discussed. New values for the parameters of our earlier theory are obtained, the analysis being based on more recent spectroscopic data and arguments concerning the relative widths and intensities of the optical absorption peaks. $g$-values and the temperature independent susceptibility are calculated and the results compared with experimental values. Experiments which need to be done to confirm various parts of the theory are suggested.

## 1. Introduction

Several years ago we [1][2] published two papers (to be referred to here as I and II), on the properties of uranyl-like ions. Our interpretation of the experimental data was based on a specific model for these ions. We assumed that the uranium atom lies between, and equidistant from, the two oxygen atoms, the uranyl ion as a whole being predominantly covalently bonded. The ligand field, which is due to the bonding electrons, was assumed to be strong in comparison with the electrostatic field, which is due to neighboring ions or molecules.

Since 1956 important new spectroscopic measurements have been reported [2, 3]. The new data do not require any revision in our model or in our general assumptions about the model. However, they do require rather large changes in the parameters of our theory such as the spin-orbit coupling constant, the coulomb integrals and the strength of the ligand field.

In this paper and in a future paper on plutonyl a more complete discussion of the properties of the uranyl-like ions than appeared in our previous papers will be given. The object is not so much to present the revised values of the parameters as it is to discuss the numerous hypotheses which were made in attempting to understand the properties of these ions. Some of the things touched on in this paper are the most physically significant way of plotting an absorption spectrum, the interpretation of line widths, the possibility of fitting Gaussian curves to an unresolved spectrum, the excitation of vibrations, and the effects of covalent bond formation. The discussion of the general problems involved in understanding the behavior of uranyl-type ions is undoubtedly relevant to the interpretation of the properties of transition group compounds and other actinide compounds.

One of our most important contributions here is the revealing of the complexity of the uranyl-type ions. For the neptunyl ion one can calculate exactly the positions of the energy levels for a variety of physically likely perturbations. The spectrum has been determined with sufficient accuracy so that one knows the experimental positions of the energy levels (except for uncertainties to be discussed). Consequently one can determine whether the likely perturbations are, or are not, adequate to account for the spectroscopic properties. A similar remark applies to the magnetic properties.

The available absorption spectra are those of neptunyl ions in water (or heavy water) and acid (commonly $HClO_4$). The magnetic resonance data are for crystalline rubidium neptunyl

[1] Present address: Department of Physics, University of Southern California.

[2] Figures in brackets indicate the literature references at the end of this paper.



766-033 O - 65 - 2

nitrate diluted with the isomorphous uranyl salt. The susceptibility data are for crystalline sodium neptunyl acetate. It is therefore necessary to consider the neptunyl ion in different environments. That the environment can play a vital part is to be seen from I, where it is shown that the field $V_6^6$, due to the surrounding ions in the double nitrate, is responsible for the nonzero $g_\perp$, and contributes to reduce $g_{||}$ from 4.0 to 3.4. If the environment of the ion had a different symmetry, say a four-fold instead of a three-fold axis, the resonance behavior would be different; and if the ion were isolated, $g_\perp$ would be zero.

In our initial attempts to understand the solution absorption spectrum we paid no attention to the ionic environment (solvation sphere), but it now appears that this omission was unjustified. We are therefore led to the question:— what is the immediate environment?

In many crystals whose structure is known such as rubidium uranyl nitrate and sodium uranyl acetate the uranyl ion is surrounded by six oxygen atoms in an equatorial, hexagonal puckered ring. In sodium uranyl acetate, e.g., six oxygen atoms from three different acetate groups are almost coplanar with the uranium ion; in the (slightly) puckered oxygen ring there are two different O—O distances [4]. Therefore it is reasonable to assume that in solution the uranyl ion is surrounded by six water molecules in a puckered ring. Such a system gives rise to a "crystalline" field with approximately three-fold symmetry. The axially symmetric components $V_2^0$, $V_4^0$, and $V_6^0$ of the "crystalline" field add to the ligand field of the ion itself, and modify the energy levels. The components $V_4^3$, $V_6^3$ and $V_6^6$ of the "crystalline" field mix the zero-order states which correspond to different axial quantum numbers, and lead to small changes in the energy levels. They also play a part in the selection rules for optical absorption.

There are also fluctuating deviations from these symmetric fields, which play a very important part in absorption by inducing electric dipole transitions.

In our earlier study of the spectrum we concentrated on the positions of the absorption bands and paid little attention to their strengths and widths. Since then a good deal of work has been published on the absorption spectra of compounds of transition elements, and the factors which determine strength and width are much more clearly understood. This work has furnished a number of important clues for the interpretation of the actinide spectra, most particularly for plutonyl.

## 2. Energy Levels and Absorption Spectrum of Neptunyl

The experimental absorption spectrum of Np (VI) is shown in figures 1 and 2 where Waggener's data are replotted as a function of wave number rather than wavelength. In addition we have used as ordinate the quantity 6900 $\epsilon\lambda$ in place of the molar extinction coefficient. It is shown in

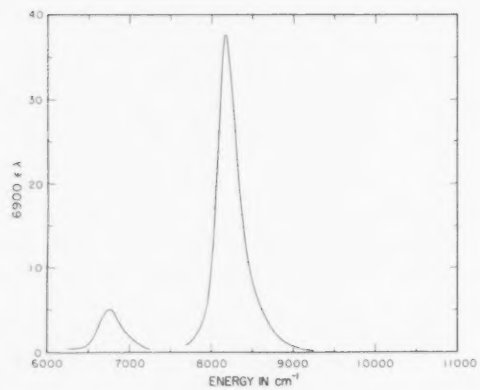


FIGURE 1. *Absorption spectrum of the* $(N_pO_2)^{++}$ *ion from 6000 to 11000* $cm^{-1}$.

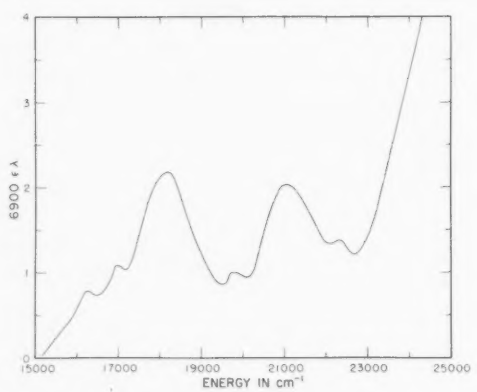


FIGURE 2. *Absorption spectrum of the* $(N_pO_2)^{++}$ *ion from 15000 to 25000* $cm^{-1}$.

the appendix that $\epsilon\lambda$ is proportional to the transition probability. From the microscopic point of view, which we must adopt in analyzing the spectrum, $\epsilon\lambda$ is more physically meaningful than the extinction coefficient itself. The absorption peaks at 6752 and 8168 $cm^{-1}$ were not known to exist prior to Waggener's and Hindman's work. The locations of these two peaks are the only new physical data on the neptunyl ion that have been published in the last ten years. The peaks at 18100 and 21100 $cm^{-1}$ were known previously but have now been more precisely located.

We shall follow the conventions of papers I and II concerning the descriptions and labeling of the states. The zero order wave functions are taken to be the spherical harmonics $Y_3^m(\theta, \varphi)$ multiplied by appropriate spin functions, which we designate by + and −. When the spin-orbit interaction, the ligand field and the crystalline fields of three-fold and six-fold symmetry are taken into account one obtains the following matrix elements between the various states:

| | $\lvert 3+\rangle$ | $\lvert -3+\rangle$ | $\lvert -2-\rangle$ | $\lvert 1-\rangle$ | $\lvert 0+\rangle$ |
|---|---|---|---|---|---|
| $\langle 3+\rvert$ | $\frac{3}{2}\zeta$ | $+V_6^*$ | 0 | 0 | $+\frac{1}{3}\sqrt{2}V_3'^*$ |
| $\langle -3+\rvert$ | $+V_6$ | $-\frac{3}{2}\zeta$ | $\frac{1}{2}\sqrt{6}\zeta$ | 0 | $-\frac{1}{3}\sqrt{2}V_3'$ |
| $\langle -2-\rvert$ | 0 | $\frac{1}{2}\sqrt{6}\zeta$ | $X+\zeta$ | $V_3$ | 0 |
| $\langle 1-\rvert$ | 0 | 0 | $V_3^*$ | $Y-\frac{1}{2}\zeta''$ | $\sqrt{3}\zeta'''$ |
| $\langle 0+\rvert$ | $\frac{1}{3}\sqrt{2}V_3'$ | $-\frac{1}{3}\sqrt{2}V_3'^*$ | 0 | $\sqrt{3}\zeta'''$ | $Z$ |

| | $\lvert 2-\rangle$ | $\lvert 1+\rangle$ | $\lvert -2+\rangle$ | $\lvert -1-\rangle$ |
|---|---|---|---|---|
| $\langle 2-\rvert$ | $X-\zeta$ | $\frac{1}{2}\sqrt{10}\zeta'$ | 0 | $-V_3^*$ |
| $\langle 1+\rvert$ | $\frac{1}{2}\sqrt{10}\zeta'$ | $Y+\frac{1}{2}\zeta''$ | $V_3^*$ | 0 |
| $\langle -2+\rvert$ | 0 | $V_3$ | $X-\zeta$ | $\frac{1}{2}\sqrt{10}\zeta'$ |
| $\langle -1-\rvert$ | $-V_3$ | 0 | $\frac{1}{2}\sqrt{10}\zeta'$ | $Y+\frac{1}{2}\zeta''$ |

There is a matrix similar to the first one for the states $\lvert -3-\rangle$, $\lvert 3-\rangle$, $\lvert 2+\rangle$. $\lvert -1+\rangle$ and $\lvert 0-\rangle$. It can be derived from the first one by observing that the crystalline potential is spin-independent; that $\langle 2\rvert V\rvert -1\rangle = -\langle 1\rvert V\rvert -2\rangle$; and that the matrix elements of spin-orbit interaction are identical.

$X$, $Y$, and $Z$ are the amounts the states with $m_l = \pm 2, \pm 1$ and 0, respectively, are raised above the states with $m_l = \pm 3$ by the ligand field (including the axially symmetric parts of the crystalline field). $V_3$ is the indicated matrix element of the part of the crystalline field which has three-fold symmetry about the O—U—O axis and $V_6$ is the matrix element of the part of the crystalline field which has six-fold symmetry. $\zeta$ is the spin-orbit coupling constant for a $5f$ electron in the field of the $Np^{7+}$ core.

The $5f_\sigma$ (or $m_l = 0$) orbitals are certainly used for bonding and there may also be some $\pi$-bonding which involves use of the $5f_\pi$ (or $m_l = \pm 1$) orbitals. Consequently it is the antibonding orbitals containing the $5f_\sigma$ and $5f_\pi$ functions which are indicated schematically by $\lvert 1+\rangle$, $\lvert 0+\rangle$, etc., in the matrices above. Since electrons in antibonding orbitals have a nonzero probability of being found on the oxygens, matrix elements of the spin-orbit interaction and the crystalline field must be appropriately reduced when these interactions connect an antibonding state with a nonbonding or antibonding state. It is for this reason that $\zeta'$, $\zeta''$, and $\zeta'''$ appear instead of $\zeta$ in various places in the above matrices. $\zeta'$, $\zeta''$, and $\zeta'''$ are reduced values of the spin-orbit coupling constant. For similar reasons the matrix element $\langle 3\rvert V_3\rvert 0\rangle$ should have a smaller value than one calculates when one assumes that the $5f\,\lvert 0\rangle$ orbital is localized on the $Np^{7+}$ core.

As we shall see later, it is probable that the $m_l = \pm 3$ and $m_l = \pm 2$ orbitals are also contaminated by non-5*f* wave functions. Therefore the spin-orbit coupling constant $\zeta$ which appears in the preceding matrix elements may not have the value appropriate to an isolated neptunyl ion. Moreover, $\zeta$ need not have the same value for the states $|3>$ and $|2>$ but for simplicity we assume that it does. Evidently if $\zeta' = \epsilon\zeta$ one should have $\zeta'' = \epsilon^2\zeta$. In view of the probable contamination of the $m_l = \pm 3$ and $m_l = \pm 2$ orbitals it is possible that $\epsilon > 1$. $\zeta'''$ should be appreciably smaller than the other values of $\zeta$ and not related to them in any simple way.

In I we assumed that the $5f_\sigma$ state was so high that it had no important perturbing effect on the $m_l = \pm 3$ states through the $V_3$ interaction or on the $m_l = \pm 1$ states through the spin-orbit interaction. This assumption can no longer be justified, so the $|0>$ states are retained in the present discussion.

In the absence of a magnetic field each state has two-fold (Kramers) degeneracy.

At the time we wrote our first paper we believed that the charge cloud due to the bonding electrons was the dominant factor in determining the sequence of energy levels. Since this charge cloud repels the odd electron from the ionic axis we expected the lowest doublet to be $|\pm 3\mp>$. Measurement of the *g*-values has confirmed that this doublet is indeed the ground state. We expected the states with $m_l = \pm 2$ to lie higher and to be followed by the states with $m_l = \pm 1$. We expected the antibonding $m_l = 0$ states to lie highest of all.

In 1955, the spectrum below 10000 $cm^{-1}$ was still unexplored. Our original interpretation was based on the assumption that below the two levels corresponding to the observed peaks at 18100 and 21000 $cm^{-1}$ there were only two others, namely those corresponding to the ground state $|\pm 3\mp>$ and the other $\varphi$-state $|\pm 3\pm>$. We therefore assigned the observed peaks to the states $|\pm 2\mp>$ and $|\pm 2\pm>$. The discovery of the two peaks at 6752 and 8168 $cm^{-1}$ shows that the upper peaks must actually correspond to the states $|\pm 1\mp>$ and $|\pm 1\pm>$.

It follows from what has been said about the expected sequence of the levels that the prominent absorption peak at 8168 $cm^{-1}$ must correspond to a transition from the ground state to one of the states $|3+>, |2->$ or $|2+>$. (We omit the Kramers conjugate states for clarity.) The possibility that the $|2->$ level occurs at 8168 $cm^{-1}$ can be ruled out at once for, if true, the $|2+>$ level would occur roughly $2\zeta$ higher. However, there is no trace of an absorption peak between 8168 and 15600 $cm^1$, and $\zeta$ can hardly be as large as 3700 $cm^{-1}$.

On the other hand, the assignment of the 8168 $cm^{-1}$ level to $|2+>$ can be made with reasonable values of the parameters. If we ignore such refinements as $V_3$, $V_3'$, $V_6$ and the distinction between $\zeta$, $\zeta'$, etc., we have four parameters at our disposal ($X$, $Y$, $Z$, and $\zeta$), and four observations to fit (the levels at 6752, 8168, 18100, and 21100 $cm^{-1}$). Therefore we can probably find values of the parameters such that the calculated energy levels agree with the data. In fact, if we set $X = 1608$ $cm^{-1}$, $Y = 15776$ $cm^{-1}$, $Z = 39995$ $cm^{-1}$, $\zeta = \zeta' = \zeta'' = \zeta''' = 1984$ $cm^{-1}$, $V_3 = V_3' = V_6 = 0$ we find the following energy level positions:

| | $cm^{-1}$ |
|---|---|
| $E(3-)$ | 0 |
| $E(2-)$ | 2846 |
| $E(3+)$ | 6752 |
| $E(2+)$ | 8168 |
| $E(1-)$ | 18100 |
| $E(1+)$ | 21100 |
| $E(0+)$ | 40455 |

These calculated levels are in exact agreement with the experimental absorption spectrum. Of course, no critical confirmation of the theory is achieved since there are enough adjustable parameters to make this agreement possible. However one also finds that the calculated *g*-values agree with the measured values [5] on rubidium neptunyl nitrate and the calculated temperature-independent susceptibility agrees with the value measured [6] for sodium neptunyl acetate, if suitable assumptions concerning $V_6$ and $V_3$ are made.

Despite this perfect accord between theory and experiment, and despite some uncertainties (to be discussed below) connected with the remaining alternative possibility, we prefer to associate the $|3+>$ state with the level at 8168 $cm^{-1}$.

The arguments which have led us to adopt this view come mainly from our analysis of the plutonyl spectrum, and will be reviewed more critically in a subsequent paper which will be devoted to $PuO_2^{++}$ and $NpO_2^{+}$. Here it will suffice to outline their nature.

The spectrum of $PuO_2^{++}$ is remarkable for the presence of a very strong, very narrow absorption band at 12050 $cm^{-1}$. Its extreme sharpness suggests most strongly that the electronic charge distribution in the upper state is almost identical with that in the ground state, so that fluctuating electric fields have negligible effect on the energy separation of the two levels. To a first approximation the ground state of $PuO_2^{++}$ (with two 5*f*-electrons) is the degenerate doublet $|3-, 2->$ and $|-3+, -2+>$. We are convinced that the upper level at 12050 $cm^{-1}$ is the doublet approximating to $|-3-, 2->$ and $|3+, -2+>$. The electronic transition corresponds to a change in the orbital quantum number $m_l$ of one of the electrons from $-3$ to 3, or conversely – without change of spin. The charge distribution is not changed by this transition, and the absorption peak is therefore narrow. A further step in the argument concerns the strength of the absorption. If one knew the matrix elements which determine the absorption of light by the one-electron system $NpO_2^{++}$, and the compositions of the states of the two-electron system $PuO_2^{++}$ (or $NpO_2^{+}$), and if one assumed the inner fields and environment to be the same for the two ions, one could estimate the strengths of the absorption bands of $PuO_2^{++}$ (or $NpO_2^{+}$). Now, it is remarkable that the strength of the dominant line in the plutonyl spectrum agrees very closely with that of the dominant line at 8168 $cm^{-1}$ in the neptunyl spectrum. We are therefore led to conclude that the transition involved is the same in the two cases, i.e., from $|\pm 3\mp>$ to $|\mp 3\mp>$. It is on this basis that we have assigned the 8168 $cm^{-1}$ level to $|\pm 3\pm>$.

If we set $X=-1716$ $cm^{-1}$, $Y=14558$ $cm^{-1}$, $Z=131102$ $cm^{-1}$, $\zeta=\zeta'=\zeta''=\zeta'''=2248$ $cm^{-1}$, and $V_3=V_3'=V_6=0$ we obtain the following energy levels:

| | $cm^{-1}$ |
|---|---|
| $E(3-)$ | 0 |
| $E(2-)$ | 208 |
| $E(2+)$ | 6750 |
| $E(3+)$ | 8167 |
| $E(1-)$ | 18100 |
| $E(1+)$ | 21100 |
| $E(0+)$ | 136026 |

Again there is precise agreement with experiment.

Two objections to our proposed assignments follow from the figures just quoted. In the first place, $X$ is negative; that is, the $m_l=\pm 2$ orbitals are below the $m_l=\pm 3$ orbitals whereas we had expected the reverse to be the case. To account for this negative value of $X$ we must assume that the surrounding ions or molecules give rise to a field with axial symmetry which repels the odd electron from the equatorial plane. The existence of such a field follows from our model of the solvation sphere, with six water molecules in a puckered ring.

The second objection is to the low position (200 $cm^{-1}$) of the $|2->$ state. If it were really as low as this, it would be appreciably populated at room temperature, and would give rise to satellite absorption peaks 200 $cm^{-1}$ to the red of the main peaks. Although such peaks would not be resolved, their presence would be detectable, but the spectrum shows no sign of them. In addition, if the $|2->$ state were as low as 200 $cm^{-1}$ the calculated temperature-independent susceptibility would be much larger than the measured value. However, when such refinements as $V_6$, $\zeta'$, etc., are considered, the calculated position of the $|2->$ level relative to $|3->$ is raised to 500–1000 $cm^{-1}$. Therefore the difficulties associated with the position of the $|2->$ level may be phantasmal.

Possibly the ligand and crystalline fields are not the same in a solution as they are in a crystalline solid. However, such an *ad hoc* hypothesis to account for the depression of the $m_l = \pm 2$ states relative to the $m_l = \pm 3$ states in solution does not appear very satisfactory. It is also possible that the very difficult susceptibility measurements are in error. It would be interesting to have these measurements extended to a range of neptunyl compounds. Better still, it would be valuable to study the optical absorption, magnetic resonance and susceptibility of the same compound.

The two hypotheses described above, both of which are adequate for interpreting the positions of the energy levels, differ in the value of the spin-orbit coupling constant required. One might think that it would be possible to decide between the two hypotheses if the value of $\zeta$ for some other hexavalent neptunium compound were known. Recently magnetic and spectroscopic data on $NpF_6$ have become available. Unfortunately, the unambiguous determination of the value of $\zeta$ from these data has proved difficult.

Our analysis [7] of the data on $NpF_6$ led to two possible interpretations, neither of which was wholly satisfactory. One, which accounted for the magnetic resonance and susceptibility data, and gave energy levels at the positions of the two known absorption bands in the near infrared, required $\zeta = 1941$ cm$^{-1}$. Its defects were that the ratios of the ligand field parameters which entered into the theory were not very plausible on the basis of our model of the molecular structure; and that it predicted an infrared absorption band around 3000 cm$^{-1}$, which has not been found experimentally. The other, requiring $\zeta = 2405$ cm$^{-1}$, accounted satisfactorily for the positions of all the absorption bands, including some in the ultraviolet whose ascription to $5f$–$5f$ transitions is by no means certain, but it led to a value for the temperature-independent part of the susceptibility which is much lower than is observed.

It is tempting to think that the agreement between the numbers 1941 cm$^{-1}$ for $NpF_6$ and 1985 cm$^{-1}$ for $NpO_2^{++}$ indicates that the "correct" value for the spin-orbit coupling constant is close to these figures. Other arguments for accepting the value 1985 cm$^{-1}$ are given above. Nevertheless, we think that the spin-orbit coupling constant for the neptunyl ion probably has a value near 2200 cm$^{-1}$, and the higher value of $\zeta$ for $NpF_6$ is also probably the correct one.

## 3. General Considerations Concerning the Interpretation of the Spectrum

The principal features of the absorption spectrum are apparent on casual inspection of figures 1 and 2. There are four peaks below 22000 cm$^{-1}$ which we ascribe to electronic transitions within the $5f$ shell. The steep rise of the absorption curve above 23000 cm$^{-1}$ is probably due to an allowed $5f$ to $6d$ transition. The four subsidiary peaks are probably part of the vibrational fine structure.

As we have already indicated, the interpretation of the spectrum is not free from ambiguity. In addition to the difficulty connected with assigning peaks to particular electronic levels there is uncertainty in the interpretation because of the widths of the peaks and (in some cases) their vibrational fine structures.

We must remember that we are not dealing with an ion in a fixed environment, but with an ion whose environment adapts itself to the ion. Energies are therefore not those of an isolated ion, but those of the whole system. It would be too ambitious to try to deal with this system in its full generality; it seems wiser to ask ourselves what would be the energy levels of the ion in the environment which it has in its ground state. Even this question is imprecise, for that environment is not a fixed one. We can restore precision to the question we wish to answer by postulating some static mean environment. When we are calculating magnetic properties in the ground state, the energies in the mean environment are the ones which are relevant.

There is a distinction between the energies so defined and the energies actually observed (as frequencies) in an absorption spectrum, for the equilibrium configuration of the environment will be altered for the excited electronic states of the ion. The ionic energy as we propose to study it is higher than the energy of the system with the ion in its excited electronic state and the environ-

ment in equilibrium with that state. The result is that the electronic transition is accompanied by the excitation of vibrational motion in the environment, and the transition is not sharp. This excitation is responsible, in part, for the line width.

Furthermore we are dealing with a complex ion which is itself capable of internal vibration. In excited states the equilibrium Np–O bond distance is not the same as in the ground state, and vibrations, notably of the symmetrical stretching mode, can be excited in an electronic transition. Therefore vibrational fine structure is observed in the absorption spectrum.

It is also important to remember that we are dealing with optical transitions between levels of the same electronic parity ($5f_u \rightarrow 5f_u$). The transitions are therefore forbidden. Quantitative analysis of their intensity shows that the two dominant mechanisms available to parity-forbidden transitions in atomic spectroscopy, namely magnetic dipole and electric quadrupole couplings to the electromagnetic field, are much too weak to account for the observed absorption bands. The only mechanism capable of giving the observed absorption is electric dipole coupling induced by the fluctuating field of the environment. This coupling causes departures from the perfect odd parity of the electronic states, and thereby allows nonvanishing matrix elements of electric dipole moment.

In the fluctuating fields arising from distortions and motions of the solvation sphere and from vibrations of the ion, nearly all the selection rules of atomic and molecular spectroscopy break down. One, however, remains in modified form, namely the rule that in an optical transition there is no change of spin quantum number. Since the "crystalline" fields and the electric dipole moment are spin-independent, no perturbation by these fields can give transition matrix elements between states of different spin.

It will be seen in this and subsequent papers that although changes in $m_l$ from 0 to $\pm 6$ are encountered, $\Delta m_s$ is zero in all except some very weak bands. (This statement needs qualification when $m_s$ is not a good quantum number, and we shall discuss it more precisely in a later paper.) Indeed we shall see that the strongest bands correspond to $\Delta m_l = \pm 6$.

All of the absorption peaks are rather broad and asymmetrical. Consequently it is not clear what energies should be used as the positions of the electronic levels. If we consider only first order couplings with the environment, and if an absorption peak is not too broad, then it can be shown that the centroid [3] of the peak corresponds to the sum of the ionic energy, as we have defined it, and a positive correction which is connected with the transfer of energy to the vibrations of odd parity which induce the electric moment in these otherwise parity–forbidden transitions. When the fluctuations which give rise to the dipole moment are slow, as we believe to be the case here, this correction is negligible. In any case, the first order perturbations will not lead to any asymmetry of the absorption peaks.

If the width and asymmetry of a peak are due to random depression of the ground state by second order coupling with the nearby $|2->$ state then the energy shift is given by $(V^2+W^2)/\Delta E$, where $V$ and $W$ are the real and imaginary parts of the appropriate matrix element, and $\Delta E$ is the energy gap between the two states. It is reasonable to assume that $V$ and $W$ can be represented by Gaussian distributions with equal amplitudes and widths. The line shape corresponding to these assumptions can easily be calculated. The absorption jumps from zero to a finite value at the threshold and falls off exponentially thereafter. In order to account for the observed line shapes it is necessary to make additional assumptions; for example, that second order perturbations also move the upper levels about. We will not push this possible interpretation any further.

An alternative and more probable explanation of the marked asymmetry of the absorption peaks is that it is due to unresolved vibrational fine structure. We can get a rough idea of the positions, amplitudes and widths of the peaks by fitting a sum of Gaussian functions to the observed absorption curve. This fitting lacks any theoretical justification so it should not be taken too seriously. In the following discussion the amplitudes are expressed in units of $6900\ \epsilon\lambda$ where $\epsilon$ is the molar extinction coefficient and $\lambda$ is the wavelength in cm.

[3] More precisely, the centroid of the $\epsilon/\nu$ versus $\nu$ curve.

After making an allowance of 0.39 units for the background one finds that the peak whose maximum is at 6752 $cm^{-1}$ can be fitted by a Gaussian function whose amplitude is 4.70 and whose full width at half maximum is 292 $cm^{-1}$. A small peak is left over, centered at about 7039 $cm^{-1}$, with an amplitude of 0.90 and width 210 $cm^{-1}$. These two peaks together fit 42 points read off Waggener's curve with a maximum deviation of 0.10 and a root mean square deviation of 0.047.

The large absorption peak at 8168 $cm^{-1}$ may have as many as four subsidiary peaks on the high frequency side and two on the low frequency side.

According to our analysis (which, it must be admitted, is not unique) the separation of the unresolved peaks is about 200 $cm^{-1}$. The bending frequency in the ground state of the uranyl ion is known to be about 215 $cm^{-1}$. Therefore it is possible to assign all the subsidiary peaks below 10000 $cm^{-1}$ to vibrational fine structure. The peaks on the high frequency side of the main peaks may be due to the electronic transitions accompanied by excitation of the bending mode. It seems reasonable that the bending vibrations rather than the stretching vibrations should be involved here since, in both ground and excited electronic states, the charge distribution is near the equatorial plane.

One puzzling feature is that the 8168 $cm^{-1}$ peak is almost as wide (233 $cm^{-1}$) as the 6752 $cm^{-1}$ peak. In first approximation it corresponds to a transition from $m_l = \pm 3$ to $m_l = \mp 3$, involving no change of charge distribution, and therefore should be very narrow. Even when allowance is made for the contamination of the ground state by $|2+>$, the change in charge distribution is still considerably less (by a factor of at least 2) than for the 6752 $cm^{-1}$ line. It may be that the nearby $|2->$ state perturbs the ground state. Fluctuating fields which couple the two states might cause them to spread in energy over a range sufficient to account for the 233 $cm^{-1}$ width. In plutonyl, where the lowest excited level is at 2500 $cm^{-1}$, the width of the 12050 $cm^{-1}$ peak, which should be closely comparable with the 8168 $cm^{-1}$ peak in neptunyl, is less than 50 $cm^{-1}$. The fact that the 6752 $cm^{-1}$ peak is (slightly) wider than the 8168 $cm^{-1}$ peak is a point in favor of the assignment of the upper levels to $|2+>$ and $|3+>$ respectively.

It is more difficult to analyze the complex structure of the absorption spectrum above 15000 $cm^{-1}$. However, the set of Gaussian curves whose descriptions follow yields a representation of the absorption curve which accords very closely with the data.

| Center | Amplitude | Width at half maximum | Strength |
|---|---|---|---|
| $cm^{-1}$ | | $cm^{-1}$ | |
| 15670 | 0.300 | 588 | 0.97 |
| 16245 | .690 | 588 | 2.23 |
| 16850 | .620 | 588 | 2.00 |
| 18100 | 2.180 | 1540 | 18.44 |
| 18590 | 0.077 | 588 | 0.25 |
| 19150 | .410 | 588 | 1.32 |
| 19760 | .550 | 588 | 1.78 |
| 21100 | 2.000 | 1660 | 18.24 |
| 22330 | 0.352 | 588 | 1.14 |
| 25210 | 4.933 | 3241 | ..... |

The sum of these curves has a maximum deviation of 0.07 from 75 points read off Waggener's curve between 15000 and 24400 $cm^{-1}$. The root mean square deviation is 0.024. It is rather tedious to fit Gaussian curves to the experimental spectrum so no serious effort was made to find the set which minimizes the root mean square deviation. Such an effort is likely to be unrewarding in view of the unavoidable errors in plotting the experimental curve, and in reading points off it.

Although one can argue about the details, the following general points seem to be well established. (1) The two principal absorption peaks at 18100 and 21100 $cm^{-1}$ have nearly the same widths (1600 $cm^{-1}$) and strengths (18.3). (2) There are three subsidiary peaks at 15670, 16245,

and 16850 $cm^{-1}$. (3) There are two subsidiary peaks at 19150 and 19760 $cm^{-1}$ and possibly a third at 18590 $cm^{-1}$. (4) There is a subsidiary peak at 22330 $cm^{-1}$. (5) All the subsidiary peaks have nearly the same width of 590 $cm^{-1}$. They are very much narrower than the principal peaks.

The similarity of the two principal peaks is strong evidence in favor of our hypothesis that they are both due to transitions to an orbital state with $|m_l| = 1$. The width of these peaks is possibly associated with nonequilibrium configurations of the ion and its environment.

The subsidiary peaks listed under (2) and (3) above are quite possibly not associated with the principal peaks. In the first place, they are definitely narrower than the latter. Secondly, they seem to form two similar groups; one group occurs on the low frequency side of each principal peak. Consequently they probably cannot be ascribed to transitions in which vibrational modes are excited. The strengths of the subsidiary peaks are too great for the peaks to be ascribed to transitions from the vibrationally excited ground electronic state.

We are inclined to attribute the subsidiary peaks below 20000 $cm^{-1}$ to transitions in which, in the final electronic state, the environment has accommodated itself to the altered charge distribution of the ion. That is, the energies 15670 $cm^{-1}$, 16245 $cm^{-1}$, etc. correspond to states in which the environment is distorted away from its ground state configuration toward that appropriate to the $|1->$ and $|1+>$ electronic states.

The energy differences of the successive peaks listed under (2) and (3) are all approximately 600 $cm^{-1}$. This difference possibly represents the energy of the symmetric stretching vibration in the excited state. That the stretching vibrations of the neptunyl ion should be strongly excited is plausible, for the electron in the $m_l = \pm 1$ upper state is much closer to the bonding electrons than when in the ground state, so that the equilibrium bond distance must be considerably changed. On the other hand, 600 $cm^{-1}$ is a rather low energy for the stretching vibration. It is a moot question whether the energy of this vibration can change from about 860 $cm^{-1}$ in the ground state to 600 $cm^{-1}$ in an excited state.

The small peak at 22330 $cm^{-1}$ is probably part of the vibrational fine structure of the principal peak at 21100 $cm^{-1}$. If so, its position ($21100 + 2 \times 615$) indicates that the energy of the stretching vibration really is about 600 $cm^{-1}$. Because of the strongly rising absorption above 22600 $cm^{-1}$ it is impossible accurately to determine the width of the 22330 $cm^{-1}$ peak. It may very well be greater than the 588 $cm^{-1}$ quoted above.

## 4. Values for the Empirical Parameters of the Theory

In comparing the theoretical and experimental values of the coefficients in the spin Hamiltonian, and for the purpose of extending the theory to other uranyl-type ions, it is important to know the extent to which the observed neptunyl absorption peaks fix the values of the parameters. We have already introduced ten of these parameters: $X$, $Y$, $Z$, $\zeta$, $\zeta'$, $\zeta''$, $\zeta'''$, $V_3$, $V_3'$, and $V_6$. The locations of the four absorption peaks provide only four relations among them. Roughly speaking they determine $X$, $Y$, and $\zeta$ fairly closely, and $Z$ to within 50 percent. Varying the remaining parameters ($\zeta$, $\zeta'$, $\zeta''$, $\zeta'''$ remaining roughly equal) causes only slight changes in $X$, $Y$, and $\zeta$. $V_6$ has a strong effect on $g_\perp$, and can be estimated from that. $g_{||}$ is sensitive to $V_6$ and $V_3'$, and is also very sensitive to "$l$-reduction," i.e., a loss of 5$f$-character in the $|3->$ wave function due to partial overlap with the orbitals on the six equatorial oxygen atoms. This $l$-reduction is very similar to the mechanism which reduces $\zeta$ to $\zeta'$ etc., but applies to the $|\pm 3>$ states. The susceptibility is extremely sensitive to the position of the $|2->$ level.

Clearly we cannot determine all the parameters of the theory from the experimental data. Rather, we must attempt to show that reasonable values for the parameters, suggested by the nature of the model, are capable of explaining the salient features of the observations. Our procedure will be to assign values to the crystal field matrix elements, and then show how the remaining parameters are related.

The simplest case to treat is that for which $V_3 = V_3' = V_6 = 0$. In this case the secular equations can be factored so that the most complicated equation one has to solve is quadratic in the energy. The experimental positions of the $|2+>$ and $|3+>$ levels determine $\zeta$ and $X$ uniquely. One finds $\zeta = 2248\ \text{cm}^{-1}$ and $X = -1716\ \text{cm}^{-1}$.

Next, using the information that $|1+>$ is at $21100\ \text{cm}^{-1}$, we can determine $Y$. It will be seen that the relevant energy matrix contains $\zeta'$ and $\zeta''$ as well as $\zeta$. We assume that $\zeta' = \epsilon\zeta$ and $\zeta'' = \epsilon^2\zeta$ where $\epsilon$ is a parameter probably less than but near 1. One easily finds that

$$Y = 16305 - 1747.3\ \epsilon^2.$$

The energy of the $|2->$ state is the other eigenvalue of the matrix and can be determined when $Y$ is known. One finds that $E(2-) = 831 - 623.3\ \epsilon^2$.

Having found $Y$ we can now use the position of the $|1->$ level, $18100\ \text{cm}^{-1}$, to determine $Z$. $\zeta'''$ appears in this calculation as well as $\epsilon$. The calculation also determines the energy of the $|0\pm>$ level. One finds that

$$Z = 13305 + \frac{\zeta'''^2}{1000 - 957.1\epsilon^2}$$

$$E(0\pm) = 21100 - 2871.3\epsilon^2 + \frac{\zeta'''^2}{1000 - 957.1\epsilon^2}.$$

All of these formulas are exact; that is, they do not result from perturbation calculations. Results for various values of $\epsilon^2$ are given in the following table:

| $\epsilon^2$ | $Y(\text{cm}^{-1})$ | $Z(\text{cm}^{-1})$ | $E(2-)\text{cm}^{-1}$ | $E(0\pm)\text{cm}^{-1}$ |
|---|---|---|---|---|
| 1.0 | 14558 | $13305 + \zeta'''^2/42.9$ | 208 | $18229 + \zeta'''^2/42.9$ |
| 0.9 | 14732 | $13305 + \zeta'''^2/138.6$ | 270 | $18516 + \zeta'''^2/138.6$ |
| .8 | 14907 | $13305 + \zeta'''^2/234.3$ | 332 | $18803 + \zeta'''^2/234.3$ |
| .7 | 15082 | $13305 + \zeta'''^2/330.0$ | 395 | $19090 + \zeta'''^2/330.0$ |

We obtain a very rough value for $Z$ by observing that $\zeta'''$ is less than $\zeta$ but probably more than $\frac{1}{2}\zeta$. It follows that $Z$ lies between about $131000\ \text{cm}^{-1}$ (for $\epsilon^2 = 1$, $\zeta''' = \zeta$) and $17100\ \text{cm}^{-1}$ (for $\epsilon^2 = 0.7$, $\zeta''' = \frac{1}{2}\zeta$). This determination of $Z$ is particularly sensitive to the separation between the $|1+>$ and $|1->$ levels. Since this separation cannot be accurately determined from the spectrum, not much can be deduced concerning $Z$.

On the basis of our model we expected $Z$ to be greater than $Y$ (perhaps $Z > 25000\ \text{cm}^{-1}$), and perhaps less than $50000\ \text{cm}^{-1}$. No conflict occurs.

Essentially what we learn from the preceding calculation is that our interpretation of the 18100 and $21100\ \text{cm}^{-1}$ peaks as the doublet $|1->$ and $|1+>$ is consistent with the value of $\zeta$ deduced from the infrared peaks, provided $\epsilon^2$ and $\zeta'''$ are suitably chosen. A more significant way of presenting the results of these calculations is embodied in the following equation:

$$\epsilon^2 = 1.045 - \frac{\zeta'''^2}{957(Z - 13305)} \pm 0.070,$$

The indicated uncertainty is the effect of the $\pm 200\ \text{cm}^{-1}$ possible error in the separation between the peaks at 18100 and $21100\ \text{cm}^{-1}$. Since $\epsilon^2$ is probably near 1, we see that some limitation is imposed on our assumptions concerning the values of $Z$ and $\zeta'''$, but that the uncertainties in the observational values are such that these constraints are practically ineffective.

The next simplest case to treat is that in which $V_3' = V_3 = 0$ and $V_6$ differs from zero. We shall take $V_6$ to be 1500 $cm^{-1}$, since this order of magnitude is suggested by resonance data. Again the values of $\zeta$ and $X$ are uniquely determined by the positions of the $|2+>$ and $|3+>$ levels. One finds $\zeta = 2071$ $cm^{-1}$, $X = -599$ $cm^{-1}$. With this choice of $\zeta$ and $X$, $E(2+)$ is 6752 $cm^{-1}$ and $E(3+)$ is 8168 $cm^{-1}$. One can then determine $Y$, $Z$, $E(2-)$ and $E(0\pm)$ as before. One finds the results given in the following table.

| $\epsilon^2$ | $Y(cm^{-1})$ | $Z(cm^{-1})$ | $E(2-)(cm^{-1})$ | $E(0\pm)(cm^{-1})$ |
|---|---|---|---|---|
| 1.0 | 15026 | $13617+\zeta'''^2/124.35$ | 1257 | $18473+\zeta'''^2/124.35$ |
| 0.9 | 15185 | $13617+\zeta'''^2/211.91$ | 1313 | $18736+\zeta'''^2/211.91$ |
| 0.8 | 15344 | $13617+\zeta'''^2/299.48$ | 1368 | $18998+\zeta'''^2/299.48$ |
| 0.7 | 15503 | $13617+\zeta'''^2/387.05$ | 1424 | $19261+\zeta'''^2/387.05$ |

The uncertainty concerning $Z$ can be expressed as before by an equation:

$$\epsilon^2 = 1.142 - \frac{\zeta'''^2}{8.75.65(Z-13617)} \pm 0.076.$$

Finally we shall obtain values of $\zeta$, $X$, $Y$, and $Z$ for the case $V_3' = \frac{1}{2}V_3 = 500$ $cm^{-1}$, $V_6 = 0$, $\zeta''' = \frac{1}{2}\zeta$, $\zeta' = 0.95\zeta$, $\zeta'' = 0.95\zeta'$. If we take $\zeta = 2249$ $cm^{-1}$, $X = -1620$ $cm^{-1}$, $Y = 14670$ $cm^{-1}$, $Z = 22400$ $cm^{-1}$ we find the following energy level positions:

| | $cm^{-1}$ |
|---|---|
| $E(3-)$ | 0 |
| $E(2-)$ | 306 |
| $E(2+)$ | 6754 |
| $E(3+)$ | 8162 |
| $E(1-)$ | 18108 |
| $E(1+)$ | 21091 |

The conclusion we draw from these calculations is that for moderate values of the crystalline fields and various amounts of covalence the spin-orbit coupling constant and the parameters of the ligand field are fairly well determined. $\zeta$ probably lies in the range 2070 to 2250 $cm^{-1}$, $X$ lies between $-600$ and $-1720$ $cm^{-1}$, and $Y$ lies between 14500 and 15500 $cm^{-1}$.

The effect of the nonaxial field $V_6$ is to raise the $|2->$ level relative to $|3->$. This perturbation is roughly quadratic in $V_6$. The perturbations by $V_3$ and $V_3'$ (also quadratic) can move the $|2->$ level either way relative to $|3->$. The effect of reductions in $\zeta'$ and $\zeta''$ is to raise the $|2->$ level. It is therefore likely that this level is higher than 200 $cm^{-1}$, but it is probably lower than 1400 $cm^{-1}$.

## 5. Spectroscopic Splitting Factors

In I we gave approximate formulas for the $g$-values and the susceptibility of the neptunyl ion. More complete formulas will be given here.

It follows from the interaction matrices that there are three types of states for the neptunyl ion. They are

$$|a> = |-3+><-3+|a> + |-2-><-2-|a> + |3+><3+|a>$$

$$+|1-><1-|a> + |0+><0+|a>,$$

$$|b>=|3->\langle 3-|b>+|2+>\langle 2+|b>+|-3->\langle -3-|b>$$

$$+|-1+>\langle -1+|b>+|0->\langle 0-|b>,$$

$$|c>=|2->\langle 2-|c>+|-2+>\langle -2+|c>+|1+>\langle 1+|c>$$

$$+|-1->\langle -1-|c>.$$

The ground state is a Kramers doublet of types $|a>$, $|b>$.

In I we defined our basic states $|a>$ and $|b>$ the other way round (i.e., $|3->$ and $|-3+>$ respectively in first approximation) which has the disadvantage that $g_{yy}$ is of opposite sign to $g_{xx}$, so that the axial symmetry of the magnetic properties is lost in the formulation. Our present choice of basic states is consistent with magnetic axial symmetry.

The coefficients occurring in $|b>$ are equal in magnitude to those in $|a>$. From Kramers' theorem one has

$$\langle 0-|b>=\langle 0+|a>^*$$

$$\langle 3-|b>=-\langle -3+|a>^*$$

$$\langle 2+|b>=-\langle -2-|a>^*$$

$$\langle -3-|b>=-\langle 3+|a>^*$$

$$\langle -1+|b>=\langle 1-|a>^*$$

In the double nitrates isomorphous with $Rb(UO_2)(NO_3)_3$ the symmetry of the crystalline field is such that if the $c$-axis is chosen as $z$-axis, and an axis joining the center of a nitrate group to the neptunium atom is chosen as $y$-axis, all matrix elements $V_6$, $V_3$, $V_3'$ are real, and the coefficients above are all real.

In calculating the matrix elements of the magnetic moment operator it is necessary to allow for possible $l$-reduction [8, 9]. The $m_l=\pm 1$ orbitals may be partially used in $\pi$-bonding as already described. We shall denote the appropriately reduced value of $L$ by $k_1L$. Similarly, the $m_l=\pm 2$, $\pm 3$ orbitals may overlap the oxygen atoms which form the equatorial ring. We shall denote the reduced $L$'s by $k_2L$ and $k_3L$, respectively. (We shall assume that matrix elements of $\mathbf{L}$ between the states with $m_l=\pm 2$ and $\pm 3$ are reduced by $\sqrt{k_2k_3}$, etc.). One then finds the following matrix elements of the magnetic moment operator:

$$\langle a'|\mathbf{L}+2\mathbf{S}|a>=\{(1-3k_3)\langle a'|-3+>\langle -3+|a>-(2k_2+1)\langle a'|-2->\langle -2-|a>$$

$$+(3k_3+1)\langle a'|3+>\langle 3+|a>+(k_1-1)\langle a'|1->\langle 1-|a>+\langle a'|0+>\langle 0+|a>\}\mathbf{k}$$

$$\langle b|\mathbf{L}+2\mathbf{S}|a>=\{\tfrac{1}{2}\sqrt{6k_3k_2}\,[\langle b|2+>\langle 3+|a>+\langle b|-3->\langle -2-|a>]$$

$$+\langle b|3->\langle 3+|a>+\langle b|-3->\langle -3+|a>$$

$$+\sqrt{3k_1k_0}\,[\langle b|0->\langle 1-|a>+\langle b|-1+>\langle 0+|a>]$$

$$+\langle b|0->\langle 0+|a>\}(\mathbf{i}+i\mathbf{j})$$

$$< c \mid \mathbf{L}+2\mathbf{S} \mid a >= \{ < c \mid -2+ >< -2- \mid a > + < c \mid 1+ >< 1- \mid a >$$

$$+\tfrac{1}{2}\sqrt{6k_3k_2} < c \mid -2+ >< -3+ \mid a >$$

$$+\tfrac{1}{2}\sqrt{10k_2k_1}\,[ < c \mid 2- >< 1- \mid a > + < c \mid -1- >< -2- \mid a > ]$$

$$+\sqrt{3k_1k_0} < c \mid 1+ >< 0+ \mid a > \}(\mathbf{i}-i\mathbf{j})$$

It follows that

$$g_{\|} = 2\{(1-3k_3) \mid < -3+ \mid a > \mid^2 - (2k_2+1) \mid < -2- \mid a > \mid^2 + (3k_3+1) \mid < 3+ \mid a > \mid^2$$

$$+(k_1-1) \mid < 1- \mid a > \mid^2 + \mid < 0+ \mid a > \mid^2\}$$

$$g_{\perp} = 2\{-\sqrt{6k_3k_2} < 3+ \mid a >< -2- \mid a > -2 < 3+ \mid a >< -3+ \mid a >$$

$$+2\sqrt{3k_1k_0} < 0+ \mid a >< 1- \mid a > + < 0+ \mid a >^2\}.$$

If we neglect nonaxial fields, $|a>$ contains only $|-3+>$ and $|-2->$, and $|b>$ only $|3->$ and $|2+>$, from which it is easily seen that $g_{\perp}$ is zero. In fact if we take the parameters $\zeta = 2248$ cm$^{-1}$, $X = -1716$ cm$^{-1}$, $V_3 = V_3' = V_6 = 0$ we find

$$|a> = 0.8883\,|-3+> - 0.4593\,|-2->$$

$$|b> = -0.8883\,|3-> + 0.4593\,|2+>$$

and

$$g_{\|} = -\{0.7891\,(6k_3-2) + 0.2109\,(4k_2+2)\}$$

$$g_{\perp} = 0.$$

With $k_3 = k_2 = 1$, one obtains $g_{\|} = -4.4218$. With $k_3 = k_2 = 0.9$, $g_{\|} = -3.8640$.

The experimental values for rubidium neptunyl nitrate [5, 10] are $|g_{\|}| = 3.405 \pm 0.008$ and $|g_{\perp}| = 0.205 \pm 0.006$. They differ from the above values in that, first $g_{\perp} \neq 0$, and secondly $|g_{\|}|$ is lower. As was discussed in I, the effect of $V_6$ is to give rise to a nonzero $g_{\perp}$ and to some reduction in $|g_{\|}|$. Orbital reduction will further reduce $|g_{\|}|$.

$V_3$ and $V_3'$ will also modify the $g$-values slightly, but their contributions are secondary so that if we wish to determine the parameters of the theory approximately we can concentrate on $V_6$, $k_3$, and $k_2$. We shall assume that $k_3 = k_2$ for simplicity. If we set

$$\zeta = 2175 \text{ cm}^{-1},\ X = -1220 \text{ cm}^{-1},\ V_6 = 1000 \text{ cm}^{-1},\ V_3 = V_3' = 0,$$

which parameters give energy levels in the correct places, we have

$$|a> = 0.8975\,|-3+> - 0.4262\,|-2-> - 0.1134\,|3+>$$

$$|b> = -0.8975\,|3-> + 0.4262\,|2+> + 0.1134\,|-3->.$$

For $k_3 = k_2 = 1$, one has $g_{\|} = -4.2084$, $g_{\perp} = 0.1706$. With $k_3 = k_2 = 0.9$, this becomes modified to $g_{\|} = -3.6602$, $g_{\perp} = 0.1942$. With $k_3 = k_2 = 0.85$ the values are $g_{\|} = -3.3861$ and $g_{\perp} = 0.2060$.

These results indicate that $V_6$ around 1000 $cm^{-1}$, and orbital reduction to about 85 percent are adequate hypotheses to account for the resonance results. Such a large amount of orbital reduction implies considerable overlap of the $5f$ wave functions on the oxygen atoms of the nitrate groups. Such partial covalency in the formation of a hexanitrato-uranyl ion has already been considered on chemical grounds by Coulson and Lester [11]. If this deduction is correct, the parameter $\zeta$ which enters into our calculations does not have the value of the spin-orbit coupling constant in the free neptunyl ion, but a value reduced by about 0.85. It follows that in the free ion $\zeta = 2178/0.85 = 2560$ $cm^{-1}$. Too much should not be made of this estimate, however, since we are combining optical data from aqueous solution with magnetic data from $Rb(NpO_2)(NO_3)_3$, and the "crystalline" fields may be quite different in the two systems. However, such a line of thought suggests that the apparent discrepancy between the values of $\zeta$ derived from the $NpO_2^{++}$ solution absorption spectrum and from the $NpF_6$ spectrum (about 2400 $cm^{-1}$) is capable of resolution.

In future work on neptunyl compounds it would be worthwhile to study the Zeeman effect in the spectra of crystals, since the Zeeman splittings furnish a valuable test of the identification of the lines. One expects large Zeeman splittings for several of the levels when the magnetic field is parallel to the ionic axis.

We therefore give, as a guide, the approximate values of the spectroscopic splitting factors deduced from simple calculations (which neglect orbital reduction).

| State | Energy | $\lvert g_{\parallel}\rvert$ (uncorrected for orbital reduction) |
|---|---|---|
| | $cm^{-1}$ | |
| $\lvert -3+>$ | 0 | 4.2 |
| $\lvert \ 2->$ | 664 | 2.1 |
| $\lvert \ 2+>$ | 6752 | 4.3 |
| $\lvert \ 3+>$ | 8168 | 5.6 |
| $\lvert \ 1->$ | 18100 | 0.0 |
| $\lvert \ 1+>$ | 21100 | 3.9 |

The absorption spectrum of crystals of $Rb(NpO_2)(NO_3)_3$ (or mixed crystals with the isomorphous uranyl salt) will probably give sharp enough lines at low temperatures to permit the Zeeman structure to be resolved. Each line will be split into four components, two of which will be strong and two weak, because of the operation of the selection rule $\Delta m_s = 0$. The approximate splittings to be expected for the vibrationless (0–0) electronic transitions are as follows:

| Transition | Expected Zeeman splitting/"Normal" Zeeman splitting | |
|---|---|---|
| | Strong components | Weak components |
| $\lvert -3+> \rightarrow \lvert -2+>$ | 2.1 | 6.3 |
| $\lvert -3+> \rightarrow \lvert \ 2+>$ | 8.5 | 0.1 |
| $\lvert -3+> \rightarrow \lvert \ 3+>$ | 9.8 | 1.4 |
| $\lvert -3+> \rightarrow \lvert -1+>$ | 4.2 | 4.2 |
| $\lvert -3+> \rightarrow \lvert \ 1+>$ | 8.1 | 0.3 |

These are large Zeeman separations, and should not be difficult to detect provided the absorption lines in the crystalline state are sharp. In view of the sharpness of the lines in the absorption spectrum of $RbUO_2(NO_3)_3$, where a considerably smaller Zeeman effect was detected [12], there is reason to believe that this condition will be satisfied.

## 6. Nuclear Hyperfine Structure

The nuclear hyperfine structure is described by the term

$$AS'_z I_z + B(S'_x I_x + S'_y I_y) + PI_z^2$$

in the spin Hamiltonian, where $S'$ is the fictitious spin. The derivation of the hyperfine structure parameters $A$, $B$, and $P$ from the characteristics of the states $|a>$ and $|b>$ was described in I, and can be deduced from equations (2.3), (2.8), and (2.9) of Abragam and Pryce [13]. We here wish to add two points to the previous discussion.

First, consequent on the interchange of the basic states $|a>$ and $|b>$ as compared with I, the sign of $A$ (like that of $g_{||}$) must be reversed. This reversal is not trivial, for the resonance data, while not determining the sign of $A$, do determine the relative signs of $A$ and $P$. Theoretical prediction of the sign of $A$ therefore implies theoretical prediction of the sign of the quadrupole moment of the nucleus, and our previous deduction was wrong. The present interpretation of the data of Bleaney et al. [5] and Llewellyn (quoted by Bowers and Owen [10]) for $Np^{237}$ in $Rb(NpO_2)(NO_3)_3$ is

$$\begin{aligned} A &= -0.16547 \pm 0.00008 \text{ cm}^{-1} \\ |B| &= \ \ 0.01782 \pm 0.00003 \text{ cm}^{-1} \\ P &= +0.03017 \pm 0.00007 \text{ cm}^{-1}. \end{aligned}$$

The sign of $A$ is based on the assumption that the nuclear moment is positive. According to (5.9) of I, the sign of the nuclear quadrupole moment is opposite to that of $P$, and is thus negative.

The magnetic hyperfine coupling arises in part from the magnetic field of the $5f$ electron, and in part from small admixtures of $s$-states, which are due to perturbations such as configuration interaction. In the present case, there is a perturbation resulting in $s$-electron coupling, which we omitted in I, namely the $V_3^3$ term in the crystalline potential, which couples the $5f$, $m_l = \pm 3$ states to $s$-states ($7s$ antibonding or $8s$, etc.). This coupling leads to an additional contribution to the expressions (5.6) of I for $A$ and $B$.

Assuming, for illustration, that the ground state is given by

$$|a> = 0.8975\,|-3+> - 0.4262\,|-2-> - 0.1134\,|3+>, \text{ etc.}$$

we obtain

$$A = -(13.305 + 1.273\,\kappa - \kappa')\gamma\beta\beta_N < r^{-3} >$$

$$B = -(0.2589 + 0.4071\,\kappa - \kappa')\gamma\beta\beta_n < r^{-3} >$$

where $\kappa$ is the usual parameter characterizing $s$-electron admixture (through configuration interaction) and $\kappa'$ is a parameter describing the admixture through $V_3^3$. $\kappa'$ is probably small for it is quadratic in the admixture, unlike $\kappa$, which is linear [14].

Nothing is known about the magnitude of $\kappa$, but it seems unlikely to be appreciable. We may therefore make an estimate of the nuclear moment $\mu_N$ from the experimental value of $A$ by neglecting the $\kappa$ and $\kappa'$ terms. It is necessary to know $< r^{-3} >$.

Both $\zeta$ and $< r^{-3} >$ were calculated by Foglio and Pryce [15] on the basis of a Thomas-Fermi model. They concluded that this model leads to values of $\zeta$ and $< r^{-3} >$ which are too low, but that the calculated ratio $\zeta / < r^{-3} >$ is fairly accurate. If we take $\zeta / < r^{-3} > \sim 360$ cm$^{-1}$/atomic unit as indicated by their results and $\zeta \sim 2160$ cm$^{-1}$ as indicated by the previous discussion in this paper we find $< r^{-3} > \sim 6.0$ atomic units ($40 \times 10^{24}$ cm$^{-3}$)

We then obtain

$$\mu_N = \Upsilon I = \frac{5}{2} \frac{0.16547}{6.0 \times 1.5913 \times 10^{-3} \times 13.305}$$

$$= 3.2 \text{ nuclear magnetons.}$$

There are at least three sources of error here, apart from the experimental error in the determination of $A$:— error in $< r^{-3} >$, which we set at $\pm 20$ percent; error from neglecting $\kappa$ and $\kappa'$, which we set at $\pm 10$ percent; and error from (somewhat arbitrarily) using the ground state above, which however is negligible in comparison with the other two. We may therefore write

$$\mu_N = 3.2 + 0.9 \text{ n.m.}$$

## 7. Magnetic Susceptibility

The susceptibility can be written in the form

$$\chi = \frac{N\beta^2}{12k}(g_{\|}^2 + 2g_{\perp}^2) + a$$

here $k$ is the Boltzmann constant), provided the temperature is sufficiently low for the $| 2 - >$ level to be effectively unpopulated. We wish here to estimate the value of $a$, which is given by

$$a = \chi_{\text{core}} + \frac{2}{3} N\beta^2 \Sigma_i \frac{| < 0 | \mathbf{L} + 2\mathbf{S} | i > |^2}{(E_i - E_0)}.$$

The contribution of the core, $\chi_{\text{core}}$, we have previously estimated to be $57 \times 10^{-6}$ emu/mole.

The dominant term in this sum arises from the $| 2 - >$ level, because it is so low. With the parameters we have chosen for the ground state, and $k_3 = k_2 = 0.85$ we obtain for this dominant term

$$\frac{0.1248}{\Delta E(\text{cm}^{-1})} \text{ emu/mole.}$$

The contributions from the remaining leveis total about $25 \times 10^{-6}$. We therefore estimate

$$a \sim (82 + \frac{0.1248}{\Delta E}) \times 10^{-6} \text{ emu/mole.}$$

In Na $NpO_2(CH_3COO)_3$ the observed [6] value of $a$ is $194 \times 10^{-6}$. The calculated value of $a$ would also be $194 \times 10^{-6}$ if the $| 2 - >$ level were at 1100 cm$^{-1}$. This position for the $| 2 - >$ level is within the limits suggested by the calculations in section 4.

## 8. Conclusion

In this paper we have discussed the magnetic and spectroscopic properties of the neptunyl ion, and have presented an interpretation of these properties which is based on some hypotheses concerning the structure of the ion and its environment. The hypotheses seem to be fully justified a priori, by crystal structure data on uranyl and neptunyl compounds, and a posteriori, by detailed agreement between calculated and observed quantities.

We have dealt first with the solution absorption spectrum, and have shown how the spin-orbit coupling constant and the parameters of the ligand and crystal fields can be determined from the positions of the absorption peaks. We have pointed out an important ambiguity in the interpretation of the spectrum and have tried to indicate that there is uncertainty concerning the precise values of the parameters. The ambiguity and uncertainty stem partly from the complexity of the physical system involved and partly from the limited extent and accuracy of the experimental data. We have tried to treat, in a quantitative way, the effect of covalence on the positions of the energy levels.

The available magnetic data come from electron spin resonance experiments and from susceptibility measurements. We have shown that theoretical and experimental values for the spectroscopic splitting factors agree if a crystal field of appropriate symmetry and magnitude is present, and if covalent effects which effectively reduce the orbital angular momentum are also present. The same assumptions which lead to agreement of calculated and experimental values for the spectroscopic splitting factors lead also to agreement of calculated and experimental values for the susceptibility.

We believe the principal factors which determine the magnetic and spectroscopic properties of uranyl type ions are now known. Ligand field, crystal field, and covalent effects make the behavior of these ions rather complicated.

A second paper on the properties of the $(PuO_2)^{++}$ and the $NpO_2^+$ ions is being prepared. A more convincing interpretation than heretofore of the rather complex absorption spectra of these ions can now be given. Eventually a long deferred paper on the americyl and $PuO_2^+$ ions may follow.

---

We thank Clyde A. Hutchison, Jr., for many stimulating and enlightening discussions, and M. Fred for information and discussions concerning the absorption spectra.

## 9. Appendix

Plots of absorption spectra are usually given in terms of molecular extinction coefficient or absorbance as a function of wavelength. The molecular extinction coefficient $\epsilon$ is defined as follows:

$$\epsilon = \frac{-\log_{10}(\text{transmittancy})}{\text{Molarity} \times \text{length of cell (in cm)}}.$$

The transmittancy is defined as the ratio $I/I_0$ where $I$ is the radiant flux transmitted and $I_0$ is the radiant flux incident. The molarity is the number of gram molecular weights of the absorbing substance per liter of solution. The absorptance is [1 − transmittancy] and the absorbance is $\log_{10}$ (absorptance).

Another term in common use is the specific extinction, $k$. This is defined as

$$k = E/cd$$

where

$E$ = extinction = $\log_{10} I_0/I$

$c$ = concentration in grams/liter

$d$ = thickness of cell in cm.

Evidently $\epsilon$ = molecular weight $\times k$.

The energy absorbed per unit time at energy $h\nu$ is $Nwh\nu$ where $N$ is the number of absorbers and $w$ is the probability that a transition will take place. The energy absorbed per unit time at energy $h\nu$ per volume $V$ is $Nwh\nu/V$. For an oscillating magnetic field $\tilde{H}\cos\omega t$ the incident energy per cm$^2$ per sec is $c\tilde{H}^2/8\pi$. Hence

$$\frac{\dfrac{\text{Energy absorbed}}{\text{volume second}}}{\dfrac{\text{energy incident}}{\text{cm}^2\ \text{second}}} = \frac{\dfrac{wh\nu N}{V}}{\dfrac{c\tilde{H}^2}{8\pi}} = -\frac{dI}{Idy} = \alpha, \text{ say}$$

where

$$I = I_0 e^{-\alpha y}$$

or

$$\log_e I/I_0 = -\alpha y.$$

Let us put these relations into conformity with the previous notation. We use $d$ instead of $y$. Then

$$2.303 \log_{10} I/I_0 = -\alpha d.$$

But

$$-\log_{10} I/I_0 = E = k \times \text{concentration} \times d$$

$$= \epsilon \times \text{concentration} \times d/M,$$

$M$ being the molecular weight. Hence

$$\alpha = 2.303\epsilon \times \text{concentration}/M$$

and

$$\epsilon = \frac{M}{2.303 \times \text{concentration}} \frac{wh\nu N/V}{c\tilde{H}^2/8\pi}.$$

For magnetic dipole absorption we have

$$w = \frac{2\pi}{\hbar} \beta^2 \frac{\tilde{H}^2}{4} \rho(E_f)$$

where $\rho(E_f)$ is the density of final states per unit energy range. Hence since

$$\frac{\text{molecular weight}}{\text{grams/liter}} \frac{\text{number of absorbers}}{\text{cm}^3} = \frac{N_0}{1000}$$

we have

$$\epsilon = \frac{8\pi^3 N_0 \beta^2 \nu \rho\ (E_f)}{2303\ c}$$

$N_0$ is the Avogadro number.

As a measure of the strength of an absorption line we shall take

$$k \int \epsilon \frac{d\nu}{\nu}$$

where $k$ is a constant chosen to make the strength corresponding to a magnetic dipole transition equal to one. In terms of our previous formula we must have

$$k \int \frac{8\pi^3 N_0 \beta^2}{2303} \frac{\nu}{c} \rho(E_f) \frac{d\nu}{\nu} = 1$$

or

$$k = \frac{2303hc}{8\pi^3 \beta^2 N_0 \int \rho(E_f) dE_f}.$$

Since only one final state is accessible to a magnetic dipole we have

$$k = \frac{2303hc}{8\pi^3 \beta^2 N_0} = 35.587.$$

In practice it is sometimes inconvenient to calculate $\int \epsilon d\nu/\nu$ so we make the approximation that the absorption peaks have a Gaussian frequency distribution. It then follows that the area under the peaks is approximately

$$\int \frac{\epsilon d\nu}{\nu} = 1.064 \frac{\epsilon_{max} \Delta\nu}{\nu_0}$$

where $\Delta\nu$ is the width of the peak at half intensity, and $\epsilon_{max}$ is the molecular extinction coefficient at the frequency $\nu_0$ where the absorption is maximal. The strength of a Gaussian peak therefore is $37.9\ \epsilon_{max}\ \Delta\nu/\nu_0$.

Since we make considerable use of Waggener's spectroscopic measurements it is worth noting that he plots a quantity he calls "absorbance" versus wavelength. This quantity is in reality the extinction $\log_{10} I_0/I$.

## 10. References


[1] J. C. Eisenstein and M. H. L. Pryce, Proc. Roy. Soc. **A229,** 20 (1955) and 238, 31 (1956).
[2] J. C. Hindman, private communication.
[3] W. C. Waggener, J. Phys. Chem. **62,** 382 (1958).
[4] W. H. Zachariasen and H. A. Plettinger, Acta Cryst. **12,** 526 (1959).
[5] B. Bleaney, P. M. Llewellyn, M. H. L. Pryce, and G. R. Hall, Phil. Mag. **45,** 992 (1954).
[6] D. M. Gruen and C. A. Hutchison, J. Chem. Phys. **22,** 386 (1954).
[7] J. C. Eisenstein and M. H. L. Pryce, Proc. Roy. Soc. **A255,** 181 (1960).
[8] K. W. H. Stevens, Proc. Roy. Soc. **A219,** 542 (1953).
[9] J. Owen, Proc. Roy. Soc. **A227,** 183 (1955).
[10] K. D. Bowers and J. Owen, Rep. Progr. Phys. **18,** 304 (1955).
[11] C. A. Coulson and G. R. Lester, J. Chem. Soc. **1956,** 3650.
[12] G. H. Dieke and A. B. F. Duncan, Spectroscopic Properties of Uranium Compounds (National Nuclear Energy Series III, 2), New York (McGraw-Hill Book Co., New York, N.Y., 1949).
[13] A. Abragam and M. H. L. Pryce, Proc. Roy. Soc. **A205,** 135 (1951).
[14] A. Abragam, J. Horowitz and M. H. L. Pryce, Proc. Roy. Soc. **A230,** 169 (1955).
[15] M. E. Foglio and M. H. L. Pryce, Mol. Phys. **4,** 287 (1961).


(Paper 69A3–341)

JOURNAL OF RESEARCH of the National Bureau of Standards—A. Physics and Chemistry
Vol. 69A, No. 3, May–June 1965

# Heats of Transformations in Bismuth Oxide by Differential Thermal Analysis

**Ernest M. Levin and Clyde L. McDaniel**

(January 5, 1965)

DTA was chosen as a convenient method for resolving differences in the reported heat of transition and heat of fusion of $Bi_2O_3$. The heat of the low to high transition of $K_2SO_4$ (at 583 °C) and the heat of fusion of Ag (at 960.8 °C) were used as internal standards. These standards were mixed directly with the $Bi_2O_3$ in three weight ratios. The heating schedule for each weight ratio was 3°/min, 9°/min, and 3°/min. For evaluating internal consistency, DTA determinations were made for mixtures of the two standards. Linearity was obtained within limits between the weight ratio of $Bi_2O_3$ and standard and the corresponding ratio of peak areas. The heat of transition of $Bi_2O_3$ ($mon \xrightarrow{730\ °C} cubic$) was found to be $9.9 \pm 0.5$ kcal/mole and the heat of fusion ($cubic \xrightarrow{825\ °C} liq.$) $3.9 \pm 0.2$ kcal/mole. The uncertainties are estimated limits of error, based on internal consistency and on the values of the standards.

## 1. Introduction

By application of the Clausius-Clapeyron equation to the liquidus curve of the $Bi_2O_3$–PbO system [1],[1] K. K. Kelley determined the heat of fusion of $Bi_2O_3$ to be 6.8 kcal/mole [2]. This value is listed in tables of thermodynamic data [3, 4]. Levin and McDaniel [5] applying the same Clausius-Clapeyron equation to the $Bi_2O_3$–$B_2O_3$ system obtained a heat of fusion value of $2.0_5$ kcal/mole. Gattow and Schröder [6] and Gattow and Schütze [7] have used these two values in conjunction with differential thermal analysis (DTA) data to calculate the heat of transition of monoclinic- to cubic-bismuth oxide (see table 1). They found that the area of the peak representing the monoclinic to cubic transition was $4.10 \pm 0.11$ times the area of the peak representing the cubic to liquid transformation; and, consequently, the heat of transition should be 4.10 × the heat of fusion.

TABLE 1. *Heats of transformations in bismuth oxide*

| Investigator | Method | Heat of transformation | |
|---|---|---|---|
| | | Transition (mon → c) | Fusion (c → liq) |
| | | *kcal/mole* | *kcal/mole* |
| K. K. Kelley (1936) [2] | $Bi_2O_3$–PbO liquidus [1] | | 6.8 |
| Levin and McDaniel (1962) [5] | $Bi_2O_3$–$B_2O_3$ liquidus | | $2.0_5$ |
| Gattow and Schröder (1962) [6] | DTA[a] | 27.9 ± 1.0 | |
| Gattow and Schütze (1964) [7] | DTA[b] | 8.4 ± 0.3 | |
| Levin and McDaniel (1964) | DTA[c] | 9.9 ± 0.5 | 3.9 ± 0.2 |

[a] Heat of transformation = (4.10 ± 0.11) × heat of fusion (6.8 kcal/mole).
[b] Heat of transformation = (4.10 ± 0.11) × heat of fusion (2.05 kcal/mole).
[c] Using $K_2SO_4$ and Ag as internal standards.

[1] Figures in brackets indicate the literature references at the end of this paper.

The two reported values for the heat of fusion of $Bi_2O_3$ differ by a factor of about three. The value of 6.8 kcal/mole obtained from the $Bi_2O_3$–PbO diagram is suspect for two reasons: First, a reinvestigation of the $Bi_2O_3$–PbO system [8] has shown Belladen's simple liquidus diagram to be incorrect, inasmuch as PbO exists in solid solution with $Bi_2O_3$ at the liquidus. Second, the sum of the reported entropy of transition and of fusion, $\left(\frac{6800}{1098} + \frac{27900}{1003} \Big/ 5\right)$, is about 7 cal/°K/g atom, an abnormally high value.

Because of the increasing importance of $Bi_2O_3$ in the electronics and ceramics industries, it is desirable to verify the basic thermodynamic data. As equipment for direct calorimetric measurement was not available, differential thermal analysis, using internal standards, was selected as a convenient, independent method for determining heats of transformation.

## 2. Equipment

The differential thermal analysis equipment was built in the laboratory and is of conventional design. The furnace heating element consists of a ceramic core 10 in. long × 2⅜ in. o.d., wound with 20 gage, 80 percent Pt: 20 percent Rh, wire. Linear temperature rise with time is accomplished by means of a program controller and a pneumatically activated variable autotransformer. Heating rates of 3°/min and 9°/min are obtained by controlling the percentage of time during which the set point is driven. Using a multipoint recorder, the emfs of the sample thermocouple and of the differential thermocouple are plotted as a function of time. Determinations are made at overall sensitivities of 14 μV/in.

To minimize errors that might be caused by poor thermal diffusivity, a special holder assembly is used.

The two thermocouples (Pt—90 percent Pt:10 percent Rh) from the holder assembly are welded, near the bottom, to Pt containers. The containers are made from Pt tubing and measured 16 mm long × 2.6 mm i.d. × 3.0 mm o.d. The tubes contain a total of 0.2 to 0.4 g of material, depending on the substances and weight ratios studied. To reduce the effect of air currents in the furnace, the Pt tubes are covered with thin ceramic thimbles.

## 3. Method

The usual procedure for measuring heats of transformation by DTA depends on calibration of the equipment with a known weight of a standard, e.g., benzoic acid, $AgNO_3$, $KNO_3$ [9, p. 111] and [10, 11]. The calibration can be expressed in terms of calories per unit of integrated peak area, in the differential temp.-time curve representing the transformation. Assuming approximate constancy of the calibration factor, the unknown heat of transformation for a substance can be determined from the peak area in its differential temp.-time curve.

The method depends on conditions that are seldom closely realized. First, the geometry of the physical arrangement and other operating conditions should be exactly the same for the determination of the unknown as for the calibration with the standard. Second, and even more unlikely, such thermal properties as conductivity, diffusivity, and specific heat should be essentially identical for the two samples.

A method using internal standards avoids the problems inherent in a separate calibration method. Therefore, several high-purity chemicals, with appropriate temperatures and heats of transformations were tried, in a search for internal standards.

Two substances were found satisfactory for calibrants: (1) Finely ground crystalline $K_2SO_4$ with a heat of transition ($\alpha \xrightarrow{583\ °C} \beta$) of 2.14 kcal/mole [3, 12]. (2) Fine, precipitated Ag powder with a heat of fusion ($s \xrightarrow{960.8\ °C}$ liq.) of 2.61 kcal/mole [2] [13]. The transformation temperatures in these two substances bracket the transition temp. of $Bi_2O_3$ (monoclinic $\xrightarrow{730\ °C}$ cubic) and the fusion temp. of $Bi_2O_3$ (cubic $\xrightarrow{825\ °C}$ liquid). Two additional substances, NaCl and $Li_2SO_4$, were found to be unsatisfactory as internal calibration standards.

DTA experiments were carried out for $Bi_2O_3 : K_2SO_4$ mixtures in wt. ratios of 3.46 : 1, 1.72 : 1, and 1.00 : 1; and for $Bi_2O_3$ : Ag mixtures in wt ratios of 4.32 : 1, 2.16 : 1, and 2.00 : 1. Mixtures were made in 2g batches by shaking in a mechanical mixer accurately weighed amounts of dried starting materials. As will be shown below under "Derivation of Equations" the heat of transformation calculations are not based on the actual weights of the two substances in the sample holder but only on the formulated ratios.

Each mixture was given a preliminary heat-cycling treatment by heating the mixture at 12 °C/min to about 775 °C (above the transition of $K_2SO_4$ and $Bi_2O_3$ but below the melting point of $Bi_2O_3$) and then cooling to room temperature. The preliminary heat treatment was followed by three successive cycles of heating to above the mp of $Bi_2O_3$ in $K_2SO_4$ mixtures and above the mp of Ag in Ag mixtures. The heating and cooling rates for the three cycles were 3°/min, 9°/min, and 3°/min, respectively. Only the peak areas in heating curves were considered, as previous work, using both DTA and high-temperature x-ray techniques [14], had shown that the stable high-temperature cubic phase is supercooled below the equilibrium transition temperature of 730 °C: and at about 650 °C a metastable tetragonal and/or body-centered cubic phase is formed, which in turn, transforms back to the stable monoclinic form.

To check on the internal consistency of the method and to evaluate the accuracy, DTA determinations were made with mixtures of the two standards, at the same heating rates and at weight ratios of $K_2SO_4$ : Ag of 1.36:1 and 4.00:1.

It should be noted that a number of investigators [9] have used internal standards for quantitative estimation of a phase. Barshad [11] has proposed using "indicators" either mixed with the sample or in separate layers, for direct temperature calibration of a DTA curve. However, the use of internal standards for heat of reaction measurements as herein proposed has not been previously reported, according to the best knowledge of the authors.

An obvious and valid à priori criticism of the internal-standard method is the possibility of obtaining erroneous results if reaction occurs between the bismuth oxide and the standards during the heat-cycling treatments. This possibility was foreseen and was shown to be minimal by a number of observations.

(1) The ratio of the areas under the peaks representing the monoclinic to cubic transition and the cubic to liquid transformation for pure $Bi_2O_3$ could be compared with the corresponding ratio when standards were mixed with the $Bi_2O_3$.

(2) Ratios of corresponding areas for successive heat cycles could be compared with each other, and any discrepancies noted.

(3) At the conclusion of each series of determinations for a given weight ratio, the mixture was examined by x-ray powder diffraction techniques to check for any new phases that might have formed by reaction of the starting materials.

(4) Finally, experimental results could be checked for conformance to theory.

By the criteria listed above, it was possible to evaluate the individual experimental data and to eliminate the few values which were obviously in error. However, even in these instances, the evidence did not indicate chemical reaction of the $Bi_2O_3$, but pointed to physical factors.

## 4. Derivation of Equations

It can be shown that to a close approximation [9, p. 111] the total heat of reaction in a DTA determination

[2] The literature values reported for the heats of transformations in $K_2SO_4$ and Ag vary over a range of about 10 percent. The values selected here are shown later in this paper (see Internal Consistency) to be self-consistent.

is given by:

$$\Delta H = \frac{cK_s}{g} \int y dt = \frac{cK_s}{g} \cdot A \qquad (1)$$

where, $H$ = heat of transformation per g

$c$ = geometrical shape constant

$K_s$ = thermal conductivity of the sample

$g$ = mass of reactive component in sample

$\int y dt = A$ = peak area for the transformation.

If two substances, designated by subscripts 1 and 2, are considered in a mixture, eq (1) may be applied to each substance. Assuming no reaction between the substances, constancy in $c$, and approximate constancy in $K_s$ (now the combined thermal conductivity of the mixture), the following expression is readily obtained:

$$\frac{\Delta H_1}{\Delta H_2} = \frac{A_1 g_2}{A_2 g_1}. \qquad (2)$$

As $\Delta H_1$ and $\Delta H_2$ are constants, $g_2/g_1$ is the weight ratio of the binary mixture, as formulated, and $A_1/A_2$ is the experimentally measured peak area ratio of the two transformations, the basic equation for an unknown heat of transformation becomes:

$$\Delta H_1 = \Delta H_2 \left(\frac{g_2}{g_1}\right)\left(\frac{A_1}{A_2}\right). \qquad (3)$$

It may be noted that eq (3) is a straight line that passes through the origin and with slope, $m$, equal to $(A_1/A_2)/(g_1/g_2)$. Thus, over the range that the assumptions made in the derivation hold true, a linear relationship should exist between the formulated weight ratios and the corresponding measured peak area ratios.

If the heat of transformation is desired directly in kcal/mole rather than on a gram basis, eq (3) may be transformed to:

$$L_1 = L_2 \left(\frac{M_1}{M_2}\right)\left(\frac{A_1}{A_2}\right)\Big/\left(\frac{g_1}{g_2}\right) \qquad (4)$$

where, $L_1$ and $L_2$ are the heats of transformation of substances 1 and 2, respectively, in kcal/mole, and

$M_1$ and $M_2$ are the corresponding molecular weights.

Applying eq (4) to the specific case of $Bi_2O_3$ : $K_2SO_4$ mixtures:

$$L_{Bi_2O_3} = 2.14 \left(\frac{465.96}{174.27}\right)\left(\frac{A_{Bi_2O_3}}{A_{K_2SO_4}}\right)\Big/\left(\frac{g_{Bi_2O_3}}{g_{K_2SO_4}}\right) = 5.722 m_1 \qquad (5)$$

where, $L_{Bi_2O_3}$ refers to the heat of transformation (transition or fusion), in kcal/mole;

2.14 = the heat of transition of $K_2SO_4$, from the $\alpha$ to $\beta$ form, in kcal/mole;

465.96/174.27 = the molecular weight ratio of $Bi_2O_3$ to $K_2SO_4$; and

$m_1$ = the slope of the line obtained by plotting as ordinate the ratio of the peak areas representing the particular transformation of $Bi_2O_3$ to the transition of $K_2SO_4$ ($A_{Bi_2O_3}/A_{K_2SO_4}$) and plotting as abscissa the corresponding weight ratio of $Bi_2O_3$ to $K_2SO_4$ ($g_{Bi_2O_3}/g_{K_2SO_4}$).

Applying eq (4) to the case of $Bi_2O_3$: Ag mixtures:

$$L_{Bi_2O_3} = 2.61 \left(\frac{465.96}{107.87}\right)\left(\frac{A_{Bi_2O_3}}{A_{Ag}}\right)\Big/\left(\frac{g_{Bi_2O_3}}{g_{Ag}}\right) = 11.274 m_2 \qquad (6)$$

where, 2.61 = the heat of fusion of Ag, in kcal/mole,

465.96/107.87 = the molecular weight ratio of $Bi_2O_3$ to $K_2SO_4$, and $m_2$ is the slope of the line obtained by plotting $\frac{A_{Bi_2O_3}}{A_{Ag}}$ as ordinate versus $\frac{g_{Bi_2O_3}}{g_{Ag}}$ as abscissa.

Applying eq (4) to the case of mixtures of the two standards, $K_2SO_4$ and Ag:

$$L_{K_2SO_4} = 2.61 \left(\frac{174.27}{107.87}\right)\left(\frac{A_{K_2SO_4}}{A_{Ag}}\right)\Big/\left(\frac{g_{K_2SO_4}}{g_{Ag}}\right) = 4.217 m_3 \qquad (7)$$

where, $L_{K_2SO_4}$ = the heat of transition of $K_2SO_4$, in kcal/mole;

2.61 = the heat of fusion of Ag, in kcal/mole

174.27/107.87 = the molecular weight ratio of $K_2SO_4$ to Ag; and

$m_3$ = the slope of the line obtained by plotting $\frac{A_{K_2SO_4}}{A_{Ag}}$ as ordinate versus $\frac{g_{K_2SO_4}}{g_{Ag}}$ as abscissa.

Inasmuch as DTA determinations were made in binary combinations of the three substances, $Bi_2O_3$, $K_2SO_4$, and Ag, it is possible to evaluate the internal consistency of the method. From eqs (5), (6), and (7), where $m_1$, $m_2$, and $m_3$ are given in terms of the specific ratios, it follows that any one ratio can be determined independently from the other two, for example:

$$\frac{\frac{A_{Bi_2O_3}}{A_{Ag}} \cdot \frac{g_{Ag}}{g_{Bi_2O_3}} = \frac{A_{K_2SO_4}}{A_{Ag}} \cdot \frac{g_{Ag}}{g_{K_2SO_4}}}{\frac{A_{Bi_2O_3}}{A_{K_2SO_4}} \cdot \frac{g_{K_2SO_4}}{g_{Bi_2O_3}}} \qquad (8)$$

or $m_2/m_1 = m_3$. (9)

## 5. Results and Discussion

### 5.1. General

Figure 1 shows a reproduction of the DTA curve for one of the $Bi_2O_3 : K_2SO_4$ mixtures. The various transformations within the phases are labeled. Peak areas were obtained by tracing the curve on millimeter ruled graph paper and averaging several counts. The modification of the sample holder in conjunction with the amplification of the equipment was found to be sensitive to heat of reaction effects. In a 1 : 1 mixture of $Bi_2O_3 : K_2SO_4$, for example, 0.1192 g $K_2SO_4$ absorbed a calculated 1.4635 calories of heat at the transition and produced an area under the peak of 208 mm², or about 0.007 cal/mm². No corrections were applied to the area data for change in thermocouple (Pt-90 percent Pt : 10 percent Rh) sensitivity with temperature. Attempted corrections did not improve the results; furthermore, the use of two standards whose transformation temperatures bracketed those of $Bi_2O_3$ provided automatic compensation.

The experimentally determined transformation ratios for pure $Bi_2O_3$ and the binary mixtures between $Bi_2O_3$, $K_2SO_4$, and Ag are given in table 2. Transformation ratios as a function of weight ratios are plotted in figures 2, 3, and 4. Slopes of the lines and standard deviations of the slopes were determined by the method of least squares for lines passing through the origin. If the assumptions used previously in deriving the linear relationships hold, then the origin constitutes a valid fixed point, for obviously as $g_{Bi_2O_3}$ in the mixture approaches 0, so does $A_{Bi_2O_3}$ and consequently so do the ratios $g_{Bi_2O_3}/g_{K_2SO_4}$ and $A_{Bi_2O_3}/A_{K_2SO_4}$.

Examining the transformation ratios (table 2) as a function of the 3°/min and 9°/min heating rates or as a function of the heating cycle (1st, 2d, or 3d), no overall trend of statistical significance can be discerned. The average ratios of the $Bi_2O_3$ transformations ($M \rightarrow c/c \rightarrow 1$) of 2.54 and 2.52 for the $Bi_2O_3 : K_2SO_4$ mixtures and of 2.53 for the $Bi_2O_3$ : Ag mixture (4.32 : 1) are in good agreement with each other and with that for pure $Bi_2O_3$, 2.46. However, the ratios of 3.20 and 2.80 for the $Bi_2O_3$ transformations in the Ag mixtures (2.16 : 1 and 2.00 : 1) appear high. The heat of fusion of $Bi_2O_3$ is 2/5 that of the heat of transition, and the shape of the fusion peak tends to be low and flat (see fig. 1). Therefore, as the amount of $Bi_2O_3$ decreases in the mixture, the peak area for fusion becomes less defined and broader tending to give a low area count.

It may be noted in figure 2 for the $Bi_2O_3 : K_2SO_4$ mixtures that the curves deviate from linearity above a 2 : 1 wt ratio of $Bi_2O_3 : K_2SO_4$. This deviation is not due to any significant reaction between $Bi_2O_3$ and $K_2SO_4$ but to poor thermal properties of the $Bi_2O_3$ mixture. For the mixtures containing Ag, which is a good thermal conductor and which has been used to improve thermal transfer [9, 15], linearity extends beyond the 4 : 1 ratio of substance to Ag (fig. 3 and 4). Therefore, the area ratios for the 3.46 to 1 wt ratio of $Bi_2O_3$ to $K_2SO_4$ were not used in computing the slopes.

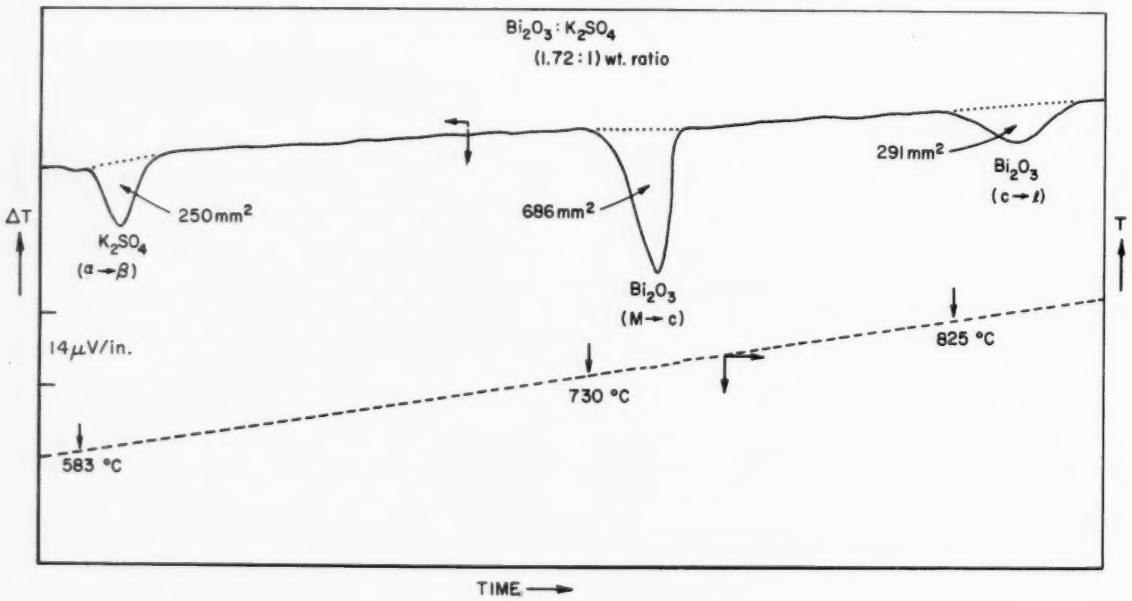


FIGURE 1. *Differential thermal analysis curve for third cycle of heat treatment of* $Bi_2O_3 : K_2SO_4$ *mixtures of weight ratio 1.72 : 1.*

Approx. 0.2 g of sample in Pt tube was heated in air at 3°/min. The temperature of sample container was measured with Pt – 90 percent Pt: 10 percent Rh thermocouple; reference material was compacted alumina powder. Areas under peaks were obtained by counting squares in tracings of the peaks on millimeter ruled graph paper.
$\alpha \rightarrow \beta$ = transition of $K_2SO_4$
$M \rightarrow c$ = monoclinic to cubic transition of $Bi_2O_3$
$c \rightarrow l$ = fusion of cubic $Bi_2O_3$.

TABLE 2. *Ratio of peak areas between transformations in* $Bi_2O_3$ *and in binary mixtures of* $Bi_2O_3$, $K_2SO_4$, *and* Ag, *as a function of heating rates and weight ratios**

| Composition wt. ratio | Transformation ratios [a] $A_1/A_2$ | Ratio of peak areas at heating rates: 3°/min | 9°/min | 3°/min | Average |
|---|---|---|---|---|---|
| **$Bi_2O_3$ (pure)** | | | | | |
| | $\frac{M \rightarrow c}{c \rightarrow l}$ | 2.47 | 2.57 | 2.33 | 2.46 |
| **$Bi_2O_3$ : $K_2SO_4$ mixtures** | | | | | |
| 77.6 $Bi_2O_3$ / 22.4 $K_2SO_4$ (3.46 : 1) | $\frac{M \rightarrow c}{c \rightarrow l}$ | 2.86 | 2.18 | 2.58 | 2.54 |
| | $\frac{M \rightarrow c}{\alpha \rightarrow \beta}$ | 4.67 | 4.87 | 4.57 | 4.70 |
| | $\frac{c \rightarrow l}{\alpha \rightarrow \beta}$ | 1.63 | 2.23 | 1.92 | 1.93 |
| 63.3 $Bi_2O_3$ / 36.7 $K_2SO_4$ (1.72 : 1) | $\frac{M \rightarrow c}{c \rightarrow l}$ | 2.51 | 2.70 | 2.36 | 2.52 |
| | $\frac{M \rightarrow c}{\alpha \rightarrow \beta}$ | 3.03 | 2.94 | 2.74 | 2.90 |
| | $\frac{c \rightarrow l}{\alpha \rightarrow \beta}$ | 1.21 | 1.09 | 1.16 | 1.15 |
| 50.0 $Bi_2O_3$ / 50.0 $K_2SO_4$ (1.00 : 1) | $\frac{M \rightarrow c}{\alpha \rightarrow \beta}$ [b] | 1.61 | 1.61 | 1.62 | 1.61 |
| **$Bi_2O_3$ : Ag mixtures** | | | | | |
| 81.2 $Bi_2O_3$ / 18.8 Ag (4.32 : 1) | $\frac{M \rightarrow c}{c \rightarrow l}$ | 2.56 | 2.52 | 2.51 | 2.53 |
| | $\frac{M \rightarrow c}{s \rightarrow l}$ | 3.91 | 3.82 | 3.96 | 3.90 |
| | $\frac{c \rightarrow l}{s \rightarrow l}$ | 1.52 | 1.51 | 1.58 | 1.54 |
| 68.35 $Bi_2O_3$ / 31.65 Ag (2.16 : 1) | $\frac{M \rightarrow c}{c \rightarrow l}$ | 3.10 [c, d] | 3.29 [d] | ..... | 3.20 [d] |
| | $\frac{M \rightarrow c}{s \rightarrow l}$ | 2.14 [c] | 1.68 | ..... | 1.91 |
| | $\frac{c \rightarrow l}{s \rightarrow l}$ | 0.69 [c] | 0.51 | ..... | 0.60 |
| 66.7 $Bi_2O_3$ / 33.3 Ag (2.00 : 1) | $\frac{M \rightarrow c}{c \rightarrow l}$ | ..... | 2.80 | ..... | 2.80 [d] |
| | $\frac{M \rightarrow c}{s \rightarrow l}$ | 1.99 | 1.72 | ..... | 1.86 |
| | $\frac{c \rightarrow l}{s \rightarrow l}$ | ..... | 0.61 | ..... | 0.61 |
| **$K_2SO_4$ : Ag mixtures** | | | | | |
| 57.7 $K_2SO_4$ / 42.3 Ag (1.36 : 1) | $\frac{\alpha \rightarrow \beta}{s \rightarrow l}$ | 0.637 | 0.638 | 0.604 | 0.626 |
| 80.0 $K_2SO_4$ / 20.0 Ag (4.00 : 1) | $\frac{\alpha \rightarrow \beta}{s \rightarrow l}$ | 2.27 | 2.16 | 2.07 | 2.17 |

*Sample weights varied from 0.2 to 0.4 g, depending on the particular mixtures. Samples were contained in Pt tubes and heated in air. Sensitivity on the differential temperature scale was 14 $\mu$v/in.

[a] Refers to ratio of peak areas between the indicated transformations:
$M \rightarrow c$, monoclinic to cubic transition of $Bi_2O_3$ phase at 730 °C
$c \rightarrow l$, cubic to liquid transformation of $Bi_2O_3$ phase at 825 °C
$\alpha \rightarrow \beta$, low to high transition of $K_2SO_4$ phase at 583 °C
$s \rightarrow l$, solid to liquid transformation of Ag phase at 960.8 °C.

[b] No values for $\frac{M \rightarrow c}{c \rightarrow l}$ and $\frac{c \rightarrow l}{\alpha \rightarrow \beta}$ ratios as $c \rightarrow l$ transformation of $Bi_2O_3$ is not well defined.

[c] 12°/min heating rate.

[d] Area for $c \rightarrow l$ transformation of $Bi_2O_3$ appears low.

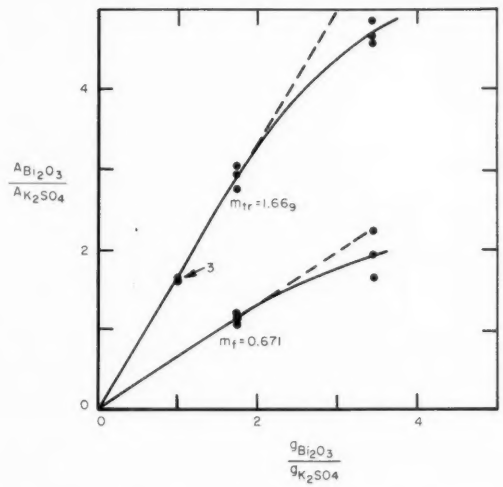


FIGURE 2. *Peak area ratios versus weight ratios for mixtures of* $Bi_2O_3$ *and* $K_2SO_4$.

$g_{Bi_2O_3}/g_{K_2SO_4}$ refers to the weight ratio. $A_{Bi_2O_3}/A_{K_2SO_4}$ for slope of line $m_{tr}$ refers to area under transition of $Bi_2O_3$ ÷ area under transition of $K_2SO_4$. $A_{Bi_2O_3}/A_{K_2SO_4}$ for slope of line $m_f$ refers to area under fusion of $Bi_2O_3$ ÷ area under transition of $K_2SO_4$. Slopes calculated by method of least squares.

$L_{Bi_2O_3} = 5.722 m_1$ (see eq (5), in text).
$L_{tr}Bi_2O_3 = 5.722 \times 1.66_9 = 9.5_5$ kcal/mole. S.D. $m_{tr} = 0.031$.
$L_fBi_2O_3 = 5.722 \times 0.671 = 3.8_4$ kcal/mole. S.D. $m_f = 0.020$.

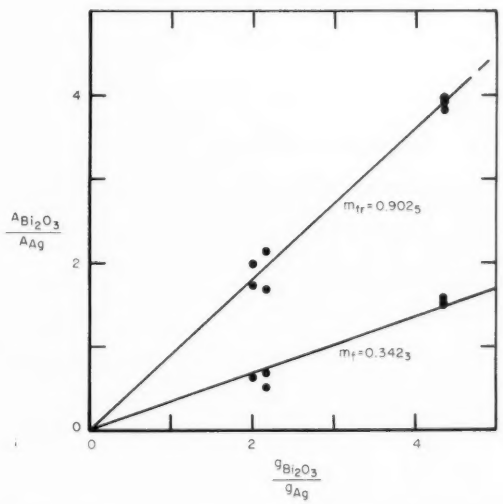


FIGURE 3. *Peak area ratios versus weight ratios for mixtures of* $Bi_2O_3$ *and* Ag.

$g_{Bi_2O_3}/g_{Ag}$ refers to the weight ratio. $A_{Bi_2O_3}/A_{Ag}$ for slope of line $m_{tr}$ refers to area under transition of $Bi_2O_3$ ÷ area under fusion of Ag. $A_{Bi_2O_3}/A_{Ag}$ for slope of line $m_f$ refers to area under fusion of $Bi_2O_3$ ÷ area under fusion of Ag. Slopes calculated by method of least squares.

$L_{Bi_2O_3} = 11.274 m_2$ (see eq (6), in text).
$L_{tr}Bi_2O_3 = 11.274 \times 0.902_5 = 10.1_7$ kcal/mole. S.D. $m_{tr} = 0.019$.
$L_fBi_2O_3 = 11.27 \times 0.342_3 = 3.8_6$ kcal/mole. S.D. $m_f = 0.015$.

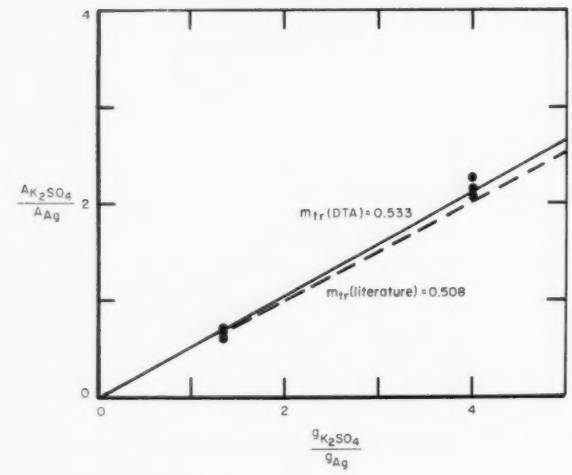


FIGURE 4. *Peak area ratios versus weight ratios for mixtures of* $K_2SO_4$ *and* Ag.

$g_{K_2SO_4}/g_{Ag}$ refers to the weight ratio. $A_{K_2SO_4}/A_{Ag}$ for slope of line $m_{tr}$ (DTA) refers to the area under the transition of $K_2SO_4$ ÷ area under the fusion of Ag. Slope for solid line calculated by method of least squares; slope for dashed line calculated from literature values.
$L_{K_2SO_4} = 4.217 m_3$ (see eq (7), in text).
$L_{tr} K_2SO_4 = 4.217 \times 0.533 = 2.2_5$ kcal/mole. S.D. $m_{tr} = 0.014$.
$L_{tr} K_2SO_4$, from literature [3, 12] = 2.14 kcal/mole.

## 5.2. Heats of Transformations

By application of eq (5) to the slopes in figure 2:

$$L_{tr} Bi_2O_3 (M \rightarrow c) = 5.722 \times 1.669 = 9.5_5 \text{ kcal/mole}$$

$$\text{S.D. } m_{tr} = 0.031 \text{ (0.30 kcal/mole)}$$

$$L_f Bi_2O_3 (c \rightarrow l) = 5.722 \times 0.671 = 3.8_4 \text{ kcal/mole}$$

$$\text{S.D. } m_f = 0.020 \text{ (0.08 kcal/mole)}$$

Similarly, by application of eq (6) to the slopes for the $Bi_2O_3$ : Ag mixtures (fig. 3):

$$L_{tr} Bi_2O_3 (M \rightarrow c) = 11.274 \times 0.9025 = 10.1_7 \text{ kcal/mole}$$
$$\text{S.D. } m_{tr} = 0.019 \text{ (0.19 kcal/mole)}$$

$$L_f Bi_2O_3 (c \rightarrow l) = 11.274 \times 0.3423 = 3.8_6 \text{ kcal/mole}$$

$$\text{S.D. } m_f = 0.015 \text{ (0.06 kcal/mole).}$$

The standard deviations of the slopes for the $Bi_2O_3$ : Ag mixtures are somewhat lower than for the $Bi_2O_3$ : $K_2SO_4$ mixtures because of the additional data, for the high weight ratio, that could be used in the calculations. Certainly, the difference in the heat of fusion of $Bi_2O_3$ obtained from the two standards is not statistically significant. The difference in values for the heat of transition is of questionable significance.

## 5.3. Accuracy

The linear relationship between area ratios and weight ratios for mixtures of the two standards can be seen in figure 4. The experimentally determined slope (0.533) is 4.7 percent greater than the theoretical slope (0.508) derived from the literature values. The difference between slopes is about twice the standard deviation of the experimentally determined slope. The agreement is good considering that the binary mixture of standards presents the most extreme in physical conditions of the three binary mixtures. In the $K_2SO_4$ : Ag mixtures, the area of the solid-solid transition of $K_2SO_4$ at 583 °C is compared to the area of the solid-liquid transformation of Ag at 960.8 °C.

Substituting in eq (7) the slope of the transformation ratio shown in figure 4 (0.533) gives a value of 2.25 kcal/mole for the heat of transition of $K_2SO_4$, compared to 2.14, the literature value. The agreement between these two values, as well as for the slopes, tends to substantiate the standard values used in the calculations, namely, 2.61 kcal/mole for $L_f$ of Ag and 2.14 kcal/mole for $L_{tr}$ of $K_2SO_4$. Attempts to correct for the change in thermocouple sensitivity with temperature or the use of other literature values for the heats of transformation of the standards has a detrimental effect on the agreement.

## 5.4. Internal Consistency

As shown in the development of eqs (8) and (9), it is possible to check the internal consistency of the results through a calculation which does not involve any heat of transformation values. From eqs (8) and (9):

$$\frac{m_2}{m_1} = m_3 = \frac{A_{K_2SO_4}}{A_{Ag}} \cdot \frac{g_{Ag}}{g_{K_2SO_4}}.$$

Substituting the values for the slopes $m_1$, $m_2$, and $m_3$, as given in figures 2, 3, and 4, respectively: For transition data, $\frac{0.902_5}{1.66_9} = 0.541$ (calc.) versus 0.533 (expt.). For fusion data, $\frac{0.342_3}{0.67_1} = 0.510$ (calc.) versus 0.533 (expt.).

The internal consistency calculations give deviations between the experimentally determined slope, $m_3$, and the calculated one, $m_2/m_1$, of +1.5 percent, for the transition data and −4 percent for the fusion data. The average of the two calculated slopes agrees to better than 1.5 percent with the experimentally determined one.

## 5.4. Conclusion

Consideration of the three criteria, namely, standard deviation of the slopes, internal consistency, and accuracy, as determined with the binary mixtures of standards, indicate an overall uncertainty of about 5 percent.

Averaging the results for the heats of transformation of $Bi_2O_3$ obtained from the mixtures with $K_2SO_4$ and Ag, yields:

$$L_{tr}Bi_2O_3(M \rightarrow c) = 9.9 \pm 0.5 \text{ kcal/mole}$$

$$L_fBi_2O_3(c \rightarrow l) = 3.9 \pm 0.2 \text{ kcal/mole}$$

The sum of the entropy of transition and of fusion equals $\left(\frac{9900}{1003} + \frac{3900}{1098}\right) \Big/ 5 = 2.7$ cal/°K/g atom, a reasonable value [3].

## 6. Summary

To avoid problems inherent in a separate heat of reaction calibration of DTA equipment, a technique was developed which makes use of internal standards.

Binary mixtures of $Bi_2O_3$ and two standards, $K_2SO_4$ and Ag, were formulated in three weight ratios and subjected to three cyclic heat treatments, in the DTA equipment. Small amounts of mixtures, 0.2 to 0.4 g in total weight, were heated in platinum tubes which were isolated from the tubes containing the reference material, $Al_2O_3$. Thermocouples, Pt-90 percent Pt:10 percent Rh, of fine wire were welded to the outside of the tubes. The modification of the sample holder and overall sensitivity of the equipment was found to respond to heat effects equivalent to 0.007 cal per $mm^2$ of the area under the peak.

A number of criteria were employed to check on possible reaction between $Bi_2O_3$ and the standards and to eliminate erroneous date. These criteria were as follows: Comparison of corresponding transformation ratios in successive heat cycles; comparison of the transformation ratio ($M \rightarrow c/c \rightarrow l$) in the $Bi_2O_3$ phase of mixtures with that in pure $Bi_2O_3$; x-ray powder analysis of mixtures at the completion of a determination; and, finally, observing the adherence of the data to linearity as prescribed by theory.

Except for the high weight ratio of $Bi_2O_3$ to $K_2SO_4$ in the 3.46:1 mixture, plots of ratios of transformation areas versus corresponding weight ratios were linear and passed through the origin. The presence of Ag in the $Bi_2O_3$:Ag and the $K_2SO_4$:Ag mixtures contributed to thermal transfer, and linearity was observed for all the weight ratios.

The data were analyzed according to (1) standard deviation of the slopes, (2) internal consistency, which is independent of the heat of transformation of the standards, and (3) agreement between calculated and selected literature value when one standard is mixed with the other. The heat of transition of $Bi_2O_3$ was found to be $9.9 \pm 0.5$ kcal/mole and the heat of fusion, $3.9 \pm 0.2$ kcal/mole. The uncertainties are estimated limits of error, based on internal consistency and on the values of the standards.

The authors express their sincere appreciation to Joan R. Rosenblatt of the Statistical Engineering Section, who was consulted on the statistical analysis of the data.

## 7. References

[1] L. Belladen, Il sistema $Bi_2O_3$-PbO (The System $Bi_2O_3$-PbO), Gazz. chim. ital. **52,** II, 160–164 (1922).

[2] K. K. Kelley, Contributions to Data on Theoretical Metallurgy: V, Heats of Fusion of Inorganic Substances, U.S. Bur. Mines Bull., No. 393, 166 pp. (1936); p. 26; Ceram. Abstr. **16** [5] 162 (1937).

[3] O. Kubaschewski and E. LL. Evans, Metallurgical Thermochemistry, 426 pp, 3d ed., rev. (Pergamon Press, New York, 1958).

[4] F. D. Rossini, D. D. Wagman, W. H. Evans, S. Levine, and I. Jaffee, Selected Values of Chemical Thermodynamic Properties, NBS Cir. 500, (1952) 1268 pp.

[5] E. M. Levin and C. L. McDaniel, The System $Bi_2O_3$-$B_2O_3$, J. Am. Ceram. Soc. **45** [8] 355–360 (1962).

[6] G. Gattow and H. Schröder, "Über Wismutoxide, III, Die Kristallstruktur der Hochtemperaturmodifikation von Wismut (III)-oxid ($\delta$-$Bi_2O_3$)", Z. anorg. allg. Chem. **318** [3–4] 176–189 (1962).

[7] G. Gattow and D. Schütze, Über Wismutoxide, VI, Über ein Wismut (III)-oxid mit höherem Sauerstoffgehalt ($\beta$-Modifikation), Z. anorg. allg. Chem. **328,** [1–2] 45–67 (1964).

[8] E. M. Levin and R. S. Roth, Polymorphism of bismuth sesquioxide. II. Effect of oxide additions on the polymorphism of $Bi_2O_3$, J. Res. NBS **68A** (Phys. and Chem) No. 2, 197–206 (1964).

[9] W. J. Smothers and Yao Chiang, Differential Thermal Analysis: Theory and Practice, 444 pp (Chemical Publ. Co., Inc., New York, 1958).

[10] F. C. Kracek, The polymorphism of potassium nitrate, J. Phys. Chem. **34,** 225–47 (1930).

[11] Isaac Barshad, Temperature and heat of reaction calibration of the differential thermal analysis apparatus, Am. Mineral. **37** [7&8] 667–694 (1952).

[12] K. K. Kelley, Contributions to the Data on Theoretical Metallurgy. XIII. High-Temperature Heat-Content, Heat-Capacity, and Entropy Data for the Elements and Inorganic Compounds, U.S. Bur. Mines Bull. 584, 1960. 232 pp.

[13] (a) Cavallaro, Atti Real. Acad. Ital., Rend. Class Sci., Fiz., Mat. et Nat. [**4–5**] 520–526 (1934). (b) F. E. Wittig, Z. Elektrochem. **54,** 288 (1950). (c) W. Oelson, Arch. Eisenhüttenw. **28,** 1–6 (1957).

[14] Ernest M.Levin and Robert S. Roth, Polymorphism of bismuth sesquioxide. I. Pure $Bi_2O_3$, J. Res. NBS **68A** (Phys. and Chem.) No. 2, 189–195 (1964).

[15] C. J. Penther, S. T. Abrams, and F. H. Stross, Semi-automatic Thermal Analysis Apparatus, Anal. Chem. **23,** 1459–66 (1951).

(Paper 69A3–342)

JOURNAL OF RESEARCH of the National Bureau of Standards—A. Physics and Chemistry
Vol. 69A, No. 3, May–June 1965

# Phase Relations Between Iridium and the Sesquioxides in Air

S. J. Schneider, J. L. Waring, and R. E. Tressler[1]

(February 11, 1965)

A study has been made by x-ray diffraction analysis of the reactions that occur in an air environment between Ir and $IrO_2$ and each of the following: $Nd_2O_3$, $Sm_2O_3$, $Eu_2O_3$, $Gd_2O_3$, $Dy_2O_3$, $Ho_2O_3$, $Y_2O_3$, $Er_2O_3$, $Tm_2O_3$, $Yb_2O_3$, $Lu_2O_3$, $In_2O_3$, $Sc_2O_3$, and $Al_2O_3$. In air Ir oxidizes at low temperatures to form $IrO_2$ which in turn dissociates at 1020 °C. The pseudo binary $Nd_2O_3$-$IrO_2$ was studied in detail inasmuch as it typified many of the $Ln_2O_3$-$IrO_2$ systems. Two compounds, $Nd_2O_3 \cdot 2IrO_2$ and $3Nd_2O_3 \cdot 2IrO_2$ occur in the system. The former, a cubic pyrochlore type phase, dissociates upon heating at 1190 °C. The 3:2 compound dissociates to the solid phases, $Nd_2O_3$ and Ir, at 1300 °C. Prior to dissociation, the 3:2 compound undergoes an apparent polymorphic transition at 1195 °C which may be related to an oxygen loss. Up to at least 2000 °C no further reaction occurred between Ir and $Nd_2O_3$. All B- and C-type rare earth oxides formed cubic pyochlore type compounds with $IrO_2$. Each of these compounds subsequently dissociated upon heating. No apparent reaction occurred between $IrO_2$ and either $In_2O_3$, $Sc_2O_3$, or $Al_2O_3$.

## 1. Introduction

As part of the program at the National Bureau of Standards to obtain accurate melting points of the metal oxides [1][2], a study has been initiated to determine what effect, if any, various refractory metal containers have upon possible standard oxides. The type of reaction between appropriate container materials such as iridium (Ir) or tungsten (W) and an oxide can be best characterized through a thorough study of their equilibrium phase relations. As the first in a series of phase equilibria investigations, the present paper reports results obtained in a study of portions of the Nd-Ir-Oxygen and related systems in an air environment.

Preliminary information indicated that powdered Ir has a tendency to oxidize to $IrO_2$ when heated in air at moderate temperatures. Since complete oxidation is difficult to achieve, $IrO_2$ rather than Ir metal was selected as one end member of the system. By utilizing $IrO_2$, an approach to equilibrium could be achieved more readily. The study would still reflect, however, the behavior in air of Ir metal in combination with $Nd_2O_3$ and other oxides.

Iridium has a face-centered cubic, copper type structure with $a=3.8394$ Å [2]. The freezing point of Ir is 2443 °C, a value which is given as a secondary reference point on the International Practical Temperature Scale (IPTS)[3] [3]. Iridium dioxide ($IrO_2$) is similar to $TiO_2$ in having the tetragonal, rutile structure with $a=4.4983$ Å and $c=3.1544$ Å [4]. Upon heating, $IrO_2$ has been reported to dissociate to the metal and a vapor phase at 1100 °C in one atmosphere oxygen [5].

Neodymium sesquioxide ($Nd_2O_3$) has been reported to occur in three polymorphic forms; the A, B, and C rare earth oxide structure types [6, 7]. The hexagonal A type ($a=3.831$ Å, $c=5.999$ Å) [8], is generally regarded as the stable modification of $Nd_2O_3$ although there has been some controversy regarding the existence and stability of the B and C types [6, 7]. The melting point of $Nd_2O_3$ is not well established. The one value reported in the literature lists the melting point as 2272 °C for material having a purity of 99 percent [9].

Since little data are available on either Ir of $IrO_2$ in combination with oxides, the present study was broadened somewhat to include, in addition to $Nd_2O_3$, the following materials: $Sm_2O_3$, $Eu_2O_3$, $Gd_2O_3$, $Dy_2O_3$, $Ho_2O_3$, $Y_2O_3$, $Er_2O_3$, $Tm_2O_3$, $Yb_2O_3$, $Lu_2O_3$, $In_2O_3$, $Sc_2O_3$, and $Al_2O_3$.

[1] Mr. Tressler is currently a graduate student at Pennsylvania State University.
[2] Figures in brackets indicate the literature references at the end of this paper.
[3] This scale (IPTS) applies to all temperatures listed in this paper.

## 2. Materials

All starting materials employed in this study had a purity of 99.7 percent or greater. With the exception of Ir, $IrO_2$, and $Al_2O_3$, the oxides were used in previous investigations and their spectrochemical analyses are reported elsewhere [10, 11, 12]. The Ir, $IrO_2$, and $Al_2O_3$ samples were found by general qualitative spectrochemical analysis [4] to have the following impurities:

Ir 0.01–0.1% each Pd, Pt and Si;
0.001–0.01% each of Ag, Cu, and Fe;
0.0001–0.001% each Al and Mg;
and < 0.0001%, Ca.

$IrO_2$ 0.01–0.1%, Pt;
0.001–0.01% each Al, Cu, Fe, Pd, and Si;
0.0001–0.001% Mg; and < 0.0001% Ca.

$Al_2O_3$ 0.01–0.1% each Ga, Pb and Si;
0.001–0.01% each Cu, Fe, and Mg;
0.0001–0.001% each Ag, Ca, and Cr.

## 3. Experimental Procedure

Specimens for the oxide-$IrO_2$ studies were prepared from 0.5 g batches of various combinations of the end members. Calculated amounts of each oxide, corrected for ignition loss, were weighed to the nearest milligram. Each batch was thoroughly hand mixed, placed in Pt tubes and fired at 800 or 1000 °C a minimum of 19 hr in a muffle furnace.

Following the preliminary heat treatment, a portion of each calcined batch was placed in a small Vycor tube (sealed at one end) and fired in a Pt alloy quench furnace at various temperatures for different periods of time until equilibrium was attained. The Vycor tube containing the specimen was air quenched by quickly pulling the tube from the furnace. Equilibrium was assumed to have been achieved when the x-ray pattern showed no change after successive heat treatments of a specimen or when the data were consistent with the results from a previous set of experiments.

The use of Vycor tubes instead of Pt for experiments above 1000 °C was necessitated by the fact that Ir, frequently found as a decomposition product, readily reacts with Pt. On the other hand, the Vycor tube did not appear to influence or react with the various oxide samples.

Temperatures in the quench furnace, controlled to within ±3 °C, were measured with a 100 percent Pt versus 90 percent Pt–10 percent Rh thermocouple. All reported temperatures pertaining to quench furnace data are considered accurate to within ±5 °C.

[4] The spectrochemical analyses were performed by the Spectrochemical Analysis Section of the National Bureau of Standards.

Several experiments were conducted with mixtures having 1:2 mole ratios of oxide to Ir metal. Specimens of this type were prepared from two gram batches. After each batch was mechanically mixed it was heat treated at three different temperatures; specifically, 1000 °C for 12 hr, 1400 °C for 1 hr and ≈ 2000 °C for 1/2 hr. A small iridium pellet was used as a setter material. A program controlled tube furnace was employed for the 1000 and 1400 °C treatments. An induction furnace [11] utilizing an iridium crucible as both the susceptor and specimen container was used for the 2000 °C treatment. Temperatures were measured with a calibrated optical pyrometer sighted through a small hole in the crucible cover. The optical pyrometer temperature measurements are estimated to be accurate to within ±25 °C or better.

All specimens were examined by x-ray diffraction techniques at room temperature using a high angle recording Geiger counter diffractometer and Ni-filtered Cu radiation.

## 4. Results and Discussion

### 4.1. $Nd_2O_3$–$IrO_2$ and $Nd_2O_3$–Ir Systems in Air

The equilibrium phase diagram for the combined $Nd_2O_3$–$IrO_2$ and $Nd_2O_3$–Ir systems in air is given in figure 1. The diagram was constructed from the data listed in table 1. The solid circles indicate the compositions and temperatures of the experiments conducted. It should be emphasized that figure 1 does not represent a true binary system, but a composite of the true binary, $Nd_2O_3 - Ir$, and the pseudo binary, $Nd_2O_3$–$IrO_2$, in the Nd–Ir–Oxygen ternary system. At the lower temperatures the oxygen content of the specimens closely conform to the compositions represented by the pseudo binary $Nd_2O_3 - IrO_2$ system. As the temperature is increased, the compositions of the solid phases change by an apparent oxygen loss to those indicated by the $Nd_2O_3$–Ir join. By considering this dissociation as a type of phase transition in which the vapor phase is ignored, a simple binary representation of the phase relations in a portion of the ternary system can be given. This method of illustration has been employed by a number of investigators, notably A. Muan in his work on iron oxides [13, 14].

At 1020 ± 5 °C in an air environment at atmospheric pressure, $IrO_2$ was found to dissociate to one solid phase, Ir metal. This value favorably compares with the 1015 °C dissociation temperature at 160 mm Hg oxygen pressure calculated from the data given by Cordfunke and Meyer in their study of the Ir–Oxygen system [5]. The dissociation of $IrO_2$ is apparently a reversible process. For practical purposes the dissociation can be represented as a type of polymorphic transformation.

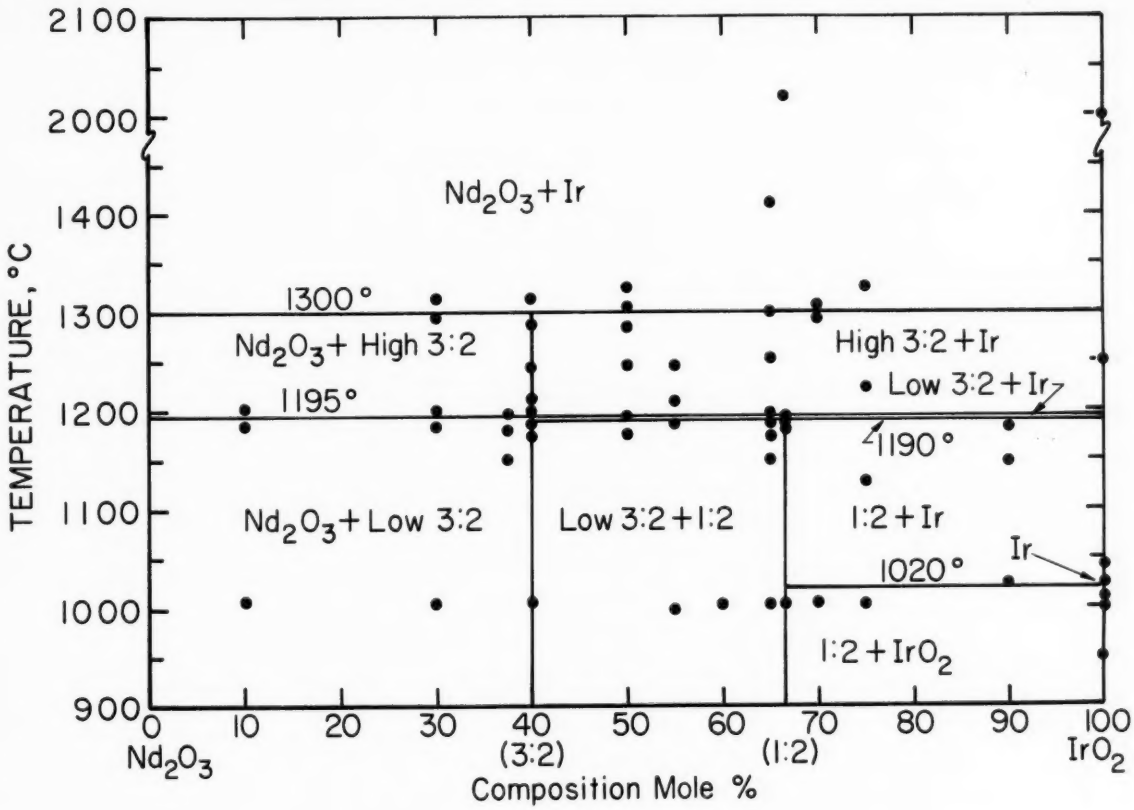


FIGURE 1. *Composite phase equilibrium diagrams for the* $Nd_2O_3$–$IrO_2$ *and* $Nd_2O_3$–Ir *systems in air.*

●–compositions and temperatures of experiments conducted in an air environment.

Low 3:2–$3Nd_2O_3 \cdot 2IrO_x$.

High 3:2–$3Nd_2O_3 \cdot 2IrO_x$; x is probably less than 2.

1:2–$Nd_2O_3 \cdot 2IrO_2$ (pyrochlore type compound).

Ir–iridium metal.

TABLE 1. *Experimental data for compositions in the* $M_2O_3$–$IrO_2$ *and* $M_2O_3$–Ir *systems in air*

| System | Composition | Heat treatment | | X-ray diffraction analyses[b] | Remarks |
|---|---|---|---|---|---|
| | | temp.[a] | Time | | |
| | *Mole %* | *°C* | *hr* | | |
| $Nd_2O_3$–$IrO_2$ | 90:10 | 1009 | 19 | $Nd_2O_3$ + low $3Nd_2O_3 \cdot 2IrO_2$ | |
| | | [c]1185 | 19 | $Nd_2O_3$ + low $3Nd_2O_3 \cdot 2IrO_2$ | |
| | | 1202 | 20 | $Nd_2O_3$ + high $3Nd_2O_3 \cdot 2IrO_2$ | Possibly small amount of low 3:2 present. |
| | 70:30 | 1009 | 19 | Low $3Nd_2O_3 \cdot 2IrO_2$ + $Nd_2O_3$ | |
| | | [c]1185 | 60 | Low $3Nd_2O_3 \cdot 2IrO_2$ + $Nd_2O_3$ | |
| | | [c]1201 | 19 | Low $3Nd_2O_3 \cdot 2IrO_2$ + high $3Nd_2O_3 \cdot 2IrO_2$ + $Nd_2O_3$ | Nonequilibrium. |
| | | [c]1296 | 20 | High $3Nd_2O_3 \cdot 2IrO_2$ + $Nd_2O_3$ | Possibly small amount of low 3:2 present. |
| | | [c]1315 | 19 | $Nd_2O_3$ + high $3Nd_2O_3 \cdot 2IrO_2$ + Low $3Nd_2O_3 \cdot 2IrO_2$ | Nonequilibrium: low 3:2 probably formed on cooling; Ir not detected by x rays[d]; high 3:2 present only in minor amounts. |

TABLE 1. *Experimental data for compositions in the* $M_2O_3$–$IrO_2$ *and* $M_2O_3$–Ir *systems in air*—Continued

| System | Composition | Heat treatment | | X-ray diffraction analyses[b] | Remarks |
|---|---|---|---|---|---|
| | | temp.[a] | Time | | |
| $Nd_2O_3$–$IrO_2$ (cont.) | 62.5:37.5 | 1151 | 70 | Low $3Nd_2O_3 \cdot 2IrO_2 + Nd_2O_3$ | |
| | | 1180 | 21 | Low $3Nd_2O_3 \cdot 2IrO_2 + Nd_2O_3$ | |
| | | [c]1198 | 22 | Low $3Nd_2O_3 \cdot 2IrO_2$ + high $3Nd_2O_3 \cdot 2IrO_2$ + $Nd_2O_3$ | Nonequilibrium. |
| | 60:40 (3:2) | 1009 | 19 | Low $3Nd_2O_3 \cdot 2IrO_2$ | |
| | | 1175 | 20 | Low $3Nd_2O_3 \cdot 2IrO_2$ | |
| | | [c]1188 | 20 | Low $3Nd_2O_3 \cdot 2IrO_2$ | |
| | | [c]1200 | 60 | Low $3Nd_2O_3 \cdot 2IrO_2$ + high $3Nd_2O_3 \cdot 2IrO_2$ + $Nd_2O_3$ | Nonequilibrium.[e] |
| | | 1211 | 20 | High $3Nd_2O_3 \cdot 2IrO_2$ | Possibly some low 3:2 present. |
| | | [c]1243 | 20 | High $3Nd_2O_3 \cdot 2IrO_2$ | Possibly some low 3:2 present. |
| | | 1290 | 1.75 | High $3Nd_2O_3 \cdot 2IrO_2$ | Possibly some low 3:2 present. |
| | | 1313 | 1.75 | $Nd_2O_3$ + Ir | |
| | 50:50 | 1178 | 20 | Low $3Nd_2O_3 \cdot 2IrO_2 + Nd_2O_3 \cdot 2IrO_2$ | |
| | | [c]1195 | 22 | Low $3Nd_2O_3 \cdot 2IrO_2$ + high $3Nd_2O_3 \cdot 2IrO_2$ | Nonequilibrium; Ir not detected by x rays.[d] |
| | | 1247 | 16 | High $3Nd_2O_3 \cdot 2IrO_2$ + Ir | |
| | | 1289 | 3 | High $3Nd_2O_3 \cdot 2IrO_2$ + Ir | |
| | | [c]1305 | 1.75 | High $3Nd_2O_3 \cdot 2IrO_2 + Nd_2O_3$ + Ir | Nonequilibrium. |
| | | 1325 | 5 | $Nd_2O_3$ | Ir not detected by x rays.[d] |
| | 45:55 | 1000 | 19 | $Nd_2O_3 \cdot 2IrO_2$ + low $3Nd_2O_3 \cdot 2IrO_2$ | |
| | | 1188 | 20 | $Nd_2O_3 \cdot 2IrO_2$ + low $3Nd_2O_3 \cdot 2IrO_2$ | |
| | | [c]1210 | 68 | High $3Nd_2O_3 \cdot 2IrO_2$ | Ir not detected by x rays.[d] |
| | | 1249 | 20 | High $3Nd_2O_3 \cdot 2IrO_2$ | Ir not detected by x rays.[d] |
| | 40:60 | 1005 | 20 | $Nd_2O_3 \cdot 2IrO_2$ + low $3Nd_2O_3 \cdot 2IrO_2$ | |
| | 35:65 | 1005 | 20 | $Nd_2O_3 \cdot 2IrO_2$ + low $3Nd_2O_3 \cdot 2IrO_2$ | |
| | | 1151 | 19 | $Nd_2O_3 \cdot 2IrO_2$ + low $3Nd_2O_3 \cdot 2IrO_2$ | |
| | | [c]1173 | 22 | $Nd_2O_3 \cdot 2IrO_2$ + low $3Nd_2O_3 \cdot 2IrO_2$ | |
| | | 1187 | 17.5 | $Nd_2O_3 \cdot 2IrO_2$ + low $3Nd_2O_3 \cdot 2IrO_2$ | Possibly small amount of high 3:2 present. |
| | | [c]1198 | 17.5 | $Nd_2O_3 \cdot 2IrO_2$ + low $3Nd_2O_3 \cdot 2IrO_2$ + high $3Nd_2O_3 \cdot 2IrO_2$ | Nonequilibrium; Ir not detected by x rays.[d] |
| | | 1253 | 16 | High $3Nd_2O_3 \cdot 2IrO_2$ + Ir | |
| | | 1300 | 3 | High $3Nd_2O_3 \cdot 2IrO_2$ + Ir | |
| | | 1411 | 1 | Ir + $Nd_2O_3$ | Reheat of 1173 °C specimen. |
| | 33.3:66.7 (1:2) | 1005 | 19 | $Nd_2O_3 \cdot 2IrO_2$ | |
| | | 1180 | 90 | $Nd_2O_3 \cdot 2IrO_2$ + low $3Nd_2O_3 \cdot 2IrO_2$ | Nonequilibrium; small amount of $IrO_2$ probably lost by volatilization. |
| | | [c]1189 | 42 | $Nd_2O_3 \cdot 2IrO_2$ + low $3Nd_2O_3 \cdot 2IrO_2$ | Nonequilibrium; small amounts of $IrO_2$ probably lost by volatilization. |
| | | [c]1191 | 20 | $Nd_2O_3 \cdot 2IrO_2$ + Ir + low $3Nd_2O_3 \cdot 2IrO_2$ | Nonequilibrium. |
| | 30:70 | 1007 | 18 | $Nd_2O_3 \cdot 2IrO_2 + IrO_2$ | |
| | | 1295 | 19 | High $3Nd_2O_3 \cdot 2IrO_2$ + Ir | |
| | | [c]1308 | 19 | $Nd_2O_3$ + Ir + high $3Nd_2O_3 \cdot 2IrO_2$ | Nonequilibrium. |
| | 25:75 | 1005 | 19 | $Nd_2O_3 \cdot 2IrO_2 + IrO_2$ | |
| | | 1030 | 92 | $Nd_2O_3 \cdot 2IrO_2$ + Ir | |
| | | 1226 | 16 | Low $3Nd_2O_3 \cdot 2IrO_2$ [f]+ high $3Nd_2O_3 \cdot 2IrO_2$ + Ir | Nonequilibrium. |
| | | 1325 | 4.5 | Ir + $Nd_2O_3$ | |
| | 10:90 | 1027 | 5 | $Nd_2O_3 \cdot 2IrO_2$ + Ir + $IrO_2$ | Nonequilibrium. |
| | | 1150 | 16 | $Nd_2O_3 \cdot 2IrO_2$ + Ir + $IrO_2$ | Nonequilibrium. |
| | | 1181 | 67 | $Nd_2O_3 \cdot 2IrO_2$ + Ir | |
| | 0–100 | 0 | 0 | Amorphous to x rays | "As received" material. |
| | | 950 | 16 | $IrO_2$ | |
| | | 1010 | 64 | $IrO_2$ | |
| | | 1011 | 16 | $IrO_2$ | |
| | | [c]1017 | 16 | $IrO_2$ | |
| | | 1018 | 18 | $IrO_2$ | |
| | | 1022 | 16 | $IrO_2$ + Ir | Nonequilibrium. |
| | | 1026 | 3 | $IrO_2$ + Ir | Nonequilibrium. |
| | | 1047 | 12 | Ir | |
| | | 2000 | 0.5 | Ir | |
| $Sm_2O_3$–$IrO_2$ | 33.3:66.7 (1:2) | 1000 | 100 | $Sm_2O_3 \cdot 2IrO_2$ | |
| | | [f]1205 | 19 | $Sm_2O_3 \cdot 2IrO_2$ | |
| | | [f]1216 | 19 | $Sm_2O_3 \cdot 2IrO_2$ + unknown phase | Nonequilibrium; Ir not detected by x rays[d]; unknown phase similar to low $3Nd_2O_3 \cdot 2IrO_2$. |
| | | [f]1229 | 19 | $Sm_2O_3 \cdot 2IrO_2$ + Ir + unknown phase | Nonequilibrium; unknown phase similar to low $3Nd_2O_3 \cdot 2IrO_2$. |

TABLE 1. *Experimental data for compositions in the* $M_2O_3$–$IrO_2$ *and* $M_2O_3$–Ir *systems in air*—Continued

| System | Composition | Heat treatment | | X-ray diffraction analyses[b] | Remarks |
|---|---|---|---|---|---|
| | | temp.[a] | Time | | |
| $Eu_2O_3$–$IrO_2$ | 33.3:66.7 (1:2) | 1000 | 100 | $Eu_2O_3 \cdot 2IrO_2$ | |
| | | [f]1207 | 64 | $Eu_2O_3 \cdot 2IrO_2$ | |
| | | [f]1215 | 64 | $Eu_2O_3 \cdot 2IrO_2$ | |
| | | [f]1225 | 16 | $Eu_2O_3 \cdot 2IrO_2$ + unknown phase | Nonequilibrium; Ir not detected by x ray.[d] |
| | | [f]1231 | 16 | $Eu_2O_3 \cdot 2IrO_2$ + unknown phase | Nonequilibrium; Ir not detected by x ray.[d] |
| | | [f]1346 | 19 | $Eu_2O_3$ + Ir | |
| $Gd_2O_3$–$IrO_2$ | 33.3:66.7 (1:2) | 1000 | 100 | $Gd_2O_3 \cdot 2IrO_2$ + $Gd_2O_3$ | Nonequilibrium.[e] |
| | | [f]1218 | 19 | $Gd_2O_3 \cdot 2IrO_2$ + $Gd_2O_3$ | Nonequilibrium.[e] |
| | | [f]1235 | 19 | $Gd_2O_3 \cdot 2IrO_2$ + $Gd_2O_3$ | Nonequilibrium.[e] |
| | | [f]1242 | 19 | $Gd_2O_3 \cdot 2IrO_2$ + $Gd_2O_3$ + Ir | Nonequilibrium.[e] |
| $Dy_2O_3$–$IrO_2$ | 33.3:66.7 (1:2) | [f]1000 | 100 | $Dy_2O_3 \cdot 2IrO_2$ + $Dy_2O_3$ | Nonequilibrium.[e] |
| | | [f]1170 | 92 | $Dy_2O_3 \cdot 2IrO_2$ + $Dy_2O_3$ | Nonequilibrium.[e] |
| | | [f]1200 | 19 | $Dy_2O_3 \cdot 2IrO_2$ + $Dy_2O_3$ | Nonequilibrium.[e] |
| | | [f]1242 | 19 | $Dy_2O_3 \cdot 2IrO_2$ + $Dy_2O_3$ | Nonequilibrium.[e] |
| | | [c]1260 | 20 | $Dy_2O_3 \cdot 2IrO_2$ + $Dy_2O_3$ + unknown phase | Nonequilibrium.[e] |
| | | [c]1301 | 4 | $Dy_2O_3 \cdot 2IrO_2$ + $Dy_2O_3$ + unknown phase | Nonequilibrium.[e] |
| | | [f]1351 | 19 | $Dy_2O_3$ + Ir | |
| $Ho_2O_3$–$IrO_2$ | 33.3:66.7 (1:2) | 1000 | 100 | $Ho_2O_3 \cdot 2IrO_2$ + $Ho_2O_3$ + $IrO_2$ | Nonequilibrium. |
| | | [f]1218 | 19 | $Ho_2O_3 \cdot 2IrO_2$ + $Ho_2O_3$ | Nonequilibrium.[e] |
| | | [f]1235 | 19 | $Ho_2O_3 \cdot 2IrO_2$ + $Ho_2O_3$ + Ir | Nonequilibrium.[e] |
| $Y_2O_3$–$IrO_2$ | 33.3:66.7 (1:2) | 1000 | 100 | $Y_2O_3 \cdot 2IrO_2$ + $Y_2O_3$ | Nonequilibrium.[e] |
| | | [f]1210 | 19 | $Y_2O_3 \cdot 2IrO_2$ + $Y_2O_3$ | Nonequilibrium.[e] |
| | | [c]1216 | 4 | $Y_2O_3 \cdot 2IrO_2$ + $Y_2O_3$ | Nonequilibrium.[e] |
| | | 1225 | 19 | $Y_2O_3 \cdot 2IrO_2$ + $Y_2O_3$ + unknown phase | Nonequilibrium.[e] |
| | | 1351 | 19 | $Y_2O_3$ + Ir | |
| $Er_2O_3$–$IrO_2$ | 33.3:66.7 (1:2) | 1000 | 100 | $Er_2O_3 \cdot 2IrO_2$ + $Er_2O_3$ | Nonequilibrium.[e] |
| | | [f]1215 | 64 | $Er_2O_3 \cdot 2IrO_2$ + $Er_2O_3$ | Nonequilibrium.[e] |
| | | [c]1225 | 64 | $Er_2O_3 \cdot 2IrO_2$ + $Er_2O_3$ | Nonequilibrium[e]: 1:2 phase reduced in amount from that of previous heat treatment. Ir not detected by x rays.[d] |
| | | 1346 | 19 | $Er_2O_3$ + Ir | |
| $Tm_2O_3$–$IrO_2$ | 33.3:66.7 (1:2) | 1000 | 100 | $Tm_2O_3 \cdot 2IrO_2$ + $Tm_2O_3$ | Nonequilibrium.[e] |
| | | [f]1199 | 19 | $Tm_2O_3 \cdot 2IrO_2$ + $Tm_2O_3$ | Nonequilibrium.[e] |
| | | [c]1226 | 19 | $Tm_2O_3$ + $Tm_2O_3 \cdot 2IrO_2$ | Nonequilibrium[e]; 1:2 phase reduced in amount from that of previous heat treatment; Ir not detected by x rays.[d] |
| | | 1351 | 19 | $Tm_2O_3$ + Ir | |
| $Yb_2O_3$–$IrO_2$ | 33.3:66.7 (1:2) | 1000 | 100 | $Yb_2O_3 \cdot 2IrO_2$ + $Yb_2O_3$ | Nonequilibrium.[e] |
| | | [f]1161 | 19 | $Yb_2O_3 \cdot 2IrO_2$ + $Yb_2O_3$ | Nonequilibrium.[e] |
| | | [f]1173 | 19 | $Yb_2O_3 \cdot 2IrO_2$ + $Yb_2O_3$ | Nonequilibrium.[e] |
| | | [f]1199 | 19 | $Yb_2O_3$ + Ir + $Yb_2O_3 \cdot 2IrO_2$ | Nonequilibrium. |
| | | [f]1226 | 19 | $Yb_2O_3$ + Ir | |
| $Lu_2O_3$–$IrO_2$ | 33.3:66.7 (1:2) | 1000 | 100 | $Lu_2O_3 \cdot 2IrO_2$ + $Lu_2O_3$ | Nonequilibrium.[e] |
| | | [f]1161 | 19 | $Lu_2O_3 \cdot 2IrO_2$ + $Lu_2O_3$ | Nonequilibrium.[e] |
| | | [f]1170 | 19 | $Lu_2O_3 \cdot 2IrO_2$ + $Lu_2O_3$ | Nonequilibrium[e]: 1:2 phase reduced in amount from that of previous heat treatment; Ir not detected by x rays.[d] |
| | | [c]1200 | 19 | $Lu_2O_3$ + Ir + $Lu_2O_3 \cdot 2IrO_2$ | Nonequilibrium. |
| | | [f]1309 | 19 | $Lu_2O_3$ + Ir | |
| $In_2O_3$–$IrO_2$ | 33.3:66.7 (1:2) | 1000 | 100 | $In_2O_3$ + $IrO_2$ | |
| | | 1256 | 19 | $In_2O_3$ + Ir | |
| $Sc_2O_3$–$IrO_2$ | 33.3:66.7 (1:2) | 1000 | 100 | $Sc_2O_3$ + $IrO_2$ | |
| | | 1256 | 19 | $Sc_2O_3$ | Ir not detected by x rays.[d] |
| $Al_2O_3$–$IrO_2$ | 33.3:66.7 (1:2) | 1000 | 100 | $Al_2O_3$ + $IrO_2$ | |
| | | 1256 | 19 | $Al_2O_3$ + Ir | |
| $Nd_2O_3$–Ir | 33.3:66.7 (1:2) | 1000 | 12 | $Nd_2O_3 \cdot 2IrO_2$ + Ir + $IrO_2$ | Nonequilibrium. |
| | | [c]1400 | 1 | Ir + $Nd_2O_3$ + $Nd(OH)_3$ | $Nd_2O_3$ commonly hydrates at room temperature. |
| | | [c]2020 | .75 | Ir + $Nd_2O_3$ + $Nd(OH)_3$ | $Nd_2O_3$ commonly hydrates at room temperature. |



766-033 O - 65 - 3

TABLE 1. *Experimental data for compositions in the* $M_2O_3$–$IrO_2$ *and* $M_2O_3$–Ir *systems in air*—Continued

| System | Composition | Heat treatment | | X-ray diffraction analyses[b] | Remarks |
|---|---|---|---|---|---|
| | | temp.[a] | Time | | |
| $Nd_2O_3$–Ir (cont.) | 0:100 | 0 | 0 | Ir | "As received." |
| | | 1000 | 6 | $IrO_2$ + Ir | Nonequilibrium. |
| | | [c]1000 | 20 | $IrO_2$ + Ir | Nonequilibrium; greater amount of $IrO_2$ present from that of previous heat treatment. |
| | | [c]1000 | 116 | $IrO_2$ + Ir | Nonequilibrium. |
| | | [c]1040 | 18 | Ir + $IrO_2$ | Nonequilibrium; smaller amount of $IrO_2$ present from that of previous heat treatment. |
| | | [c]1250 | 5 | Ir + $IrO_2$ | Nonequilibrium; only small amount of $IrO_2$ present. $IrO_2$ probably formed on cooling. |
| $Sm_2O_3$–Ir | 33.3:66.7 (1:2) | 1000 | 12 | $Sm_2O_3 \cdot 2IrO_2$ + $IrO_2$ + Ir + unknown phase | Nonequilibrium; unknown phase similar to low $3Nd_2O_3 \cdot 2IrO_2$. |
| | | [c]1400 | 1 | $Sm_2O_3$ + Ir | |
| | | [c]2030 | 0.50 | $Sm_2O_3$ + Ir | |
| $Eu_2O_3$–Ir | 33.3:66.7 (1:2) | 1000 | 12 | $Eu_2O_3 \cdot 2IrO_2$ | |
| | | [c]1400 | 1 | $Eu_2O_3$ + Ir | |
| | | [c]2020 | 0.50 | $Eu_2O_3$ + Ir | |
| $Gd_2O_3$–Ir | 33.3:66.7 (1:2) | 1000 | 12 | $Gd_2O_3 \cdot 2IrO_2$ + $Gd_2O_3$ + $IrO_2$ + Ir | Nonequilibrium. |
| | | [c]1400 | 1 | $Gd_2O_3$ + Ir | |
| | | [c]2015 | 0.50 | $Gd_2O_3$ + Ir | |
| $Dy_2O_3$–Ir | 33.3:66.7 (1:2) | 1000 | 12 | $Dy_2O_3 \cdot 2IrO_2$ + $Dy_2O_3$ + $IrO_2$ + Ir | Nonequilibrium. |
| | | [c]1400 | 1 | $Dy_2O_3$ + Ir | |
| | | [c]2015 | 0.50 | $Dy_2O_3$ + Ir | |
| $Y_2O_3$–Ir | 33.3:66.7 (1:2) | 1000 | 12 | $Y_2O_3 \cdot 2IrO_2$ + $Y_2O_3$ + $IrO_2$ + Ir | Nonequilibrium. |
| | | [c]1400 | 1 | $Y_2O_3$ + Ir | |
| | | 2010 | 0.50 | $Y_2O_3$ + Ir | |
| $Lu_2O_3$–Ir | 33.3:66.7 (1:2) | 1000 | 12 | $Lu_2O_3 \cdot 2IrO_2$ + $Lu_2O_3$ + $IrO_2$ + Ir | Nonequilibrium. |
| | | [c]1400 | 1 | $Lu_2O_3$ + Ir | |
| | | [c]2080 | 0.50 | $Lu_2O_3$ + Ir | |
| $Al_2O_3$–Ir | 33.3:66.7 (1:2) | 1000 | 12 | $Al_2O_3$ + Ir + $IrO_2$ | Nonequilibrium. |
| | | [c]1400 | 1 | $Al_2O_3$ + Ir | |
| | | 2010 | 0.5 | $Al_2O_3$ + Ir + $IrO_2$ | Nonequilibrium: $IrO_2$ probably formed on cooling. |
| | | 2055 | 0.5 | $Al_2O_3$ + Ir | Specimen partially melted. |

[a] All specimens in the $Nd_2O_3$–$IrO_2$ system heat treated at 800 °C a minimum of 24 hrs prior to the listed heat treatment.

[b] The phases identified are given in order of the relative amount present at room temperature.

[c] Reheat of the previous specimen.

[d] Iridium dioxide ($IrO_2$) in combination with other oxides, upon dissociation, forms small Ir metal grains which are generally detectable by microscopic examination. X-ray patterns of these specimens often fail to show reflections representing Ir unless there is anomalous intensity due to orientation of the grains.

[e] Small amount of $IrO_2$ probably lost by volatilization.

[f] Reheat of 1000 °C specimen.

As $IrO_2$ is heated to temperatures near its dissociation temperature, it becomes somewhat volatile. Cordfunke and Meyer [5] conclude that $IrO_2$ combines with oxygen to form $IrO_3$ which is stable only in the gaseous state. Efforts to produce solid $IrO_3$ in the present work proved unsuccessful. The condensed vapors from heated samples of either $IrO_2$ or Ir always were identified as $IrO_2$. The problem of the volatility of $IrO_2$ in the present study was minimized greatly by reacting the end members at low temperatures. The volatilization of $IrO_2$ was sufficiently inhibited by reaction to consider the listed compositions (cation to metal ratio) of table 1 as being near correct.

Two intermediate binary compounds occur in the $Nd_2O_3$–$IrO_2$ system. One phase, a 1:2 compound, is stable up to 1190 °C where it dissociates to two solid phases and a vapor phase, presumably oxygen. The composition of the 1:2 compound corresponds to that of an $A_2B_2O_7$ pyrochlore type phase. Table 2 gives the x-ray pattern of $Nd_2O_3 \cdot 2IrO_2$ indexed on the basis of the typical face-centered cubic symmetry ($a = 10.383$Å) of the pyrochlore structure.

TABLE 2. *X-ray diffraction powder data for* $Nd_2O_3 \cdot 2IrO_2$ ($CuK_\alpha$ *radiation*) [a]

| *hkl* [b] | *d* [c] | $I/I_0$ [d] |
|---|---|---|
| 111 | 6.00 | 6 |
| 311 | 3.140 | 4 |
| 222 | 3.003 | 100 |
| 400 | 2.673 | 43 |
| 511/333 | 2.0035 | 3 |
| 440 | 1.8370 | 46 |
| 622 | 1.5661 | 40 |
| 444 | 1.4994 | 11 |
| 800 | 1.2986 | 6 |
| 622 | 1.1913 | 11 |
| 840 | 1.1613 | 10 |
| 844 | 1.0601 | 9 |
| 10,22/666 | 0.9995 | 9 |
| 880 | .9174 | 3 |
| 11,33/973 | .8813 | 3 |
| 10,62 | .8772 | 9 |
| 12,00/884 | .8652 | 9 |
| 12,40 | .8205 | 3 |

[a] X-ray pattern obtained from specimen heat treated at 1005 °C for 19 hrs in air.
[b] The Miller indices are those representing a fcc unit cell with $a = 10.383$ Å.
[c] Interplanar spacing.
[d] Relative Intensity.

The other binary phase was found to occur in the system at the 3:2 composition. This compound, $3Nd_2O_3 \cdot 2IrO_2$, similar in behavior to the 1:2 phase, also dissociates to two solid phases (and vapor) at 1300 °C. At 1195 °C, the 3:2 compound appears to undergo a polymorphic transformation. The unindexed x-ray powder patterns of both the high and low forms are given in table 3. Because the transformation temperature of the 3:2 compound and the dissociation temperature of the 1:2 phase are approximately the same, it appears likely that an oxygen loss may have produced the apparent polymorphic phase change. Therefore, the phase designated high 3:2 in figure 1, may be, in reality, an oxygen deficient phase, $3Nd_2O_3 \cdot 2IrO_x$, where $x$ is less than 2.

At temperatures above 1300 °C the system under consideration no longer can be represented by the pseudo system, $Nd_2O_3$–$IrO_2$. Through dissociation, the system had changed to the $Nd_2O_3$–Ir binary. Up to temperatures of 2000 °C, $Nd_2O_3$ and Ir do not react in the solid state. Presumably no solid state reaction would occur below melting. No definite conclusions can be made concerning the melting characteristics of the system until further experimental work has been performed.

It should be noted that figure 1 pertains only to the phase relations of the system in an air environment at atmospheric pressure. Any change in oxygen pressure would greatly change the diagram. To emphasize this, limited experiments were carried out utilizing sealed Pt tubes as containers. In every instance the pressure in the tube was sufficient to raise the temperatures of dissociation of mixtures of the compounds with $IrO_2$ 20 to 150 °C. For unexplained reasons pure $IrO_2$ could not be heated to temperatures in excess of 1000 °C without tube failure due to the high internal pressure.

TABLE 3. *X-ray diffraction powder data for the "high" and "low" forms of* $3Nd_2O_3 \cdot 2IrO_2$ ($CuK_\alpha$ *radiation*) [a]

| "Low" $3Nd_2O_3 \cdot 2IrO_2$ [b] | | "High" $3Nd_2O_3 \cdot 2IrO_2$ [c] | |
|---|---|---|---|
| *d* [d] | $I/I_0$ [e] | *d* [d] | $I/I_0$ [e] |
| 3.34 | 11 | 4.65 | 7 |
| 3.20 | 100 | 4.06 | 32 |
| 3.00 | 11 | 4.02 | 11 |
| 2.85 | 16 | 3.70 | 4 |
| 2.73 | 18 | 3.28 | 8 |
| 2.64 | 34 | 3.12 | 7 |
| 2.379 | 5 | 3.09 | 28 |
| 2.199 | 5 | 2.85 | 100 |
| 2.110 | 6 | 2.84 | 56 |
| 2.076 | 5 | 2.72 | 4 |
| 2.050 | 4 | 2.57 | 4 |
| 2.013 | 5 | 2.494 | 7 |
| 1.940 | 5 | 2.443 | 13 |
| 1.897 | 36 | 2.424 | 13 |
| 1.875 | 11 | 2.418 | 8 |
| 1.840 | 4 | 2.110 | 7 |
| 1.808 | 3 | 2.091 | 18 |
| 1.763 | 5 | 2.030 | 13 |
| 1.725 | 6 | 2.005 | 28 |
| 1.633 | 13 | | |
| 1.601 | 18 | | |
| 1.596 | 16 | | |
| 1.545 | 10 | | |

[a] The x-ray patterns of these specimens show only broad and generally weak peaks. Therefore, only the more intense, readily measurable reflections are reported.
[b] X-ray pattern obtained from specimen heat treated at 1009 °C for 19 hrs in air.
[c] X-ray pattern obtained from specimen heat treated at 1243 °C for 20 hrs in air. The high form may be oxygen deficient with the formula corresponding to the type $3Nd_2O_3 \cdot 2IrO_x$ where $x$ is less than two.
[d] Interplanar Spacing.
[e] Relative Intensity.

### 4.2. Other $M_2O_3$–$IrO_2$ Systems in Air

Montmony and Bertaut [15] have previously reported the existence of pyrochlore type compounds in mixtures of rare earth sesquioxides and $IrO_2$. In order to confirm the earlier work and to investigate these compounds more fully, $M_2O_3$:$2IrO_2$ mole ratio mixtures were prepared from $IrO_2$ and either $Sm_2O_3$, $Eu_2O_3$, $Gd_2O_3$, $Dy_2O_3$, $Ho_2O_3$, $Y_2O_3$, $Er_2O_3$, $Tm_2O_3$, $Yb_2O_3$, $Lu_2O_3$, $In_2O_3$, $Sc_2O_3$, and $Al_2O_3$.

Tables 1 and 4 summarize the results obtained for this set of experiments. All 1:2 mixtures containing the rare earth oxides and $Y_2O_3$ formed face-centered cubic pyrochlore type compounds. Unfortunately, some of the compositions contained, in addition to the pyrochlore type phase, small amounts of the pure rare earth oxide. In all probability an unknown quantity of $IrO_2$ was lost by volatilization before complete combination occurred. The possibility still remains, however, that the true composition of the pyrochlore phase does not correspond to the idealized $Ln_2Ir_2O_7$ formula. Evidence for "off composition" pyrochlore compounds have been reported elsewhere [16].

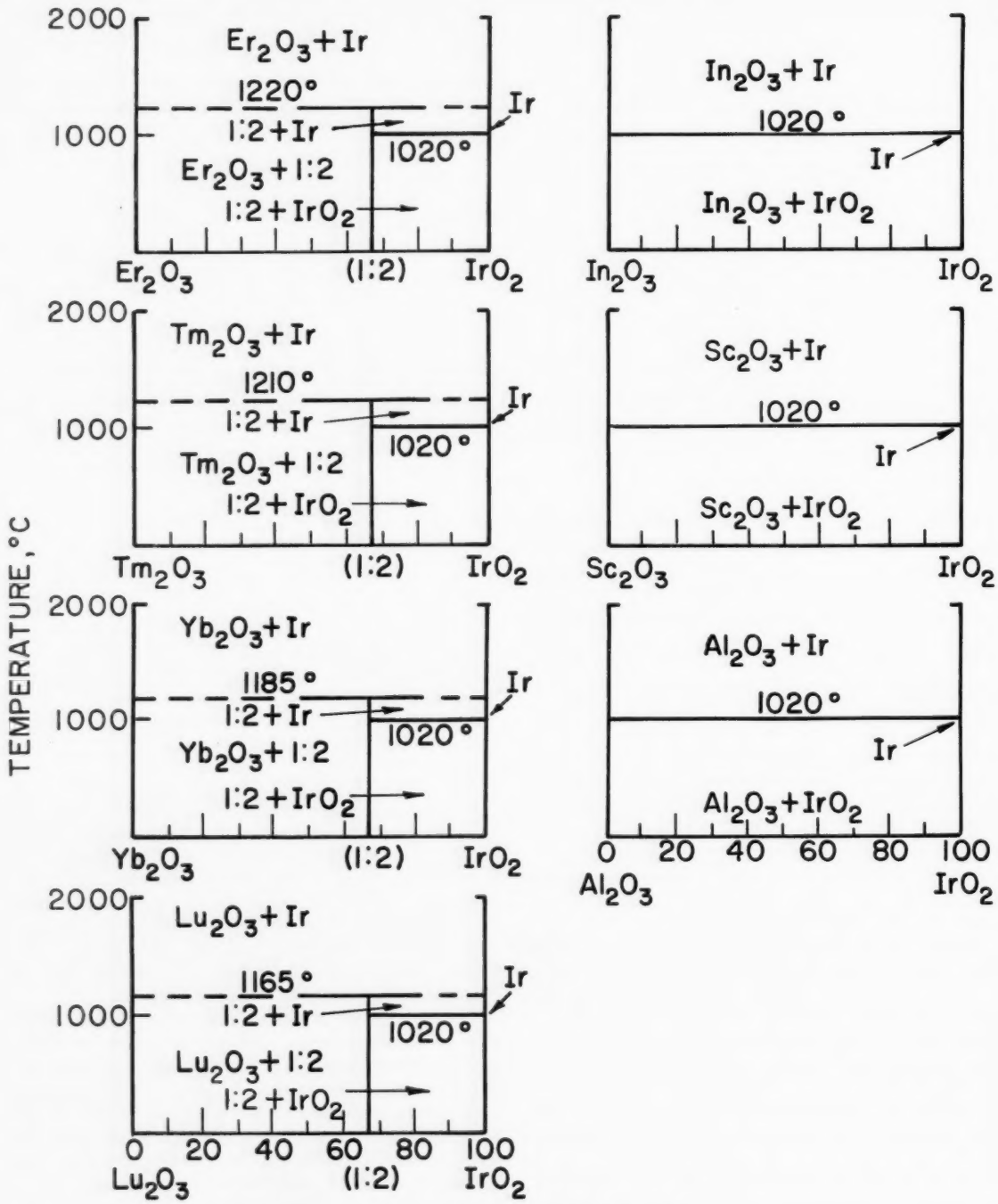


FIGURE 2. *Predicted composite phase equilibrium diagrams for various* $M_2O_3$–$IrO_2$ *and* $M_2O_3$–Ir *systems in air.*

For clarity experimental points are not included. See table 1 for exact compositions and temperatures studied. All experiments conducted involved only the $M_2O_3$:$2IrO_2$ compositions in an air environment. Ir–Iridium metal, 1:2–$M_2O_3 \cdot 2IrO_2$.

As expected, the unit cell dimensions of the cubic pyrochlore compounds decrease in a linear manner as the size of the rare earth cation decreases. In a manner similar to $Nd_2Ir_2O_7$, all the compounds dissociated at temperatures above 1020 °C, the decomposition temperature of $IrO_2$. The dissociation temperatures (table 4) when plotted as a function of the radius of the rare earth cation do not change linearly as do the unit cell dimensions. As the size of the cation is decreased, the dissociation temperature at first increases, approaching a maximum for $Dy_2Ir_2O_7$ and then decreases to a minimum for $Lu_2Ir_2O_7$.

Under the conditions of the experiments $In_2O_3$, $Sc_2O_3$, and $Al_2O_3$ did not react even partially with $IrO_2$. X-ray patterns of these mixtures after heat treatment at 1000 °C show only reflections representing $IrO_2$ and the admixture oxide. Additional heat treatment at 1256 °C failed to cause combination and only succeeded in dissociating the $IrO_2$. The resultant mixture contained the refractory oxide and Ir metal.

It is evident that the $Nd_2O_3$–$IrO_2$ system is representative in a general way of the other $M_2O_3$–$IrO_2$ systems. Using it as a guide, figure 2 gives a number of the subsolidus phase diagrams for various systems as predicted from the data tabulated in table 1.

The $In_2O_3$–$IrO_2$, $Sc_2O_3$–$IrO_2$, and $Al_2O_3$–$IrO_2$ systems are rather simple and straightforward inasmuch as there is no detectable reaction between end members in the solid state. These diagrams indicate only the dissociation of $IrO_2$, the point at which the system reverts to the true $M_2O_3$–Ir system.

The diagrams for the $Er_2O_3$–$IrO_2$, $Tm_2O_3$–$IrO_2$, $Yb_2O_3$–$IrO_2$, and $Lu_2O_3$–$IrO_2$ systems in air are slightly more complicated, each indicating the occurrence of a 1:2 compound. Studies of 1:2 compounds show that they dissociate to the solid phases $M_2O_3$ and Ir. If other phases occurred in the systems, they necessarily would have to dissociate at lower temperatures than the 1:2 compound. If other compounds existed which were stable at temperatures greater than the 1:2 dissociation temperatures, they would appear as a decomposition product of the pyrochlore type phase. As stated previously, this was not the case. On the basis of the more complete $Nd_2O_3$–$IrO_2$ study, the existence of phases other than the 1:2 is not considered likely for these systems.

Additional experimentation is needed before the $Sm_2O_3$–$IrO_2$, $Eu_2O_3$–$IrO_2$, $Gd_2O_3$–$IrO_2$, $Dy_2O_3$–$IrO_2$, $Ho_2O_3$–$IrO_2$, and $Y_2O_3$–$IrO_2$ systems can be drawn. Each of the 1:2 compounds occurring in these systems dissociates to a mixture of solid phases, generally consisting of Ir and an unidentified phase.

### 4.3. $M_2O_3$–Ir Reactions

In order to establish whether or not the results found for the $M_2O_3$–$IrO_2$ studies were indicative of Ir in combination with various oxides, a limited number of experiments were performed involving oxide-Ir mixtures. Table 1 gives the data obtained for 1:2 mole ratio (oxide:metal) mixtures heat treated in an air environment. It is apparent that Ir oxidizes at least partially to $IrO_2$, which, in turn reacts with the admixture oxide to form the same pyrochlore type compounds listed in table 4. At higher temperatures the pyrochlore type compounds dissociated as expected and further reaction between end members did not take place.

TABLE 4. $Ln_2O_3 \cdot 2IrO_2$ *pyrochlore-type compounds*

| Compound | Radius of $Ln^{+3}$ [a] | Dissociation temperature [b] | X-ray data | |
|---|---|---|---|---|
| | | | Symmetry | Unit cell dimension |
| | Å | °C | | Å |
| $Nd_2O_3 \cdot 2IrO_2$ | 1.04 | 1190 | cubic | 10.383 |
| $Sm_2O_3 \cdot 2IrO_2$ | 1.00 | 1210 | cubic | 10.313 |
| $Eu_2O_3 \cdot 2IrO_2$ | 0.98 | 1220 | cubic | 10.293 |
| $Gd_2O_3 \cdot 2IrO_2$ | .97 | 1240 | cubic | 10.265 |
| $Dy_2O_3 \cdot 2IrO_2$ | .92 | 1250 | cubic | 10.207 |
| $Ho_2O_3 \cdot 2IrO_2$ | .91 | 1225 | cubic | 10.180 |
| $Y_2O_3 \cdot 2IrO_2$ | ≈.91 | 1220 | cubic | 10.177 |
| $Er_2O_3 \cdot 2IrO_2$ | .89 | 1220 | cubic | 10.163 |
| $Tm_2O_3 \cdot 2IrO_2$ | .87 | 1210 | cubic | 10.134 |
| $Yb_2O_3 \cdot 2IrO_2$ | .86 | 1185 | cubic | 10.115 |
| $Lu_2O_3 \cdot 2IrO_2$ | .85 | 1165 | cubic | 10.096 |

[a] All radii of the rare earth cations taken from Arhens [17] with the exception of $Y^{+3}$ which was estimated by Roth and Schneider [4].

[b] Dissociation temperatures are applicable only to those specimens heated in air.

Unfortunately, Ir either alone or in combination with an oxide, never completely oxidized to $IrO_2$. As indicated by microscopic examination, $IrO_2$, as it forms, appears to coat the Ir grains and thus tends to inhibit additional oxidation. At temperatures just below the $IrO_2$ dissociation temperature, $IrO_2$ is somewhat volatile. As the metal forms $IrO_2$, the oxide is lost by vaporization and a steady state is reached where the metal:oxide (Ir:$IrO_2$) ratio of the remaining material appears to remain approximately constant. In essence, true equilibrium at low temperatures could not be obtained in the $M_2O_3$:2Ir mixtures because of the inherent difficulty in achieving complete oxidation of Ir. Except for the presence of Ir at low temperatures, the data for the $M_2O_3$:2Ir compositions completely substantiated the $M_2O_3$–$IrO_2$ studies. Also, these data, in effect, establish the reversibility of the various transformations (dissociation) discussed earlier.

In all the aforementioned experiments, every effort was made through thorough mixing and prolonged heat treatment to react Ir with the various oxides. Even with these precautions, Ir while in the metallic state appears to be unreactive with the oxides studied and thus seems quite acceptable as a container material for high temperature application in an air environment.

The fact that Ir oxidizes at low temperatures does not appreciably detract from its use as a container since all phases containing $IrO_2$ subsequently dissociate.

### 4.4. Summary

Selected mixtures in systems involving Ir or $IrO_2$ and various sesquioxides were studied by x-ray diffraction techniques after heat treatment in an air environment. Iridium, in air, oxidizes almost completely to $IrO_2$ at low temperatures. The dissociation temperature of $IrO_2$ in air at atmospheric pressure was established at 1020 ±5 °C. Iridium in combination with the sesquioxides also forms $IrO_2$ which in turn reacts with a number of the oxides to form binary compounds. The pseudo binary system $Nd_2O_3$–$IrO_2$ exemplified the typical type of reaction and was studied in detail. Two phases, a compound believed to be $3Nd_2O_3 \cdot 2IrO_2$ having unknown symmetry and a cubic pyrochlore type compound $Nd_2O_3 \cdot 2IrO_2$, with $a = 10.383$ Å, occur in the system. The 3:2 and 1:2 compounds dissociate at 1300 and 1190 °C respectively. Above 1300 °C the system corresponds to the $Nd_2O_3$–Ir join in the Nd–Ir–O ternary system. No further reaction appears to take place between $Nd_2O_3$ and Ir up to 2000 °C.

Pyrochlore type compounds also were found to occur at the 1:2 mixture of either $Sm_2O_3$, $Eu_2O_3$, $Gd_2O_3$, $Ho_2O_3$, $Y_2O_3$, $Dy_2O_3$, $Er_2O_3$, $Tm_2O_3$, $Yb_2O_3$, or $Lu_2O_3$ with $IrO_2$. Each of these compounds also dissociated upon heating at temperatures above the dissociation temperature of $IrO_2$. Mixtures of either $In_2O_3$, $Sc_2O_3$, or $Al_2O_3$ with $IrO_2$ did not react at temperatures up to 2000 °C. The phase diagrams for a number of the $M_2O_3$–$IrO_2$ systems have been predicted.

## 5. References

[1] S. J. Schneider, Mono. 68, NBS, 31 p. (1963).
[2] H. E. Swanson, R. K. Fuyat and G. M. Ugrinic, NBS Cir. 539, **4,** 9–10 (1963).
[3] H. F. Stimson, J. Res. NBS **65A** (Phys. and Chem.) No. 3, 139–145 (1960).
[4] H. E. Swanson, M. C. Morris and E. H. Evans, NBS Mono. 25, Sec. 4 (1965) to be published.
[5] E. H. P. Cordfunke and G. Meyer, Rec. Trav. Chim. **81,** 495–504 (1962).
[6] R. S. Roth and S. J. Schneider, J. Res. NBS **64A** (Phys. and Chem.) No. 4, 309–318 (1960).
[7] M. W. Shafer and R. Roy, J. Am. Ceram. Soc. **42,** 563–570 (1959).
[8] H. E. Swanson, R. K. Fuyat and G. M. Ugrinic, NBS Cir. 539, **4,** 26 (1963).
[9] W. A. Lambertson and F. H. Gunzel, Jr., A.N.L. U.S. AEC Publ. AECD–3465, 1–4 (1952).
[10] S. J. Schneider and R. S. Roth, J. Res. NBS **65A** (Phys. and Chem.) No. 4, 317–332 (1960).
[11] S. J. Schneider, J. Res. NBS **65A** (Phys. and Chem.) No. 5, 429–434 (1961).
[12] S. J. Schneider and J. L. Waring, J. Res. NBS **67A** (Phys. and Chem.) No. 1, 19–25 (1963).
[13] A. Muan, Am. J. Sci. **256** 171–207 (1958).
[14] A. Muan and C. L. Gee, J. Am. Ceram. Soc. **39** (6) 207–214 (1956).
[15] M. Montmony and F. Bertaut, Compt. Rend. **252** 4171 – 4173 (1961).
[16] R. S. Roth, J. Res. NBS **62A** (Phys. and Chem.) No. 1, 27–38 (1959).
[17] L. H. Ahrens, Geochim. et Cosmochim. Acta **2** 155–169 (1952).

(Paper 69A3–343)

JOURNAL OF RESEARCH of the National Bureau of Standards—A. Physics and Chemistry
Vol. 69A, No. 3, May–June 1965

# Phase Equilibrium Relationships in the System $Gd_2O_3$–$TiO_2$

J. L. Waring and S. J. Schneider

(February 19, 1965)

The phase equilibrium relationships for a major portion of the $Gd_2O_3$–$TiO_2$ system were determined in air, from a study of solid state reactions and from fusion characteristics. Three intermediate phases, a 1:2 compound, a 1:1 compound, and a face-centered cubic solid solution occur in the system. The solid solution phase is indicated on the phase diagram as existing from 33 to 40 mole percent $TiO_2$, at 1750 °C. This phase melts incongruently over a range of temperatures and compositions, from 1840 °C, the peritectic temperature at 35 mole percent $TiO_2$, to 1775 °C at 40 mole percent $TiO_2$, the incongruent melting temperature of $Gd_2O_3 \cdot TiO_2$. The minimum temperature of stability for the phase is 1600 °C at 38 mole percent $TiO_2$. The compound $Gd_2O_3 \cdot 2TiO_2$ has a cubic pyrochlore structure type with $a = 10.181$ Å and melts congruently at 1820 °C. This phase apparently accepts up to about 3 mole percent $TiO_2$ in solid solution at 1460 °C. The compound $Gd_2O_3 \cdot TiO_2$, melts incongruently at 1775 °C and has a reversible phase transition at 1712 °C. The x-ray powder diffraction pattern of the high temperature modification was indexed on the basis of a hexagonal cell $a = 3.683$ Å, $c = 11.995$ Å and is apparently related to the A-type rare earth oxide. The compositions $Sm_2O_3$:$TiO_2$ and $Eu_2O_3$:$TiO_2$ gave x-ray diffraction powder patterns with marked similarity one to the other as well as to both the high and low polymorphs of $Gd_2O_3 \cdot TiO_2$. The composition $Dy_2O_3$:$TiO_2$ formed several phases one of which is apparently related to the high temperature polymorph of $Gd_2O_3 \cdot TiO_2$.

## 1. Introduction

The increased availability of more pure rare earth oxides together with a continuing search for new rare earth refractory materials with desirable optical, electrical, and magnetic properties has served as an impetus to investigate the phase equilibrium relationships in rare earth oxide systems. The authors [1][1] outlined, in part, the subsolidus relationships of the binary combinations of the rare earth sesquioxides with selected oxides of the trivalent cations.

It was decided to extend this rare earth sesquioxide study to incorporate the oxides of the tetravalent cations. For this reason, the system $Gd_2O_3$–$TiO_2$ was selected to be studied in detail in air since it is probably representative of other B-type rare earth oxide–$TiO_2$ systems. The only detailed $Ln_2O_3$–$TiO_2$ phase study[2] reported previously in the literature was that of the system $La_2O_3$–$TiO_2$ by MacChesney and Sauer [2]. Roth [3] and Brixner [4] reported the existence of a number of rare earth titanates of the general type $Ln_2Ti_2O_7$ having the pyrochlore type structure, i.e., $Gd_2Ti_2O_7$ ($a = 10.181$ Å). Queyroux [5] reported a tentative phase diagram for the system $Gd_2O_3$–$TiO_2$ in which three phases were postulated: a solid solution phase occurring at approximately 40 mole percent $TiO_2$, a 1:2 compound with limited solid solution, and a 1:1 compound.

Three polymorphs of $Gd_2O_3$ have been reported. They are the A (hexagonal), B (monoclinic) and C (cubic) type rare earth oxides. The A type was reported [6] to occur metastably. Several workers [7, 8] have reported that the C to B phase transition in $Gd_2O_3$ is reversible. Roth and Schneider [6] concluded that $Gd_2O_3$ crystallizes in the C form at low temperatures and transforms irreversibly to the B type at 1225 °C. In this study the B type was considered to be the only stable modification. The unit cell dimensions of B-type $Gd_2O_3$ were reported by Roth and Schneider [6] as $a = 14.06$ Å, $b = 3.572$ Å, $c = 8.75$ Å, and $\beta = 100.10°$. Those of $TiO_2$ (rutile) were given by Swanson and Tatge [9] as $a = 4.594$ Å, $c = 2.958$ Å.

## 2. Materials

The starting materials used in this study were found by general quantitative spectrochemical analyses[3] to have the following impurities: $Gd_2O_3$–Ca present in amounts less than 0.01 percent, Fe, Mg, Pb, and Si each present in amounts less than 0.001 percent,

[1] Figures in brackets indicate the literature references at the end of the paper.

[2] The symbol "Ln" represents the lanthanide series, lanthanum through lutecum.

[3] The spectrochemical analyses were performed by the Spectrochemical Section of the National Bureau of Standards. The rare earth oxides used to synthesize the related phases were better than 99.7 percent pure.

and B, Cu, and Mn each present in amounts less than 0.0001 percent. $TiO_2$–Si present in amounts less than .1 percent, Mg present in amounts less than 0.01 percent, Cu present in less than 0.001 percent, and Ca present in amounts less than 0.0001 percent.

## 3. Specimen Preparation and Test Methods

Two gram batches of various combinations of $Gd_2O_3$ and $TiO_2$ were weighed, mixed in a mechanical shaker for approximately 10 min and pressed into disks at about $10^4$ psi. The disks were placed on platinum setters and calcined in air at 1000 °C for 18 hrs. To achieve physical homogeneity the specimens were ground in an agate mortar, repressed and recalcined for an additional 4 hrs at 1000 °C. Following these preliminary heat treatments portions of the ground specimen were placed in platinum alloy tubes and heated in the quenching furnace to various temperatures for different periods of time.

The tubes containing the specimens were quenched into ice water and examined by x-ray diffraction techniques. A high-angle recording Geiger counter diffractometer and Ni-filtered Cu radiation was used in the study. The Geiger counter traversed the specimen at 1/4 deg/min and radiation was recorded on the chart at 1 deg-2$\theta$/in. The unit cell dimensions reported can be considered accurate to about $\pm 2$ in the last decimal place listed. Equilibrium was considered to have been achieved when x-ray patterns showed no change after successive heat treatments of a specimen or when the data were consistent with the results from a previous set of experiments. Solidus and liquidus temperatures were obtained by using both a quenching furnace and an induction furnace. Because of the temperature limitation of the quenching furnace melting points above 1800 °C were determined with the induction furnace. Some duplicate determinations below 1800 °C were made using both furnace types.

The essential features of the furnaces were described previously by the authors [11]. In essence, the quenching furnace consisted of two concentric ceramic tubes wound with platinum-rhodium alloy wire. The inner tube served as the primary winding and the outer one as the booster. Separate power sources were used with each winding.

The power for the outer winding (booster) was supplied from a variable auto transformer. An a-c bridge type controller [12] in which the furnace winding was one arm of the bridge was used to control the temperature of the inner winding. The furnace temperature was controlled to about $\pm 3$ °C. Temperature was measured with a 95 percent Pt–5 percent Rh versus 80 percent Pt–20 percent Rh thermocouple used in conjunction with a high precision potentiometer.

The induction furnace consisted of an iridium crucible and cover which acted as the susceptor and specimen container. A small fragment of the calcined material was placed in the iridium crucible on an iridium setter or button and heated to the desired temperature for about 2 min to achieve thermal equilibrium. Apparent temperatures were measured with a calibrated, disappearing filament-type optical pyrometer which was sighted through a 45 deg calibrated prism into the viewing hole at the center of the crucible cover. The temperature measuring system of both the quenching furnace and the induction furnace were calibrated frequently against the melting point of Au (1063 °C), Pd (1552 °C), and Pt (1769 °C)[4]. In addition, the measuring system of the induction furnace was also calibrated against the melting point of Rh (1960 °C). Temperatures reported in the present study were considered accurate to within $\pm 10$ °C below 1650 °C and to within $\pm 20$ °C above. The measurements were reproducible to within $\pm 5$ °C, or better. The degree of melting was determined by the physical appearance of quenched or rapidly cooled specimens. The first adherence of the specimen to the platinum container or iridium setter generally established the beginning of melting. In quenched specimens, complete melting was established by the formation of a meniscus. Similarly the slumping or loss of shape of the inductively heated specimens established complete melting.

## 4. Results and Discussion

The equilibrium phase diagram (fig. 1) for a major portion of the $Gd_2O_3$-$TiO_2$ system has been constructed from the data listed in tables 1 and 2. Solid circles represent composition and temperatures of experiments conducted in the quenching furnace and solid triangles represent those conducted in the induction furnace. A combination of a solid triangle bound by an open circle represents those conducted in both types of furnaces at the same temperature. Two melting points of $Gd_2O_3$ 2330 °C and 2350 °C [13, 14] have been reported. Because of the temperature limitations of the present equipment the value was not redetermined. The numerous reported melting points of $TiO_2$ have been tabulated by Schneider [15]. Because of the apparent problems inherent with the determination of the melting point of $TiO_2$, a redetermination was not made at this time.

The following intermediate phases, indicated in figure 1, were found to occur in the system: a solid solution ($FCC_{ss}$), existing at about 1750 °C, from approximately 33 to 40 mole percent $TiO_2$; a compound, $Gd_2O_3 \cdot TiO_2$, and a compound $Gd_2O_3 \cdot 2TiO_2$. These data generally confirm those reported by Queyroux [5].

The solid solution phase ($FCC_{ss}$) has a maximum incongruent melting point at 1840 °C at 35 mole percent $TiO_2$. A minimum dissociation temperature was found to occur at 1600 °C at 38 mole percent $TiO_2$ as compared to the 1550 °C [5] value reported previously. The existence of a minimum decomposition temperature was evident since the solid solution phase once

[4] The purity of the metals used for calibration purposes was better than 99.9 percent. See reference [10].

formed could be decomposed by reheating to 1548 °C for 4 hrs. From x-ray powder diffraction data, the solid solution phase was shown to be face-centered cubic with a maximum unit cell dimension of 5.32 Å and a minimum of 5.28 Å at 1750 °C. Since the x-ray patterns were of rather poor quality with characteristic high background, the polarizing microscope was employed to determine the compositional limits of the phase. Small amounts of anisotropic phases were easily distinguished from the isotropic cubic phase.

The compound, $Gd_2O_3 \cdot TiO_2$, was found to melt incongruently at 1775 °C and to have a reversible phase transition at 1712 °C. The x-ray powder diffraction patterns for the low and the high temperature polymorphs of the 1:1 compound are given in tables 3 and 4 respectively. Unfortunately, neither of the x-ray patterns of the polymorphs of $Gd_2O_3 \cdot TiO_2$ could be indexed on a unit cell based on the constants given by Queyroux [5]. Without a more complete reporting of Queyroux's data these discrepancies cannot be resolved. The x-ray diffraction powder pattern of the low temperature form (L–$Gd_2O_3 \cdot TiO_2$) was not indexed. However, the x-ray diffraction pattern of the high temperature form (H–$Gd_2O_3 \cdot TiO_2$) was indexed on the basis of a hexagonal cell, $a = 3.683$ Å, $c = 11.995$ Å. The high temperature polymorph is apparently related to the hexagonal A-type rare earth oxide through the relationship $c$ (hexagonal $Ln_2O_3$) $\cong \frac{1}{2} c$ (H – $Gd_2O_3 \cdot TiO_2$). Some difficulty was encountered in determining the inversion temperature since

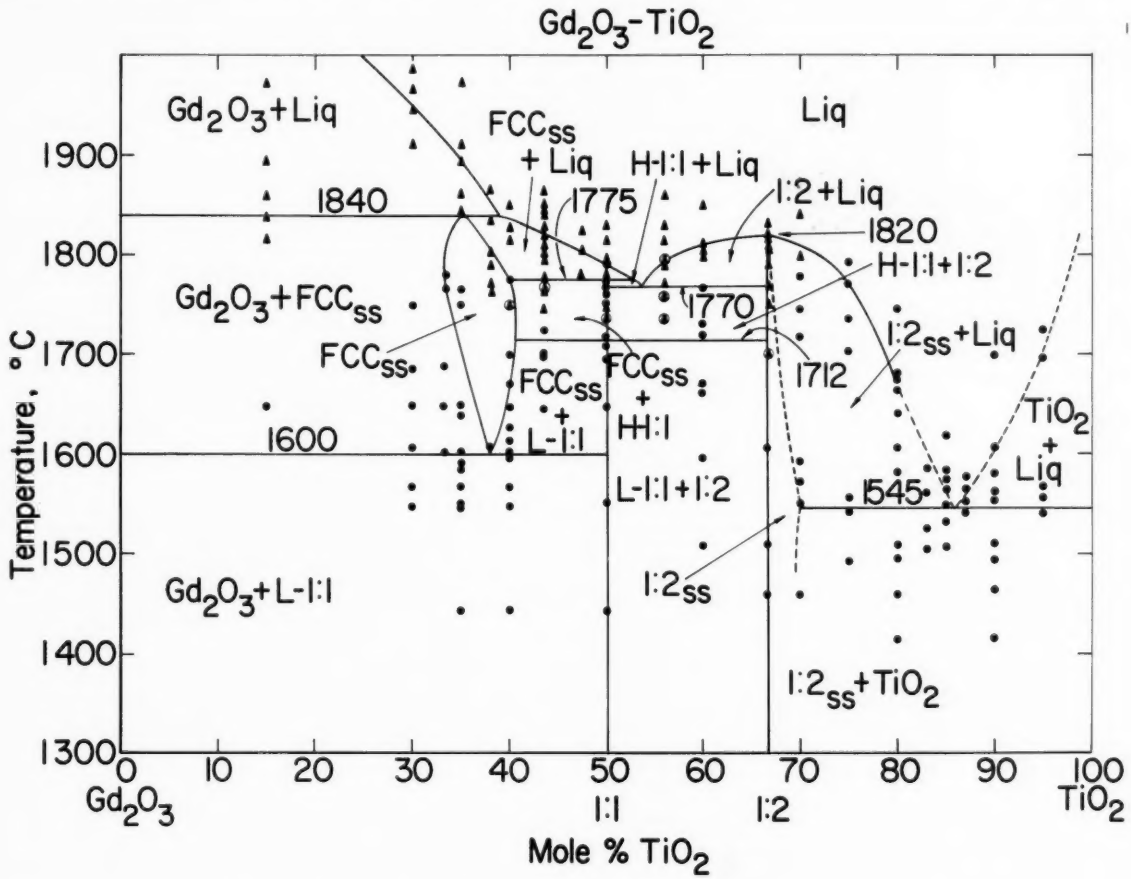


FIGURE 1. *Phase equilibrium diagram for the system* $Gd_2O_3$–$TiO_2$.
L-1:1 – Low temperature form of $Gd_2O_3 \cdot TiO_2$.
H-1:1 – High temperature form of $Gd_2O_3 \cdot TiO_2$.
1:2 – $Gd_2O_3 \cdot 2TiO_2$.
FCC – Face centered cubic phase.
ss – Solid solution.
Liq – Liquid.
● – Compositions and temperatures of experiments conducted in the quench furnace.
▲ – Compositions and temperatures of experiments conducted in the iridium crucible induction furnace.
● – Compositions and temperatures of experiments conducted in both the quenching and induction furnace.
For clarity, not all experimental data appearing in tables 1 and 2 are plotted on this diagram.

TABLE 1. *Experimental quenching data for compositions in the* $Gd_2O_3$–$TiO_2$ *system*

| Composition | | Heat treatment[a] | | X-ray analysis[b] | Remarks |
|---|---|---|---|---|---|
| $Gd_2O_3$ | $TiO_2$ | Temp. | Time | | |
| *Mole %* | *Mole %* | *°C* | *hr* | | |
| 85 | 15 | 1648 | 2.5 | $Gd_2O_3 + Fcc_m$ | |
| 70 | 30 | 1548 | 2 | $L–Gd_2O_3 \cdot TiO_2 + Gd_2O_3$ | |
| | | 1607 | 2.5 | $FCC_m + Gd_2O_3$ | |
| | | 1648 | 2.5 | $FCC_m + Gd_2O_3$ | |
| | | 1684 | 2.5 | $FCC_m + Gd_2O_3$ | |
| | | 1751 | 2 | $FCC_m + Gd_2O_3$ | |
| 66.67 | 33.33 | 1601 | 2 | $FCC_m + Gd_2O_3$[c] | |
| | | 1649 | 2 | $FCC_m + Gd_2O_3$ | |
| | | 1688 | 3 | $FCC_m + Gd_2O_3$ | |
| | | 1767 | 2 | $FCC_m + Gd_2O_3$ | |
| | | 1781 | 4 | $FCC_m$ | |
| 65 | 35 | 1444 | 64 | $L–Gd_2O_3 \cdot TiO_2 + Gd_2O_3$ | |
| | | 1550 | 2 | $L–Gd_2O_3 \cdot TiO_2 + Gd_2O_3$ | |
| | | 1567 | 3 | $L–Gd_2O_3 \cdot TiO_2 + Gd_2O_3$ | |
| | | 1584 | 2 | $L–Gd_2O_3 \cdot TiO_2 + Gd_2O_3$ | |
| | | 1601 | 2.5 | $FCC_m + (Gd_2O_3)$ | $Gd_2O_3$ not detected in x-ray pattern. |
| | | 1639 | 4 | $FCC_m + Gd_2O_3$[c] | |
| | | 1648 | 3 | $FCC_m + Gd_2O_3$ | |
| | | 1649 | 19 | $FCC_m + Gd_2O_3$[c] | |
| | | 1751 | 1 | $FCC_m$ | |
| | | 1767 | 2 | $FCC_m$ | |
| | | 1548 | 5 | $L–Gd_2O_3 \cdot TiO_2 + Gd_2O_3$ | Reheat of 1648 °C specimen. |
| 62 | 38 | 1606 | 6 | $FCC_m$ | No microscopic evidence of second phase. |
| 60 | 40 | 1444 | 64 | $L–Gd_2O_3 \cdot TiO_2 + Gd_2O_3$ | |
| | | 1567 | 3 | $L–Gd_2O_3 \cdot TiO_2 + Gd_2O_3$ | |
| | | 1599 | 16 | $L–Gd_2O_3 \cdot TiO_2 + Gd_2O_3$ | |
| | | 1601 | 2.5 | $FCC_m + (L–Gd_2O_3 \cdot TiO_2)$ | $L–Gd_2O_3 \cdot TiO_2$ not detected by x-ray diffraction; presumed to be present on basis of other data. |
| | | 1613 | 1 | $FCC_m + L–Gd_2O_3 \cdot TiO_2$ | |
| | | 1627 | 4 | $FCC_m + L–Gd_2O_3 \cdot TiO_2$ | |
| | | 1648 | 3 | $FCC_m + (L–Gd_2O_3 \cdot TiO_2)$ | $L–Gd_2O_3 \cdot TiO_2$ not detected by x-ray diffraction; presumed to be present on basis of other data. |
| | | 1672 | 2.5 | $FCC_m + L–Gd_2O_3 \cdot TiO_2$[c] | |
| 60 | 40 | 1700 | 1 | $FCC_m$ | |
| | | 1751 | 2 | $FCC_m$ | |
| | | 1776 | 66 | $FCC_m$ | Specimen partially melted. |
| | | 1548 | 3 | $L–Gd_2O_3 \cdot TiO_2 + Gd_2O_3$ | Reheat of 1648 °C specimen. |
| 56.45 | 43.55 | 1645 | 2.5 | $FCC_m + L – Gd_2O_3 \cdot TiO_2$ | |
| | | 1698 | 6 | $FCC_m + L–Gd_2O_3 \cdot TiO_2$ | |
| | | 1702 | 1 | $FCC_m + L–Gd_2O_3 \cdot TiO_2$ | |
| | | 1724 | 3 | $L–Gd_2O_3 \cdot TiO_2 + FCC_m + H–Gd_2O_3 \cdot TiO_2$ | Nonequilibrium mixture. |
| 50 | 50 | 1444 | 64 | $L–Gd_2O_3 \cdot TiO_2$ | |
| | | 1550 | 2 | $L–Gd_2O_3 \cdot TiO_2 + Gd_2O_3 + Gd_2O_3 \cdot 2TiO_2$ | Nonequilibrium mixture. |
| | | 1648 | 2.5 | $Gd_2O_3 \cdot 2TiO_2$ | Do. |
| | | 1696 | 1.5 | $Gd_2O_3 \cdot 2TiO_2$ | Do. |
| | | 1708 | 1 | $L–Gd_2O_3 \cdot TiO_2$ | |
| | | 1708 | 2 | $L–Gd_2O_3 \cdot TiO_2$ | |
| | | 1718 | 2.5 | $L–Gd_2O_3 \cdot TiO_2 + H–Gd_2O_3 \cdot TiO_2$ | $H–Gd_2O_3 \cdot TiO_2$ present in small amount. |
| | | 1738 | 1 | $L–Gd_2O_3 \cdot TiO_2 + H–Gd_2O_3 \cdot TiO_2$ | Do. |
| | | 1751 | 1 | $H–Gd_2O_3 \cdot TiO_2 + L–Gd_2O_3 \cdot TiO_2$ | |
| | | 1760 | 1 | $H–Gd_2O_3 \cdot TiO_2 + L–Gd_2O_3 \cdot TiO_2$ | |
| | | 1777 | .75 | $H–Gd_2O_3 \cdot TiO_2 + L–Gd_2O_3 \cdot TiO_2$ | Specimen partially melted $L–Gd_2O_3 \cdot TiO_2$ present in very small amount. |
| | | 1790 | 1 | $H–Gd_2O_3 \cdot TiO_2$ + unknown | Specimen partially melted. Extraneous x-ray peak $d = 3.0435$ Å probably represents nonequilibrium phase. |

TABLE 1. *Experimental quenching data for compositions in the* $Gd_2O_3$–$TiO_2$ *system*—Continued.

| Composition | | Heat treatment[a] | | X-ray analysis[b] | Remarks |
|---|---|---|---|---|---|
| $Gd_2O_3$ | $TiO_2$ | Temp. | Time | | |
| *Mole %* | *Mole %* | *°C* | *hr* | | |
| | | 1652 | 7 | L–$Gd_2O_3 \cdot TiO_2$ | Reheat of 1777 °C specimen. |
| | | 1754 | 5 | H–$Gd_2O_3 \cdot TiO_2$ + L–$Gd_2O_3 \cdot TiO_2$ | Reheat of 1790 °C specimen. |
| 44 | 56 | 1737 | 3.5 | H–$Gd_2O_3 \cdot TiO_2$ + $Gd_2O_3 \cdot 2TiO_2$ | |
| | | 1762 | .33 | H–$Gd_2O_3 \cdot TiO_2$ + $Gd_2O_3 \cdot 2TiO_2$ | |
| 40 | 60 | 1508 | 3 | L–$Gd_2O_3 \cdot TiO_2$ + $Gd_2O_3 \cdot 2TiO_2$ | |
| | | 1597 | 2 | L–$Gd_2O_3 \cdot TiO_2$ + $Gd_2O_3 \cdot 2TiO_2$ | |
| | | 1662 | 5 | L–$Gd_2O_3 \cdot TiO_2$ + $Gd_2O_3 \cdot 2TiO_2$ | |
| | | 1670 | 4 | L–$Gd_2O_3 \cdot TiO_2$ + $Gd_2O_3 \cdot 2TiO_2$ | |
| | | 1720 | 3.5 | $Gd_2O_3 \cdot 2TiO_2$ + H–$Gd_2O_3 \cdot TiO_2$ | |
| | | 1730 | 1.5 | $Gd_2O_3 \cdot 2TiO_2$ + H–$Gd_2O_3 \cdot TiO_2$ | |
| 33.33 | 66.67 | 1460 | 19 | $Gd_2O_3 \cdot 2TiO_2$ | |
| | | 1508 | 1 | $Gd_2O_3 \cdot 2TiO_2$ | |
| | | 1604 | 0.5 | $Gd_2O_3 \cdot 2TiO_2$ | |
| | | 1702 | 2 | $Gd_2O_3 \cdot 2TiO_2$ | |
| 30 | 70 | 1460 | 19 | $Gd_2O_3 \cdot 2TiO_{2ss}$ + $TiO_2$ | |
| 20 | 80 | 1416 | 25 | $Gd_2O_3 \cdot 2TiO_{2ss}$ + $TiO_2$ | |
| | | 1460 | 19 | $Gd_2O_3 \cdot 2TiO_{2ss}$ + $TiO_2$ | |
| 10 | 90 | 1416 | 25 | $TiO_2$ + $Gd_2O_3 \cdot 2TiO_{2ss}$ | |

[a] Unless otherwise indicated all specimens were first calcined at a 1000 °C–18 hr. and recalcined at 1000 °C–4 hr.
[b] Phases identified are given in order of amount present (greatest amount first) at room temperature.
[c] Second phase identified by use of petrographic microscope.

TABLE 2. *Melting characteristics of the* $Gd_2O_3$–$TiO_2$ *system*

| Composition[a] | | Temperature[b] | Furnace[c] | Observation |
|---|---|---|---|---|
| $Gd_2O_3$ | $TiO_2$ | | | |
| *Mole %* | *Mole %* | *°C* | | |
| 85 | 15 | 1816 | I | Not melted. |
| | | 1839 | I | Do. |
| | | 1860 | I | Partially melted. |
| | | 1897 | I | Do. |
| | | 1974 | I | Do. |
| 70 | 30 | 1911 | I | Do. |
| | | 1946 | I | Do. |
| | | 1967 | I | Completely melted. |
| | | 1987 | I | Do. |
| 65 | 35 | 1838 | I | Not melted. |
| | | 1841 | I | Partially melted. |
| | | 1845 | I | Do. |
| | | 1862 | I | Do. |
| | | 1894 | I | Completely melted. |
| | | 1911 | I | Do. |
| | | 1974 | I | Do. |
| 62 | 38 | 1765 | I | Not melted. |
| | | 1773 | I | Do. |
| | | 1790 | I | Do. |
| | | 1804 | I | Partially melted. |
| | | 1835 | I | Do. |
| | | 1867 | I | Completely melted. |
| 60 | 40 | 1751 | Q | Not melted. |
| | | 1776 | Q | Partially melted. |
| | | 1816 | I | Do. |
| | | 1829 | I | Do. |
| | | 1850 | I | Completely melted. |
| 56.45 | 43.55 | 1745 | I | Not melted. |
| | | 1765 | I | Do. |
| | | 1768 | I | Do. |
| | | 1779 | I | Partially melted. |
| | | 1796 | I | Do. |
| | | 1803 | I | Do. |
| | | 1811 | I | Do. |
| | | 1821 | I | Completely melted. |
| | | 1830 | I | Do. |
| | | 1841 | I | Completely melted. |
| | | 1849 | I | Do. |
| | | 1853 | I | Do. |
| | | 1866 | I | Do. |
| 52.60 | 47.40 | 1780 | I | Partially melted. |
| | | 1805 | I | Completely melted. |
| | | 1824 | I | Do. |
| 50 | 50 | 1772 | Q | Not melted. |
| | | 1777 | Q | Partially melted. |
| | | 1779 | I | Do. |
| | | 1782 | Q | Do. |
| | | 1795 | I | Completely melted. |
| | | 1790 | Q | Do. |
| | | 1814 | I | Do. |
| | | 1832 | I | Do. |
| 44 | 56 | 1737 | I | Not melted. |
| | | 1762 | Q | Not melted. |
| | | 1762 | I | Do. |
| | | 1773 | I | Partially melted. |
| | | 1790 | I | Do. |
| | | 1796 | I | Do. |
| | | 1797 | Q | Do. |
| | | 1813 | I | Completely melted. |
| | | 1830 | I | Do. |
| | | 1862 | I | Do. |
| | | 1996 | I | Do. |
| | | 2050 | I | Do. |
| 40 | 60 | 1767 | Q | Not melted. |
| | | 1799 | I | Partially melted. |
| | | 1806 | I | Do. |
| | | 1813 | I | Completely melted. |
| | | 1849 | I | Do. |

TABLE 2. *Melting characteristics of the* $Gd_2O_3$–$TiO_2$ *system*—Con.

| Composition [a] | | Temperature [b] | Furnace [c] | Observation |
|---|---|---|---|---|
| $Gd_2O_3$ | $TiO_2$ | | | |
| *Mole %* | *Mole %* | *°C* | | |
| 33.33 | 66.67 | 1752 | I | Not melted. |
| | | 1770 | I | Do. |
| | | 1792 | I | Do. |
| | | 1806 | I | Do. |
| | | 1810 | I | Do. |
| | | 1814 | I | Do. |
| | | 1823 | I | Melted. |
| | | 1834 | I | Do. |
| | | 1843 | I | Do. |
| | | 1850 | I | Do. |
| | | 1878 | I | Do. |
| 30 | 70 | 1550 | Q | Not melted. |
| | | 1573 | Q | Partially melted. |
| | | 1592 | Q | Do. |
| | | 1719 | Q | Do. |
| | | 1747 | Q | Do. |
| | | 1781 | Q | Do. |
| | | 1798 | I | Do. |
| | | 1840 | I | Completely melted. |
| 25 | 75 | 1490 | Q | Not melted. |
| | | 1541 | Q | Do. |
| | | 1555 | Q | Partially melted. |
| | | 1704 | I | Do. |
| | | 1736 | I | Do. |
| | | 1772 | I | Do. |
| | | 1794 | I | Completely melted. |
| 20 | 80 | 1495 | Q | Not melted. |
| | | 1508 | Q | Partially melted. |
| | | 1583 | Q | Do. |
| | | 1606 | Q | Do.[d] |
| | | 1641 | Q | Do. |
| | | 1664 | Q | Melted.[d] |
| | | 1677 | Q | Do. |
| | | 1683 | Q | Do. |
| | | 1747 | Q | Do. |
| 17 | 83 | 1505 | Q | Not melted. |
| | | 1525 | Q | Do. |
| | | 1562 | Q | Melted.[d] |
| | | 1585 | Q | Do. |
| 15 | 85 | 1506 | Q | Not melted. |
| | | 1533 | Q | Do. |
| | | 1549 | Q | Melted.[d] |
| | | 1565 | Q | Do. |
| | | 1575 | Q | Do. |
| | | 1584 | Q | Do. |
| | | 1618 | Q | Do. |
| 13 | 87 | 1542 | Q | Not melted. |
| | | 1553 | Q | Melted.[d] |
| | | 1564 | Q | Do. |
| | | 1576 | Q | Do. |
| 10 | 90 | 1465 | Q | Not melted. |
| | | 1495 | Q | Do. |
| | | 1511 | Q | Do. |
| | | 1554 | Q | Partially melted. |
| | | 1561 | Q | Do. |
| | | 1580 | Q | Melted.[d] |
| | | 1608 | Q | Do. |
| | | 1700 | Q | Do. |
| 5 | 95 | 1542 | Q | Not melted. |
| | | 1556 | Q | Partially melted. |
| | | 1568 | Q | Do. |
| | | 1694 | Q | Melted.[d] |
| | | 1725 | Q | Completely melted. |

[a] Specimens first calcined at 1000 °C for 18 hr and recalcined at 1000 °C for 4 hr.
[b] Specimens furnace cooled except when indicated.
[c] Q-quenching furnace; I-induction furnace. All specimens heated in induction furnace slow cooled rather than quenched.
[d] Definite verification of complete melting could not be obtained.

numerous attempts to quench H–$Gd_2O_3 \cdot TiO_2$ as a single phase below the solidus were unsuccessful. In each instance a small amount of L–$Gd_2O_3 \cdot TiO_2$ was present. However, the x-ray pattern of the partially melted 1:1 compound quenched from 1790 °C was found to be essentially single phase. One very weak extra line occurred in the x-ray pattern at $d = 3.044$ Å which was probably representative of a metastable phase formed only in the quenched liquid. Both the 33.33 and the 43.55 percent $TiO_2$ compositions when quenched from above 1712 °C, the inversion temperature of $Gd_2O_3 \cdot TiO_2$, contained H–$Gd_2O_3 \cdot TiO_2$ and an appropriate second phase. The same compositions quenched from below 1712 °C contained L–$Gd_2O_3 \cdot TiO_2$ and an appropriate second phase. These experimental data seem to indicate that the possibility of quenching H–$Gd_2O_3 \cdot TiO_2$ without residual traces of L–$Gd_2O_3 \cdot TiO_2$ is only accomplished by the presence of another second phase.

Other $Ln_2O_3 : TiO_2$ compositions were also studied. From x-ray powder diffraction data, it appears that the compositions $Sm_2O_3 : TiO_2$ and $Eu_2O_3 : TiO_2$ form phases which are very similar to both L–$Gd_2O_3 \cdot TiO_2$ and *H*–$Gd_2O_3 \cdot TiO_2$. The composition $Dy_2O_3$: $TiO_2$ was found to contain a mixture of phases, one of which is apparently similar to H–$Gd_2O_3 \cdot TiO_2$. These related phases were not detected in the equimolar compositions of the oxides of the smaller rare earth cations with $TiO_2$.

The compound $Gd_2O_3 \cdot TiO_2$ was found to melt congruently at 1820 °C. From the change in unit cell constants with composition the compound apparently accepted up to about 3 mole percent $TiO_2$ in solid solution. The unit cell dimensions of the compositions $Gd_2O_3 : 2TiO_2$ and $30Gd_2O_3 : 70TiO_2$ quenched from 1460 °C are 10.181 Å and 10.169 Å, respectively. Since the latter composition contained a small amount of $TiO_2$ the exsolution curve delineating the phase boundary is shown (fig. 1) as dashed at 69 percent $TiO_2$.

Earlier, the present authors [16] reported the parameters of the following $Ln_2O_3 \cdot 2TiO_2$ pyrochlore-type phases: $Eu_2O_3 \cdot 2TiO_2$ ($a = 10.195$); $Ho_2O_3 \cdot 2TiO_2$ ($a = 10.098$ Å); $Er_2O_3 \cdot 2TiO_2$ ($a = 10.075$ Å); $Tm_2O_3$

TABLE 3. *X-ray diffraction powder data for the low temperature modification of* $Gd_2O_3 \cdot TiO_2$ ($CuK_\alpha$ *radiation*)

| $d$[a] | $I/I_o$[b] |
|---|---|
| Å | |
| 7.70 | 21 |
| 3.56 | 21 |
| 3.066 | 100 |
| 3.060 | 79 |
| 3.054 | 64 |
| 2.976 | 14 |
| 2.947 | 14 |
| 2.667 | 64 |
| 2.624 | 14 |
| 2.566 | 17 |
| 2.554 | 21 |
| 2.334 | 11 |
| 2.130 | 14 |
| 2.113 | 14 |
| 1.925 | 14 |
| 1.896 | 10 |
| 1.869 | 21 |
| 1.661 | 19 |
| 1.648 | 10 |
| 1.607 | 26 |
| 1.601 | 11 |
| 1.597 | 43 |
| 1.586 | 29 |
| 1.583 | 17 |
| 1.569 | 14 |

[a] Interplanar spacing.
[b] Relative intensity.

TABLE 4. *X-ray diffraction powder data for the high temperature modification of* $Gd_2O_3 \cdot TiO_2$ [a] ($CuK_\alpha$ *radiation*)

| hkl [b] | d [c] | $1/d^2$ | | I/I₀ [e] |
|---|---|---|---|---|
| | | Obs | Cal [d] | |
| | Å | | | |
| 002 | 6.02 | 0.0276 | 0.0277 | 10 |
| 100 | 3.189 | .0983 | .0983 | 38 |
| 101 | 3.083 | .1052 | .1056 | 32 |
| | 3.0435 | .1080 | | 10 |
| 004 | 3.007 | .1105 | .1112 | 26 |
| 102 | 2.817 | .1260 | .1264 | 100 |
| 104 | 2.185 | .2094 | .2098 | 22 |
| 105 | 1.918 | .2720 | .2724 | 8 |
| 110 | 1.839 | .2958 | .2958 | 29 |
| 112 | 1.757 | .3239 | .3236 | 8 |
| 106 | 1.694 | .3484 | .3488 | 12 |
| 200 | 1.645 | .3944 | .3944 | 58 |
| 201 | 1.578 | .4017 | .4014 | 10 |
| 114 | 1.568 | .4070 | .4070 | 59 |
| 202 | 1.538 | .4227 | .4222 | 60 |
| 212 | 1.1801 | .7183 | .7181 | 8 |
| 300 | 1.0612 | .8881 | .8875 | 8 |

[a] Specimen not single phase. The line which occurs at $d = 3.0435$ Å probably represents a metastable phase formed only in the quenched liquid.
[b] Hexagonal Miller indices.
[c] Interplanar Spacing.
[d] Based on a hexagonal cell, $a = 3.683$ Å, $c = 11.995$ Å.
[e] Relative intensity.

$\cdot 2TiO_2$ ($a = 10.055$ Å) and $Lu_2O_3 \cdot 2TiO_2$ ($a = 10.023$ Å). Subsequent work by Brixner [4] confirmed these earlier data.

The eutectic between $Gd_2O_3 \cdot 2TiO_2$ and $TiO_2$ is shown (fig. 1) as occurring at approximately 86 mole percent $TiO_2$. Some difficulty was encountered in establishing the liquidus curves near the eutectic composition because it was virtually impossible to distinguish a partially melted from a completely melted specimen. For this reason, the eutectic composition shown in fig. 1 was approximated. Since the melting point of $TiO_2$ was not redetermined the liquidus was dashed from the eutectic composition to approximately 100 percent $TiO_2$.

## 5. Summary


The phase equilibrium diagram for a major portion of the $Gd_2O_3$–$TiO_2$ system has been determined from a study of solid state reactions and melting point relations.

A platinum alloy quenching furnace was used to establish all of the subsolidus and some of the liquidus relationships below 1800 °C. An inductively heated iridium crucible was used for the determination of solidus and liquidus relationships above 1800 °C. Phases were identified by x-ray powder diffraction and polarizing microscopic techniques.

Three intermediate phases were formed in the system. A solid solution phase is indicated on the phase diagram as existing from 33 to 40 mole percent $TiO_2$, at 1750 °C. This phase melts incongruently over a range of temperatures and compositions varying from 1840 °C, the peritectic temperature, at 35 mole percent $TiO_2$ to 1775 °C, at 40 mole percent $TiO_2$ the incongruent melting temperature of $Gd_2O_3 \cdot TiO_2$. The minimum temperature of stability for the phase is 1600 °C at 38 mole percent $TiO_2$. The x-ray diffraction pattern of the solid solution phase was indexed on the basis of a face-centered cubic cell with unit cell dimension varying from about 5.28 Å to 5.32 Å at 1750 °C. The second phase, a 1 : 1 compound, melts incongruently at 1775 °C and has a reversible phase transition at 1712 °C. The high temperature modification was indexed on the basis of a hexagonal cell related to the hexagonal rare earth oxides with $a = 3.683$ Å, $c = 11.995$ Å. The third phase, $Gd_2O_3 \cdot 2TiO_2$, melts congruently at 1820 °C. This phase apparently accepted up to about 3 mole percent $TiO_2$ in solid solution at 1460 °C. The unit cell dimensions of this pyrochlore structure type were found to vary from approximately 10.181 Å to 10.169 Å. From x-ray powder diffraction data the equimolar compositions of either $Sm_2O_3$ or $Eu_2O_3$ with $TiO_2$ were found to form phases which were very similar to both the low and high temperature modifications of $Gd_2O_3 \cdot TiO_2$. The composition $Dy_2O_3$ : $TiO_2$ apparently formed several phases one of which was apparently similar to the high temperature form of $Gd_2O_3 \cdot TiO_2$.


## 6. References


[1] S. J. Schneider, R. S. Roth, and J. L. Waring, J. Res. NBS **65A** (Phys. and Chem.) No. 4, 345–374 (1961).
[2] J. B. MacChesney and H. A. Sauer, J. Am. Ceram. Soc. **45,** No. 9, 416–422 (1962).
[3] R. S. Roth, J. Res. NBS **56,** No. 1, 17–25 (1956) RP2643.
[4] L. H. Brixner, Inorg. Chem. **3,** No. 7, 1065–67 (1964).
[5] F. Queyroux, Bull. Soc. Franc. Mineral. Crist. **86,** No. 3, 295–296 (1963).
[6] R. S. Roth and S. J. Schneider, J. Res. NBS **64A** (Phys. and Chem.) No. 4, 309–316 (1960).
[7] R. Roy, I. Warshaw, and Y. Ukai, Third Quarterly Progress Report on Crystal Chemistry Studies (Oct. 1, 1960-Dec. 30, 1960), File No. 40608–P–M–60–93–93, The Pennsylvania State University, 1–104 (1961).
[8] M. Perez y Jorba, Thèses Contribution à l'etude des systèmes zircone-oxyde de terres rares. Faculté Des Sciences De L'Université De Paris 1–33 (1962).
[9] Swanson and Tatge, NBS Circ. 539, Vol. **I,** 44 (1953).
[10] H. F. Stimson, J. Res. NBS **65A** (Phys. and Chem.) No. 2, 139–145 (1961).
[11] S. J. Schneider and J. L. Waring, J. Res. NBS **67A** (Phys. and Chem.) No. 1, 19–25 (1963).
[12] F. A. Mauer, Bridge-type Furnance Controller using Brown Servoamplifier, Informal Communiation; see also R. H. Bogue, Chemistry of Portland Cement, 2d ed. p. 311 (Reinhold Publishing Corp., New York, 1955).
[13] L. G. Wisnyi and S. Pijanowski, Metal Report of Tech. Dept., Mar., Apr., and May. U.S. AEC Publ. Kapl–1564, 19–20 (1956).
[14] C. E. Curtis and J. R. Johnson, J. Am. Ceram. Soc. **40,** 15–19 (1957).
[15] S. J. Schneider, NBS Monograph 68 (1963),
[16] J. L. Waring and S. J. Schneider, Bull. Amer. Ceram. Soc. **43,** No. 4, 263 (1964).



(Paper 69A3–344)

JOURNAL OF RESEARCH of the National Bureau of Standards—A. Physics and Chemistry
Vol. 69A, No. 3, May–June 1965

# Acid-Base Behavior in 50-Percent Aqueous Methanol: Thermodynamics of the Dissociation of Protonated Tris(hydroxymethyl)aminomethane and Nature of the Solvent Effect*

Maurice Woodhead,[1] Maya Paabo, R. A. Robinson, and Roger G. Bates

(February 16, 1965)

Electromotive-force methods and cells without liquid junction have been utilized to determine the acidic dissociation constant of protonated tris(hydroxymethyl)aminomethane [2-amino-2-(hydroxymethyl)-1, 3-propanediol] in 50 wt percent methanol solvent at seven temperatures from 10 to 40 °C. The change of the dissociation constant with temperature has been used to calculate the changes of enthalpy, entropy, and heat capacity when the dissociation takes place in the standard state. Comparisons with earlier measurements in the aqueous medium reveal no great differences in the enthalpy and entropy, suggesting that water participates in preference to methanol in the protolytic reaction even in 50-percent methanol. It is shown that electrostatic considerations alone are unable to explain the solvent effect on the dissociation energy, and a substantial "basicity effect" is indicated. The activity-coefficient term for the amine hydrochloride in equimolal amine-salt buffers has been evaluated and compared with similar data in the water solvent.

## 1. Introduction

Acid-base studies of organic compounds only slightly soluble in water are sometimes conveniently made in a solvent consisting of equal parts by weight of water and methanol. In order to facilitate the determination of *p*H and *pK* in 50-percent methanol, an operational *p*H scale has recently been established for this solvent mixture [1][2]. The standard scale, defined in a manner consistent with thermodynamic dissociation constants and activity coefficients in 50-percent methanol, is fixed by three suitable reference solutions, namely an acetate buffer, a phosphate buffer, and a solution of sodium hydrogen succinate.

As a part of the earlier work, the dissociation constants of acetic acid and dihydrogen phosphate ion in 50-percent methanol were determined from 10 to 40 °C. These two acids are of charge types $A^0B^-$ and $A^-B^=$, respectively. Here A and B refer respectively to the acid and its conjugate base. The results for the enthalpy and entropy of ionization in 50-percent methanol were of interest for their bearing on the relation between charge type and solvent effect.

The dissociation constant of an acid of charge type $A^+B^0$, namely the acid conjugate to the weak uncharged base 2-amino-2-(hydroxymethyl)-1, 3-propanediol or tris(hydroxymethyl)aminomethane,[3] has been studied in 50-percent methanol from 10 to 40 °C. The associated thermodynamic quantities have been derived. Buffer solutions composed of this primary amine and its salt have proved extraordinarily useful for *p*H control in biological systems [2].

## 2. Experimental Methods

### 2.1. Materials

An aqueous solution of twice-distilled hydrochloric acid was used as a primary standard. Its molality was determined by gravimetric chloride determination; the standard deviation derived from three determinations was 0.01 percent. The purity of four lots of crystalline tris(hydroxymethyl)aminomethane (obtained from commercial sources) was found to be 99.92, 99.94, 99.94, and 100.22 percent by titration with the standard solution of hydrochloric acid. Weight burets were used, and each sample was adjusted to the theoretical equivalence point (*p*H 4.54 in a 0.1 *M* solution of the neutralized base) with the aid of glass-electrode measurements.

*Presented before the Division of Analytical Chemistry at the 149th National meeting of the American Chemical Society, Detroit, Mich., on April 7, 1965.

[1] Guest worker, on leave from Makerere University College, Kampala, Uganda.

[2] Figures in brackets indicate the literature references at the end of this paper.

[3] For brevity, this base will sometimes be referred to as "tris" and the corresponding hydrochloride as "tris hydrochloride."

For convenience, many of the cell solutions were prepared from a commercial grade of tris hydrochloride together with the free base. The emf of cells containing buffer solutions prepared in this way was compared with solutions of identical nominal molalities prepared from tris and the standard solution of hydrochloric acid. Three buffer concentrations spanning the range covered in the study were compared in this way. The difference in emf was found to be 0.39 mV with a standard deviation of 0.05 mV. The cells prepared with the tris hydrochloride gave the higher emf. The recorded emf for cells prepared in this way was adjusted to correspond to that obtainable with pure tris (assay 100%) and the standard solution of hydrochloric acid.

On examination, the tris hydrochloride obtained commercially was found to be very close to stoichiometric neutrality; measurements of *p*H and buffer capacity showed that the product contained no appreciable excess of either the base or of hydrochloric acid. Analysis for chloride by gravimetry showed, however, that the acidic and basic components, while present in equivalent amounts, were both present in lower quantity than expected (about 99.1 percent of theoretical). Furthermore, samples of the salt prepared by the authors by neutralizing the pure tris with hydrochloric acid were also found to assay from 99.1 to 99.6 percent.

The inert impurity in the commercial product, thought to be water by the manufacturer, could not be identified.[4] Drying at temperatures low enough to preclude decomposition of the salt did not materially increase the assay value.[5] Although drying brought about some improvement in the results of the carbon and hydrogen analysis, the figures were inconclusive:

| | Carbon, percent | Hydrogen, percent |
|---|---|---|
| Commercial sample | 30.81 | 7.83 |
| | 30.56 | 7.69 |
| Commercial sample, after drying | 30.60 | 7.69 |
| | 30.60 | 7.84 |
| Theoretical | 30.49 | 7.67 |

The supposition that the impurity was electrochemically inert was confirmed by a comparison of the correction to the emf observed (0.39 mV) with that to be expected from the known assay (0.46 mV). The difference corresponds to only 0.001 unit in *pK*.

The methanol with which the solvents were prepared was "Spectro Grade," of the same quality as that used in the earlier studies in 50 wt percent methanol solvents [1, 4].

[4] Datta, Grzybowski, and Wilson [3] reported a similar low chloride assay for the samples of tris hydrochloride prepared for their study of the dissociation of tris in aqueous solution.

[5] Analysis of the dried sample by gas chromatography and by Karl Fischer methods indicated the presence of 0.1 to 0.3 percent of water. The authors are indebted to R. J. Hall for these results and for the elemental analysis.

### 2.2. Procedures

In general, the experimental procedures followed those used in determining the dissociation constant of tris in water [5]. Electromotive force measurements of the cell

$$\mathrm{Pt;H_2(g,\ 1\ atm),\ tris\cdot HCl}(m_1),\ \mathrm{tris}(m_2)\ \text{in 50 wt percent methanol, AgCl; Ag}$$

where $m_1$ and $m_2$ are molalities, were used. Thirty-four solutions, all with buffer ratio close to unity, were studied. When tris hydrochloride was used, a stock buffer solution was prepared by weighing the free base, the salt, and water. The remainder of the solutions were prepared by dissolving a known weight of tris in a known weight of standard hydrochloric acid. The necessary weight of methanol was then added, together with more water, to achieve the desired solvent composition.

Each cell contained one hydrogen electrode and one silver-silver chloride electrode. The emf measurements at the seven temperatures were made in a variety of sequences. A complete series required from two to three days. The solubility of silver chloride in a methanol-water solution of tris was not determined, as it had been found insufficient to require corrections in aqueous solutions [5]. Methanol is presumed to lower the solubility still further.

### 2.3. Results

The emf data are summarized in table 1. Corrections have been made to the reference hydrogen partial pressure of 1 atm with the aid of the recorded barometric pressure and the known total vapor pressure of the methanol-water solvent at the temperature in question [4]. The emf recorded for those solutions prepared by weighing tris and the solid hydrochloride was further corrected for the known deficiency of ionized chloride in these solutions.

## 3. Calculation of the Dissociation Constant

The calculation of $pK$, where $K$ is the acidic dissociation constant of 2-ammonium-2-(hydroxymethyl)-1,3−propanediol (that is, tris$\cdot H^+$) in water, has been described in detail in earlier papers [3, 5]. The corresponding dissociation constant in 50 wt percent methanol, referred not to the standard state in water but to that in this solvent, is termed $p({}_sK)$. The procedure for obtaining $p({}_sK)$ is entirely analogous to that for the computation of $pK$ (that is, $p({}_wK)$) in water.

"Apparent" values of $p({}_sK)'$ were computed from the emf $E$ by the equation

$$p({}_sK)' \equiv p({}_sK) - \beta I = \frac{E - {}_sE^\circ}{(RT \ln 10)/F} + 2 \log m_1 - \log m_2 - \frac{2A\sqrt{I}}{1 + B\mathring{a}\sqrt{I}} \quad (1)$$

TABLE 1. *Electromotive force of the cell Pt;* $H_2$*(g, 1 atm), tris* HCl($m_1$), *tris*($m_2$) *in 50 wt % methanol,* AgCl; Ag *from 10 to 40 °C (in volts)*

| $m_1^a$ | Temperature, °C | | | | | | |
|---|---|---|---|---|---|---|---|
| | 10 | 15 | 20 | 25 | 30 | 35 | 40 |
| Series I: $m_2 = 1.0080\ m_1$ | | | | | | | |
| 0.009554 | 0.78772 | 0.78553 | 0.78343 | ..... | ..... | ..... | ..... |
| .009566 | ..... | ..... | ..... | ..... | 0.77857 | 0.77626 | 0.77394 |
| .009575 | .78781 | .78567 | .78353 | .78099 | .77917 | .77681 | .77427 |
| .01921 | .77366 | .77117 | .76898 | .76646 | .76365 | .76097 | .75839 |
| .01922 | .77331 | ..... | ..... | ..... | .76372 | .76092 | .75812 |
| .02892 | .76635 | .76388 | .76135 | .75862 | ..... | ..... | ..... |
| .02892 | .76606 | .76357 | .76079 | .75830 | .75584 | .75298 | .75015 |
| .03871 | .76056 | .75799 | .75538 | .75276 | .75001 | .74713 | .74414 |
| .03872 | .76083 | .75830 | .75571 | .75299 | .75000 | .74712 | .74426 |
| .04857 | .75609 | .75354 | .75086 | .74800 | ..... | ..... | ..... |
| .04857 | .75646 | .75384 | .75102 | .74829 | .74558 | .74263 | .73973 |
| .04861 | .75624 | .75375 | .75106 | .74831 | .74564 | .74253 | .73932 |
| .05854 | .75322 | .75066 | .74787 | .74506 | .74205 | .73911 | .73607 |
| .06849 | .75042 | .74777 | .74503 | .74222 | .73921 | .73616 | .73307 |
| .06852 | .75031 | .74759 | .74482 | .74203 | .73915 | .73610 | .73311 |
| .07867 | .74773 | .74499 | .74230 | .73941 | .73648 | .73340 | .73037 |
| .07869 | .74789 | .74518 | .74239 | .73945 | .73630 | .73331 | .73017 |
| .08882 | .74589 | .74313 | .74033 | .73745 | .73431 | .73121 | .72810 |
| .09910 | .74397 | .74114 | .73840 | .73545 | .73255 | .72934 | .72618 |
| Series II: $m_2 = 1.0037\ m_1$ | | | | | | | |
| 0.01928 | 0.77339 | 0.77164 | 0.76912 | 0.76672 | 0.76381 | 0.76101 | 0.75826 |
| .03889 | .75992 | .75774 | .75545 | .75269 | .74992 | .74706 | .74417 |
| .05880 | .75248 | ..... | .74719 | .74464 | .74203 | .73906 | .73622 |
| .07900 | .74808 | .74532 | .74236 | .73958 | .73629 | .73321 | .73049 |
| .09948 | .74429 | .74149 | .73845 | .73564 | .73231 | .72925 | .72621 |
| Series III: $m_2 = m_1$ | | | | | | | |
| 0.01922 | 0.77405 | 0.77154 | 0.76925 | 0.76673 | 0.76415 | 0.76150 | 0.75856 |
| .03872 | .76077 | .75789 | .75541 | .75288 | .75020 | .74733 | .74421 |
| .05854 | .75304 | .75029 | .74774 | .74494 | .74200 | .73907 | .73595 |
| .07864 | .74796 | .74512 | .74242 | .73956 | .73656 | .73357 | .73044 |
| .09910 | .74371 | .74098 | .73829 | .73538 | .73230 | .72934 | .72610 |
| Series IV: $m_2 = 1.0022\ m_1$ | | | | | | | |
| 0.009576 | 0.78818 | 0.78571 | 0.78349 | 0.78128 | 0.77888 | 0.77649 | 0.77386 |
| .02894 | .76588 | .76331 | .76075 | .75825 | .75558 | .75273 | .74979 |
| .04857 | .75614 | .75357 | .75092 | .74824 | .74536 | .74239 | .73945 |
| .06853 | .75015 | .74743 | .74469 | .74189 | .73890 | .73579 | .73270 |
| .08890 | .74534 | .74261 | .73982 | .73700 | .73396 | .73089 | .72780 |

[a] Tris hydrochloride was used to prepare the solutions of Series I and II, but hydrochloric acid was used for Series III and IV.

where $A$ and $B$ are constants of the Debye-Hückel theory [6, 7] and $\mathring{a}$ is the "ion-size parameter." The values of the standard emf ${}_sE°$ in 50 wt percent methanol have been reported elsewhere [4].

The acidic strength of tris hydrochloride in this solvent, as in water, falls in the region where solvolysis of both the free base and the protonated base is minimal; hence, the buffer ratio is accurately given by $m_2/m_1$, and the ionic strength $I$ is identical with $m_1$. The thermodynamic $p({}_sK)$ is obtained by extrapolating values of $p({}_sK)'$ to the limit of $I=0$ ("infinite dilution"). If the Debye-Hückel equation is an adequate representation of the activity-coefficient term, the plot of $p({}_sK)'$ as a function of $I$ will be a straight line of slope $-\beta$ when a suitable value of the ion-size parameter $\mathring{a}$ is chosen. It will usually be curved for other values of $\mathring{a}$.

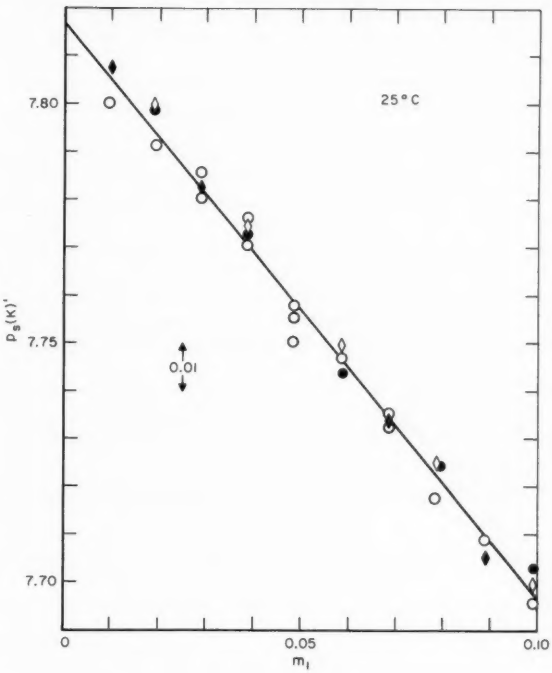


FIGURE 1. *Plot of the apparent* $p({}_sK)$ *in 50-percent methanol as a function of* $m_1$ *at 25 °C.*
○ Series I.
● Series II.
◇ Series III.
◆ Series IV.

Figure 1 is a plot of the data at 25 °C. This straight line was obtained with a value of 0 for $\mathring{a}$: it corresponds to a slope $-\beta = 1.220$. The same value of $\mathring{a}$ proved suitable for the extrapolation at all temperatures from 10 to 40 °C. The intercepts $p({}_sK)$ are summarized in table 2, together with the standard deviations of the intercepts and the values of $p({}_wK)$ found in previous investigations [3, 5]. These "observed" values of $p({}_sK)$ can be represented within about 0.001 unit by the following equation, which is of the form proposed by Harned and Robinson [8]:

$$p({}_sK) = \frac{A_1}{T} - A_2 + A_3 T = \frac{3689.57}{T} - 8.5466 + 0.013381T \qquad (2)$$

TABLE 2. $p({}_sK)$ *values for the protonated form of tris in 50 wt percent methanol from 10 to 40 °C*

| $t$ | $p({}_sK)$ | $\sigma_t$ | $p({}_sK)$ (calc.) | $p({}_wK)$ |
|---|---|---|---|---|
| °C | | | | |
| 10 | 8.273 | 0.002 | 8.273 | 8.516 |
| 15 | 8.113 | .001 | 8.114 | 8.361 |
| 20 | 7.962 | .001 | 7.962 | 8.213 |
| 25 | 7.818 | .001 | 7.818 | 8.072 |
| 30 | 7.681 | .001 | 7.681 | 7.934 |
| 35 | 7.550 | .001 | 7.550 | 7.802 |
| 40 | 7.426 | .001 | 7.426 | 7.676 |



766-033 O - 65 - 4

where $T$ is the temperature in °K. The $p(_sK)$ calculated by eq (2) is given in the next to the last column of table 2.

It is evident that the protonated form of tris(hydroxymethyl)aminomethane is a stronger acid in 50 wt percent methanol than it is in pure water, where the $pK$ is 8.072 at 25 °C [3, 5]. This increase of strength is in accord with earlier measurements of the solvent effect of methanol on acids of this charge type [9, 10, 11]. In general, the $p(_sK)$ goes through a minimum in the range of solvent compositions between 70 and 90 wt percent methanol and then rises sharply as the concentration of solvent water becomes low. It has been shown that this behavior cannot be explained by the electrostatic effects of the changing dielectric constant alone. Nevertheless, qualitative consistency among the solvent effects on $pK$ for acids of different charge types can be achieved if a second parameter characterizing the alteration in the basicity of the medium is introduced [12].

## 4. Thermodynamic Constants for the Dissociation

### 4.1. Calculation of the Thermodynamic Quantities

By the application of the usual thermodynamic formulas to eq (2), the changes of Gibbs energy, enthalpy, entropy, and heat capacity for the dissociation of the protonated form of tris in the standard state were calculated. The results from 10 to 40 °C are given by the equations

$$\frac{\Delta G^\circ}{\text{J mol}^{-1}} = 19.1445(A_1 - A_2T + A_3T^2) \qquad (3)$$

$$\frac{\Delta H^\circ}{\text{J mol}^{-1}} = 19.1445(A_1 - A_3T^2) \qquad (4)$$

$$\frac{\Delta S^\circ}{\text{J mol}^{-1}\ \text{deg}^{-1}} = 19.1445(A_2 - 2A_3T) \qquad (5)$$

$$\frac{\Delta C_p^\circ}{\text{J mol}^{-1}\ \text{deg}^{-1}} = -19.1445(2A_3T). \qquad (6)$$

The values of these thermodynamic quantities in 50 wt percent methanol are compared in table 3 with the same quantities for the dissociation in the aqueous medium [3, 5]. The standard deviations in 50-percent methanol can be estimated by the procedure outlined by Please [13]. Assuming a standard deviation of 0.001 in $p(_sK)$, the results of the estimate are as follows:

$\Delta G^\circ$, 3 J mol$^{-1}$

$\Delta H^\circ$, 64 J mol$^{-1}$

$\Delta S^\circ$, 0.22 J mol$^{-1}$ deg$^{-1}$

$\Delta C_p^\circ$, 15 J mol$^{-1}$ deg$^{-1}$.

TABLE 3. *Thermodynamic quantities for the acidic dissociation of the protonated form of tris at 25 °C*

| | In water | | In 50-percent methanol |
|---|---|---|---|
| | Ref. [3] | Ref. [5] | |
| $\Delta G^\circ$/kJ mol$^{-1}$ | 46.06 (46.06) | 46.07 | 44.62 |
| $\Delta H^\circ$/kJ mol$^{-1}$ | 47.80 (47.41) | 47.60 | 47.86 |
| $\Delta S^\circ$/J mol$^{-1}$ deg$^{-1}$ | 5.81 (4.52) | 5.11 | 10.9 |
| $\Delta C_p^\circ$/J mol$^{-1}$ deg$^{-1}$ | −69.5 (−91.4) | −63.6 | −153 |

All of the values given were derived from a three-constant equation of the same form as eq (2) except those given in parentheses. In calculating these, $pK$ was fitted to a four-constant equation (represented by eq (2) with an additional term $A_4T^2$ added to the right-hand side).

The replacement of one-half of the water solvent, on a weight basis, by methanol has evidently failed to produce profound changes of a magnitude and character sufficient to suggest that the solvation pattern has been drastically altered. It seems likely, therefore, that the fundamental dissociation process in 50-percent methanol is, as in water, the transfer of a proton from combination with tris to combination with a basic water molecule.

### 4.2. Significance of the Solvent Effect

The effect of solvent on the Gibbs energy change for the dissociation of a weak acid has sometimes been ascribed to a change in the electrostatic self-energy of the ions. The simplest expression for the electrostatic energy of a mole of univalent ions is that of Born [14]:

$$G_{el} = \frac{Ne^2}{2}\frac{1}{\epsilon r_s} \qquad (7)$$

where $N$ is the Avogadro number, $e$ the electronic charge, $\epsilon$ the dielectric constant of the medium, and $r_s$ the radius of the (spherical) ion. The assumption made here is that the solvent is a continuous medium with a dielectric constant equal at all points to the macroscopic dielectric constant.

The dissociation of tris $H^+$ is an isoelectric process:

$$BH^+ + SH = B + SH_2^+$$

where $BH^+$ represents the protonated base and SH is the amphiprotic solvent. The change in electrostatic energy on transfer from water to 50-percent methanol is then

$$\Delta G_{el} = \frac{Ne^2}{2}\left(\frac{1}{\epsilon'} - \frac{1}{\epsilon}\right)\left(\frac{1}{r_{H^+}} - \frac{1}{r_{BH^+}}\right) \qquad (8)$$

where $\epsilon'$ is the dielectric constant of 50-percent methanol (56.3 at 25 °C) and $\epsilon$ is that of water (78.30 at 25 °C). Thus $\Delta G_{el}$ will have a positive value if $r_{BH^+} > r_{H^+}$. Although the value to be assigned to the radius of the hydrogen ion (designated $SH_2^+$, or simply $H^+$ in the absence of precise knowledge of its solvated structure) may be in dispute, it is difficult to see how this radius could be larger than that of the protonated tris cation, $BH^+$.

An atom model of the tris cation shows that this ion is not unlike the tetraethylammonium ion in size and shape. A radius of 4 Å has been ascribed to the latter [6], and it may be taken as a reasonable estimate of the radius of the tris cation as well. An ion with this radius contributes 0.87 kJ $mol^{-1}$ to the electrostatic energy change on transfer from water to 50-percent methanol.

The difficulty in applying eq (8) to an acidic dissociation process lies in our ignorance of the effective radius of the hydrogen ion. There is, however, considerable evidence [15] that the hydrogen ion is intimately associated with four water molecules in solvents containing a considerable amount of water, and we can reasonably identify the radius of this hydrated hydrogen ion with the diameter of the water molecule, 2.8 Å. An ion of this size contributes 1.24 kJ $mol^{-1}$ to the electrostatic energy.

The total electrostatic effect on dissociation of the protonated form of tris should therefore be 0.4 kJ $mol^{-1}$. The experimental value of $-1.45$ kJ $mol^{-1}$ is very different and of opposite sign. A similar anomaly seems to hold for all protonated bases, for example *o*-chloroanilinium ion and *m*-nitroanilinium ion [12]. This result has been ascribed to an increase in the basicity of the solvent on the addition of methanol, which may well be due to a degradation of the water structure by methanol. A structure-promoting entity is more effective in a methanolic solvent than in water, because there are more opportunities for the water structure to be promoted.

Hydrogen ion should be one of the best structure promoters, and therefore we have a reasonable explanation of the increase in acidity of protonated tris on addition of methanol. The magnitude of the effect is surprising, however; it must be of the order of $-2$ kJ $mol^{-1}$ if the total effect is $-1.45$ kJ $mol^{-1}$ and $+0.4$ kJ $mol^{-1}$ must be ascribed to the electrostatic effect.

It is worthwhile to consider whether this discrepancy may be due to inadequacies of the simple Born treatment. In an effort to explain the Gibbs energy changes on the transfer of electrolytes from water to deuterium oxide, Hepler [16] has recently considered the consequences of assuming a model suggested by the work of Ritson and Hasted [17]. Three regions of solvent distribution around an ion are distinguished in this treatment. From the surface of the ion of radius $r_s$ to a distance 1.5 Å from its center is a region of dielectric saturation, with a dielectric constant $\epsilon_{sat}$. For water solvents, $\epsilon_{sat}$ may be taken as 5 [16]. At distances ($r$) greater than 4 Å from the center of the ion, the solvent has its macroscopic dielectric constant $\epsilon_0$. In the intermediate region, the dielectric constant varies linearly with $r$:

$$\epsilon = \frac{\epsilon_0 - \epsilon_{sat}}{2.5}(r - 1.5) + \epsilon_{sat}. \qquad (9)$$

The variation of the dielectric constant in water and in 50-percent methanol with distance from the center of the ion is shown schematically in figure 2.

The electrostatic energy of a univalent ion is then given by

$$G_{el} = \frac{e^2}{2}\left\{\int_{r_s}^{1.5}\frac{dr}{\epsilon_{sat}r^2} + \int_{1.5}^{4}\frac{dr}{(Xr - Y)r^2} + \int_{4}^{\infty}\frac{dr}{\epsilon_0 r^2}\right\} \qquad (10)$$

where $X = 0.4(\epsilon_0 - \epsilon_{sat})$ and $Y = 1.5X - \epsilon_{sat}$. Upon integration we obtain

$$G_{el} = \frac{e^2}{2}\left\{\frac{1}{\epsilon_{sat}}\left(\frac{1}{r_s} - \frac{1}{1.5}\right) - \frac{0.417}{Y} + \frac{X}{Y^2}\ln\frac{0.375\epsilon_0}{\epsilon_{sat}} + \frac{0.25}{\epsilon_0}\right\}. \qquad (11)$$

For the transfer of a mole of ions from water to another solvent (identified by a prime mark), we have

$$\Delta G_{el} = \frac{Ne^2}{2}\left\{\left(\frac{1}{\epsilon'_{sat}} - \frac{1}{\epsilon_{sat}}\right)\left(\frac{1}{r_s} - \frac{1}{1.5}\right) - 0.417\left(\frac{1}{Y'} - \frac{1}{Y}\right) + \frac{X'}{(Y')^2}\ln\frac{0.375\epsilon'_0}{\epsilon'_{sat}} - \frac{X}{Y^2}\ln\frac{0.375\epsilon_0}{\epsilon_{sat}} + 0.25\left(\frac{1}{\epsilon'_0} - \frac{1}{\epsilon_0}\right)\right\}. \qquad (12)$$

For an ion of radius 4 Å, only the last term of eq (10) appears, and the electrostatic energy of the ion is identical with that calculated by the Born equation. Thus the electrostatic energy ($\Delta G_{BH^+}$) of the protonated tris cation is still 0.87 kJ $mol^{-1}$. If the hydrogen ion has a radius of 2.8 Å, the first term of eq (10) disappears and the integration of the second term is to be made

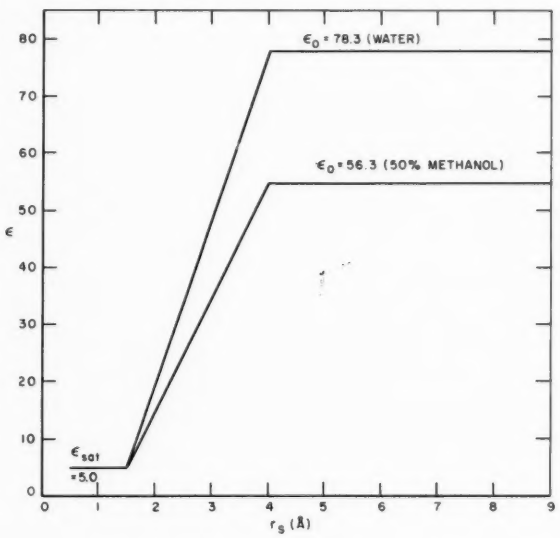


FIGURE 2. *Variation of the dielectric constant of water and 50-percent aqueous methanol in the vicinity of an ion; $r_s$ is the distance from the center of the ion.*



766-033 O - 65 - 5

from 2.8 to 4 Å. Equation (12) now becomes

$$\Delta G_{el}=\frac{Ne^2}{2}\left\{-0.107\left(\frac{1}{Y'}-\frac{1}{Y}\right)+\frac{X'}{(Y')^2}\ln\frac{0.7\epsilon_0'}{2.8X'-Y'}\right.$$

$$\left.-\frac{X}{Y^2}\ln\frac{0.7\epsilon_0}{2.8X-Y}+0.25\left(\frac{1}{\epsilon_0'}-\frac{1}{\epsilon_0}\right)\right\} \quad (13)$$

for the hydrogen ion. On substitution of the appropriate values of $\epsilon_0$ and $\epsilon_0'$ we obtain $\Delta G_{H^+}=1.35$ kJ mol$^{-1}$ for the transfer of a mole hydrogen ions from water to 50-percent methanol.

It thus appears that the calculated gain in electrostatic energy due to dissociation of the tris cation is now +0.48 kJ mol$^{-1}$, in even more marked contrast with the observed value of −1.45 kJ mol$^{-1}$. The calculation therefore serves to emphasize that, no matter how doubtful some of the assumptions about the ionic radii may be, the basicity effect in the opposite direction must be of considerable magnitude, in fact about 2 kJ mol$^{-1}$.

Further evidence for the existence of a pronounced increase in solvent basicity when methanol is added to water to make a 50 wt percent mixture is found in the energies of transfer of hydrochloric acid from water to this mixed solvent. The standard emf of the cell with hydrogen and silver-silver chloride electrodes in 50-percent methanol has been found [4] to be 0.19058 V at 25 °C, or 31.76 mV lower than the value in water. Thus the transfer of a mole of hydrogen ions and a mole of chloride ions from water to 50-percent methanol is accompanied by an increase in Gibbs energy of 3.06kJ. The radius of the chloride ion is known [18] to be 1.81 Å. Using the Born model, we calculate that the chloride ion should contribute 1.91 kJ mol$^{-1}$ which, together with 1.24 kJ mol$^{-1}$ for the hydrogen ion, gives 3.15 kJ mol$^{-1}$ for the transfer of hydrochloric acid.

This calculated figure is perhaps not in very serious disagreement with the observed value. Nevertheless, it is derived on the assumption that the macroscopic dielectric constant holds at a distance of 1.81 Å. It is in this region that the Hepler treatment gives results markedly different from those furnished by the Born equation. For example, the electrostatic term for the chloride ion is 3.08 kJ mol$^{-1}$ by the Hepler treatment. This value, together with 1.35 kJ mol$^{-1}$ for the hydrogen ion, gives a total of 4.43 kJ mol$^{-1}$ for the transfer process from electrostatic considerations alone. By comparison with the observed Gibbs energy change (3.06 kJ mol$^{-1}$) it is again seen that the basicity effect must amount to about 1.4 kJ mol$^{-1}$.

Data are available for the solvent effect on the dissociation of acetic acid, but, in view of the very unsymmetrical shape of the acetate anion, it is doubtful that either the Born equation or the Hepler treatment can be usefully applied to data for this acid. However, the second dissociation of phosphoric acid is a more suitable case, because of the higher symmetry of the oxygen atoms surrounding the phosphorus atom.

From density data [19], the partial molal volume of potassium dihydrogen phosphate can be estimated to be 39 ml mol$^{-1}$; a value of 1.5 ml mol$^{-1}$ has been ascribed to the potassium ion [20], leaving 37.5 ml mol$^{-1}$ for the dihydrogen phosphate ion. A mole of spherical ions with radii 2.5 Å would have this partial molal volume and would contribute 1.64 kJ mol$^{-1}$ to the electrostatic energy.

Similar calculations are difficult to make for the bivalent hydrogen phosphate ion ($HPO_4^=$), because the density data for sodium dihydrogen phosphate solutions are fragmentary. The available data, however, suggest a radius of about 2 Å and, therefore, a contribution of 2.49 kJ mol$^{-1}$ to the electrostatic energy. This figure must be quadrupled, however, because of the double charge on this ion. The net effect due to hydrogen ion, $H_2PO_4^-$, and $HPO_4^=$ is 9.7 kJ mol$^{-1}$ compared with the observed value of 7.1 kJ mol$^{-1}$.

It would be unwise to imply that these values of the electrostatic energy calculated with only estimated values of the ionic radii have any exactitude. It is important, however, to note that whenever a reasonable assumption can be made about these ionic radii, the electrostatic contribution is higher by 1 to 3 kJ than the observed energy change. In other words, there is always a term of considerable magnitude for the "basicity effect" that does not figure in the electrostatic treatment.

## 5. Activity Coefficient of Tris Hydrochloride

The success of the extrapolation procedure embodied in eq (1) in this and other similar situations [6] justifies the substitution of the Debye-Hückel formula for the activity-coefficient term in the expression for the dissociation constant of a protonated amine, $BH^+$. Thus for the process

$$BH^+ + SH = B + SH_2^+ \quad (14)$$

one can write [23]

$$\log \gamma_{\pm}' \equiv \log \gamma_{\pm}\left(\frac{a_{SH}}{\gamma_B}\right)^{1/2}=\frac{-A\sqrt{I}}{1+B\mathring{a}\sqrt{I}}+0.5\beta I \quad (15)$$

where $\gamma_{\pm}$ is the mean activity coefficient of the amine hydrochloride.

Straight-line extrapolations such as those shown in figure 1 could not be obtained when "reasonable" values of 3 to 5 Å were used for the ion-size parameter $\mathring{a}$ in eq (1), and the line shown corresponds to $\mathring{a}=0$. A similar anomalous behavior of the activity-coefficient term in aqueous buffer solutions composed of other aliphatic or aromatic amines and their salts has been observed in the course of a number of similar studies. These investigations have dealt with ammonia [23], tris [5], 2-methyl-2-amino-propanediol [24], *t*-butylamine [22], ethanolamine [21], diethanolamine [25],

[6] See, for example, measurements on ethanolamine [21] and *t*-butylamine [22].

triethanolamine [26], aminopyridine [27], and piperidine [28]. The abnormally small or even negative value of $\mathring{a}$ suggests that ion pairs of moderate stability exist in these buffer solutions, and in the study of piperidine it was possible to account for the results with an ion size of 4 Å when a correction was made for ion-pair formation [28].

These observations are surprising in view of the fact that the activity coefficient of aqueous ammonium chloride at 0.1 *m* is not greatly different from that of potassium chloride at the same molality [29]. The isopiestic method by which these activity coefficients were determined is unfortunately not capable of furnishing precise data for activity coefficients much below a molality of 0.1.

One can, however, derive the activity coefficients of ammonium chloride and tris hydrochloride in equimolal buffer solutions [$BH^+(m)$, $B(m)$] from the emf data used to derive $pK$ and from the slopes of the extrapolation lines such as those shown in figure 1 (see eq (15)). The results for the activity coefficients and osmotic coefficients of ammonium chloride and tris hydrochloride are compared in table 4 with the corresponding values for potassium chloride [30]. It is apparent that no great difference exists in dilute aqueous solutions. The value (0.758) found in this way for the mean activity coefficient of tris hydrochloride (0.1 m) in the presence of tris (0.1 *m*) is in good agreement with the value (0.770) found by isopiestic measurements [31] of 0.1 *m* tris hydrochloride without any added tris.

The Hückel equation utilized in eq (1) describes the activity coefficient term by two parameters in two separate terms. The results shown in table 4 mean, therefore, that the variation of the activity coefficient of ammonium chloride (and probably of amine hydrochlorides as well) with ionic strength is partitioned between the two terms in a different manner from that characterizing the behavior of the alkali metal chlorides. The reason for this difference should probably be sought in the different structures of the hydration shells of the two types of cation and in the concomitant effects on the microscopic dielectric constant in the immediate vicinity of the ions.

TABLE 4. *Comparison of the activity coefficients and osmotic coefficients of* KCl, $NH_4Cl$, *and* tris·HCl *in aqueous solutions at 25 °C.*

| $m$ | $\gamma_\pm$ for − | | | $\phi$ for − | | |
|---|---|---|---|---|---|---|
| | KCl | $NH_4Cl$ | Tris·HCl | KCl | $NH_4Cl$ | Tris·HCl |
| 0.005 | 0.928 | 0.925 | 0.925 | 0.977 | 0.975 | 0.975 |
| .01 | .902 | .899 | .898 | .968 | .966 | .966 |
| .02 | .870 | .865 | .864 | .957 | .955 | .954 |
| .05 | .817 | .809 | .808 | .941 | .937 | .936 |
| .07 | .795 | .786 | .785 | .934 | .931 | .930 |
| .1 | .770 | .760 | .758 | .927 | .923 | .923 |

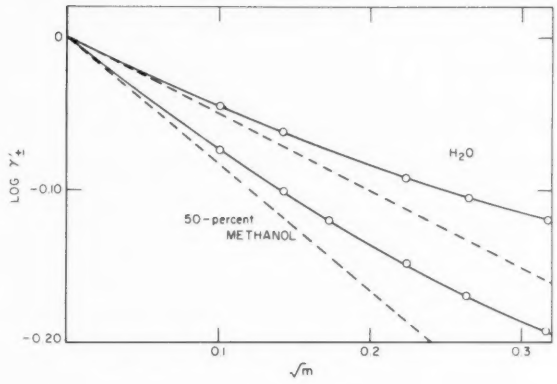


FIGURE 3. *Comparison of log $\gamma'_\pm$ (eq (15)) in the two solvents water and 50-percent methanol.*
The dashed lines are the Debye-Hückel limiting slopes.

The data for tris buffers in 50 wt percent methanol cannot be used to derive the activity coefficients for tris hydrochloride by eq (15), in the absence of information concerning the activities of both tris and the solvent in the methanolic medium. It is of interest, however, to compare the left-hand side of eq (15) for equimolal buffers of tris and its hydrochloride ($m_1 = m_2$) in 50 wt percent methanol with that for the same buffers in water. Such a comparison is shown in figure 3. The standard states in the two solvents differ, so that the activity coefficient becomes unity at $I = 0$ in each case. The Debye-Hückel limiting slopes for the two solvents are indicated by dashed lines, and the general similarity of the curves suggests that there are no great differences in the pattern of behavior in the two media of different compositions. As expected, departures from ideality are greater, at a given ionic strength, in the solvent of lower dielectric constant. Furthermore, the positive deviations from the limiting law are more pronounced in 50-percent methanol than in water.

Although this behavior is a consequence of a larger value of $-\beta$ (eq (15)) in the methanolic solvent, it is impossible at the present time to state with certainty whether it arises from differences in the salt effect on $\gamma_\pm$ or on $(a_{SH}/\gamma_B)$. It is likewise impossible to decide on the basis of this evidence what is the true nature of SH in eq (14), that is, which of the two types of solvent molecules plays the predominant role in the protolysis of $BH^+$. Here again, there seems to be little evidence of a drastic change in the nature of the reaction process, such as would be expected if methanol replaced water to any large extent in the solvation shells of the proton and the acid $BH^+$ or base B.

## 6. References


[1] M. Paabo, R. A. Robinson, and R. G. Bates, J. Am. Chem. Soc. **87,** 415 (1965).
[2] R. G. Bates, Ann. N. Y. Acad. Sci. **92,** 341 (1961).
[3] S. P. Datta, A. K. Grzybowski, and B. A. Wilson, J. Chem. Soc. (London), 792 (1963).
[4] M. Paabo, R. A. Robinson, and R. G. Bates, J. Chem. Eng. Data **9,** 374 (1964).
[5] R. G. Bates and H. B. Hetzer, J. Phys. Chem. **65,** 667 (1961).
[6] R. A. Robinson and R. H. Stokes, Electrolyte Solutions, 2d ed., p. 125 and app. 8.1 (Butterworths Scientific Publications, London, 1959).
[7] R. G. Bates, Determination of *p*H, p. 406 (John Wiley & Sons, Inc., New York, N.Y., 1964).
[8] H. S. Harned and R. A. Robinson, Trans. Faraday Soc. **36,** 973 (1940).
[9] A. L. Bacarella, E. Grunwald, H. P. Marshall, and E. L. Purlee, J. Org. Chem. **20,** 747 (1955).
[10] C. L. deLigny, H. Loriaux, and A. Ruiter, Rec. Trav. Chim. **80,** 727 (1961).
[11] D. Rosenthal, H. B. Hetzer, and R. G. Bates, J. Am. Chem. Soc. **86,** 549 (1964).
[12] E. E. Sager, R. A. Robinson, and R. G. Bates, J. Res. NBS **68A** (Phys. and Chem.) No. 3, 305 (1964).
[13] N. W. Please, Biochem. J. **56,** 196 (1954).
[14] M. Born, Z. Physik **1,** 45, 221 (1920).
[15] R. P. Bell and K. N. Bascombe, Disc. Faraday Soc. **34,** 158 (1957).
[16] L. G. Hepler, Aust. J. Chem. **17,** 587 (1964).
[17] D. M. Ritson and J. B. Hasted, J. Chem. Phys. **16,** 11 (1948).
[18] L. Pauling, The nature of the chemical bond, ch. X (Cornell University Press, Ithaca, N.Y., 1940).
[19] International Critical Tables, Vol. **3,** p. 80 (McGraw-Hill Book Co., Inc., New York, N.Y., 1928).
[20] R. A. Robinson and R. H. Stokes, Trans. Faraday Soc. **53,** 301 (1957).
[21] R. G. Bates and G. D. Pinching, J. Res. NBS **46,** 349 (1951) RP2205.
[22] H. B. Hetzer, R. A. Robinson, and R. G. Bates, J. Phys. Chem. **66,** 2696 (1962).
[23] R. G. Bates and G. D. Pinching, J. Res. NBS **42,** 419 (1949) RP1982.
[24] H. B. Hetzer and R. G. Bates, J. Phys. Chem. **66,** 308 (1962).
[25] V. E. Bower, R. A. Robinson, and R. G. Bates, J. Res. NBS **66A** (Phys. and Chem.), No. 1, 71 (1962).
[26] R. G. Bates and G. F. Allen, J. Res. NBS **64A** (Phys. and Chem.), No. 4, 343 (1960).
[27] R. G. Bates and H. B. Hetzer, J. Res. NBS **64A** (Phys. and Chem.), No. 5, 427 (1960).
[28] R. G. Bates and V. E. Bower, J. Res. NBS **57,** 153 (1956) RP2705.
[29] B. F. Wishaw and R. H. Stokes, Trans. Faraday Soc. **49,** 27 (1953).
[30] W. J. Hornibrook, G. J. Janz, and A. R. Gordon, J. Am. Chem. Soc. **64,** 513 (1942).
[31] R. A. Robinson and V. E. Bower, J. Chem. Eng. Data, in press.


(Paper 69A3–345)

JOURNAL OF RESEARCH of the National Bureau of Standards—A. Physics and Chemistry
Vol. 69A, No. 3, May–June 1965

# Observations of Dislocations and Surface Features in Corundum[1] Crystals by Electron Transmission Microscopy

D. J. Barber and Nancy J. Tighe

(February 12, 1965)

Crystals of corundum, grown by the flame-fusion method, have been chemically thinned and examined by electron transmission microscopy. Some specimens were etch-pitted after thinning, and the relationship between etch pits and dislocations was investigated. Within subgrains there is a close agreement between dislocation and etch pit densities; this agreement breaks down along many boundaries. The etching behavior of crystals containing $Cr_2O_3$, $TiO_2$ and other impurities has been examined. Etch-tunneling along grown-in dislocations is commonly observed in the impurity-doped materials; it is particularly pronounced in ruby. In heat-treated crystals containing $TiO_2$, local differences in solid solubility can lead to the formation of etch hillocks. Thermally etched surfaces have also been characterized, and gas atmospheres are shown to affect the surface topology. Evaporation experiments in the electron microscope are reported.

## 1. Introduction

In recent years, etch-pitting techniques have been used extensively [1, 2][2] to investigate dislocation behavior in inorganic crystals. These methods have been supplemented and made more meaningful by the advent of x-ray topographic and electron microscope studies. The discovery of solid state laser action in certain impurity-doped crystals, and the dependence of laser efficiency on dislocation density and freedom from gross defects, has stimulated interest in etching techniques. Crystals intended for laser applications include molybdates, tungstates, and aluminum oxide containing chromium oxide (ruby).

Currently much effort is directed towards growing crystals with low dislocation densities and the densities are commonly estimated by etch-pitting methods. This paper describes how etch pits and other surface features are related to internal defects in both pure and doped corundum crystals. An examination of dislocation behavior in corundum, using electron transmission microscopy, is published elsewhere [3]. It is hoped that our results will add significantly to the data previously obtained from deformation, x-ray and surface studies.

Wachtman and Maxwell [4], Klassen-Neklyudova [5], and Scheuplein and Gibbs [6] have studied the deformation behavior of single crystal sapphire. It is recognized that two mechanisms exist for plastic deformation by dislocation glide. Near to its melting point, sapphire can slip on the $\{1\bar{2}10\}$ prism planes, in the $< 10\bar{1}0 >$ directions; this will be referred to as prism plane glide. More commonly, slip occurs on the $\{0001\}$ planes in the $< 11\bar{2}0 >$ directions; this is known as basal glide and can occur at temperatures as low as 900 °C.

Chemical etching of sapphire was first investigated by Seebach [7], who used a potassium bisulfate flux to obtain etch-pitted surfaces and terminal dissolution bodies. More recently, Scheuplein and Gibbs [6], and Stephens and Alford [8] have used phosphoric acid and bisulfate fluxes for etching studies. Palmour [9] has studied the appearance of thermally etched surfaces.

## 2. Experimental Procedure

Specimens of white sapphire and ruby were cut from 1/8-in. or 1/10-in. rods, grown by the Verneuil method, and supplied by the Adolf Meller Company. Impurity-doped boules grown at the National Bureau of Standards were also investigated.

The technique used for thinning sections of bulk sapphire has been described by Tighe [10]. Chemical polishing is carried out with hot phosphoric acid, initially by total immersion, and finally with a chemical jet device which affords precise control over the thinning process. By feeding fresh acid into the device, the jet is sustained until a hole appears in the sample; normally the hole is bounded by areas sufficiently thin to transmit electrons. Experiment showed that different temperatures were needed to polish the various low index crystallographic planes. Sections cut parallel to basal or rhombohedral $\{10\bar{1}2\}$ planes polish at 450 to 460 °C; parallel to prism $\{10\bar{1}0\}$, $\{11\bar{2}0\}$ planes and scalenohedral $\{12\bar{3}4\}$ planes, polishing occurs at 500 to 510 °C. Pronounced etching occurred at temperatures ~ 50 °C below the optimum polishing tempera-

[1] Corundum is pure aluminum oxide, $Al_2O_3$, in the stable $\alpha$-phase. The term sapphire is used synonymously in this paper. Crystallographic indices are referred to the structural unit cell, $c/a = 2.730$.

[2] Figures in brackets indicate the literature references at the end of this paper.

ture for each orientation. Light etch-pitting could be achieved, therefore, by lowering the acid temperature as the thinning process neared completion.

The operation of the jet-polishing device depends on the condensation and boiling of orthophosphoric acid. Fresh acid is supplied to sustain operation but, since some acid also recirculates, reaction products build up in solution. If polishing is maintained too long, phosphate deposits can occur on the specimens. Although this can be avoided with care, prolonged boiling in aqua regia is sometimes necessary to obtain absolutely clean surfaces.

Certain specimens, discussed in the text, were chemically etched after normal chemical thinning, using very concentrated hot potassium hydroxide. For other work, described in section 3.4, thinned samples were further thinned by surface evaporation under various gas atmospheres. Specimens were either supported on a resistively heated carbon tape or placed in an alumina boat in a platinum-wound resistance furnace.

Charging of the samples in the electron microscope was avoided by evaporating ~ 100 Å of carbon on to the flat side of each specimen, and placing this side on a copper grid. The microscope, a JEM 6A, was operated at 100 kV.

## 3. Results

### 3.1. Characteristics of Chemical Etch Pits

The general features of etch-pitted sapphire surfaces have been described by Scheuplien and Gibbs [6], and by Alford and Stephens [8]. These workers have measured the dislocation densities for typical material grown by flame-fusion, and found these to be in the range $10^5$–$10^6$/cm$^2$. Many of the dislocations are in subgrain boundary arrays which are approximately perpendicular to the {0001} planes. With phosphoric acid, the etching times must be short in order to retain pits which are small enough for satisfactory electron microscopy. Even then, the pits are somewhat ill-defined, as indicated by figure 1; this shows etch pits on an array of dislocations. The diffraction contrast indicates that the dislocations are nearly perpendicular to the specimen plane, which is {0001}. The array is therefore composed of prism plane dislocations of edge character and is nearly a pure tilt boundary. To estimate the order of the misorientation, a Burgers vector $b_{[10\bar{1}0]} = 8.22$ Å is assumed; the dislocation spacing of $1\mu$ then implies a misorientation of ~ 3 min of arc. Etch pits produced on pure sapphire by phosphoric acid are somewhat less well defined than their counterparts on ruby ($Al_2O_3$ containing a small amount of $Cr_2O_3$). Figure 2 shows two etch pits on the same face of an {0001} specimen of ruby ($Al_2O_3$ + 2 wt percent $Cr_2O_3$ in feed powder for flame fusion), with a short segment of dislocation looping between them. It has been found that the pyramidal pits are rotated by 180° with respect to one another on the opposing faces of a {0001} section. This rotation reflects the essentially trigonal nature of the crystal. The etch pit edges are approximately parallel to $<11\bar{2}0>$ directions. It is significant that the small segment of dislocation is retained in the specimen, between the etch pits. Its presence lends support to other evidence [3] that plastic deformation in sapphire does not occur at normal temperatures. In materials where room temperature deformation occurs, small half-loops may 'pop' out of the surface.

It was sometimes found that etch pits in white sapphire exhibited short 'tails' leading from their apices into the crystal interior. These small tails, on enlargement, are the 'beaks' described by Honess [11], which are a feature of etch pits on many natural mineral crystals. These 'beaks' are now commonly recognized as occurring in etched crystals containing trace impurities. They are undoubtedly due to attack along dislocations decorated with impurity particles, or dislocations with impurity atmospheres. In impurity-doped corundum, the occurrence of etch pits with tails is more pronounced; the tails appear as small tunnels into the crystal. The effect is found in samples containing $ThO_2$, $La_2O_3$, and $Cr_2O_3$; it is particularly pronounced in ruby. The effect is discussed at length in section 3.3. For convenience in illustration, a basal section of pink ruby was chosen to show the appearance of short etch tunnels, or tails, in figure 3. The occurrence of etch pits originating on both the upper and lower crystal surfaces should also be noted.

Etch pits produced in hot caustic potash solution differ markedly from the rounded and somewhat poorly defined ones obtained with phosphoric acid. On the basal plane, 'alkali' pits are almost always hexagonal in shape; they are deep and they undergo less lateral spread than the 'acid' etch pits. It is thus common to find pits passing right through the thicker parts of specimens at points where dislocations were almost normal to the surface. Figure 4 shows a bright field transmission micrograph to illustrate this point. It closely parallels the case of rutile, $TiO_2$, thinned in a sodium hydroxide flux, observed by Barber and Farabaugh [12]. The highest orders of the electron extinction fringes are not visible in the reproduction; on the original photographic plate, however, six contour fringes are visible around the pits. The plate was obtained for two beam diffraction with a $11\bar{2}0$ reflection operating. Values of extinction distance, $t_0$, have been calculated for several lattice reflections and these are given in the appendix. The electron image thus indicates that the specimen thickness at the etch pits was approximately 7560 Å. This agrees quite well with the value deduced from the pattern of optical interference fringes seen in this specimen, 8400 Å. The measurement was made using blue light of wavelength 4600 Å, assuming a value of 1.760 for the refractive index. Taking account of the possible relativistic correction to the electron accelerating potential, mentioned in the appendix, the values agree to within 100 Å.

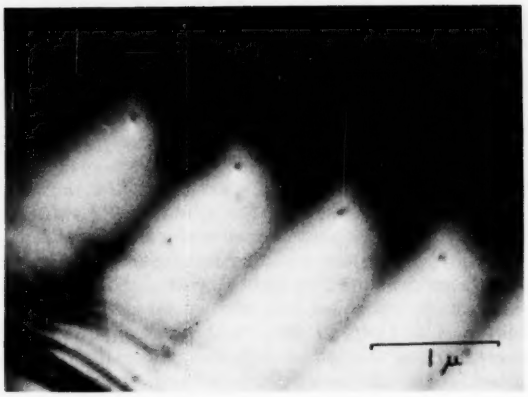


FIGURE 1. *Prism plane dislocations and associated etch pits in a {0001} section.*

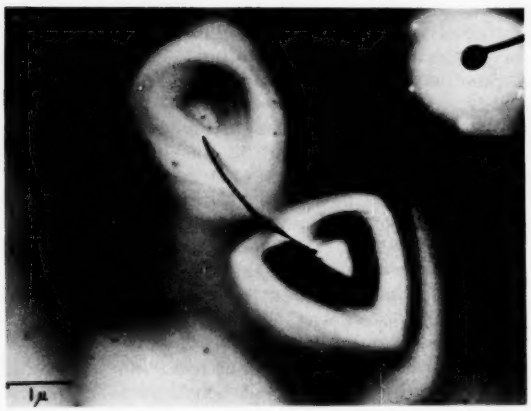


FIGURE 2. *Segment of dislocation looping between two etch pits on the same {0001} surface of a ruby crystal etched in hot phosphoric acid.*

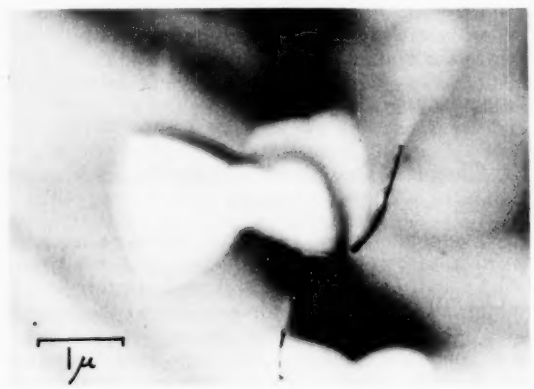


FIGURE 3. *Surface etch pits and short etch tunnels in a sample of ruby; the black lines are dislocations.*

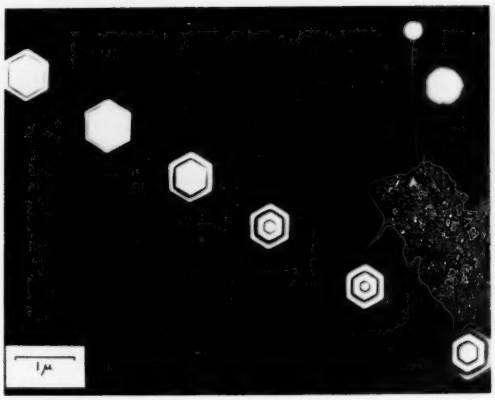


FIGURE 4. *Hexagonal etch pits on a subgrain boundary in a {0001} section etched in hot potassium hydroxide, $11\bar{2}0$ reflection operating.*

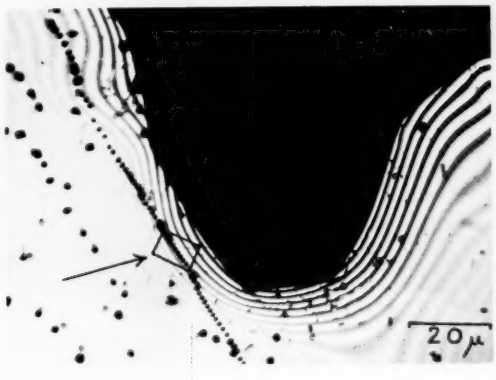


FIGURE 5. *Reflection optical micrograph of general area shown in figure 4, taken with green light.*

The 'alkali' etch pits shown in figure 4 have their edges strictly parallel to $<10\bar{1}0>$ directions. The fact that phosphoric acid etch pits are three-sided, whilst those produced in potassium hydroxide are six-sided, stems from the existence of only three crystallographically equivalent $a$-directions, as compared with six equivalent $<10\bar{1}0>$ directions. Moreover, unlike the pits produced by phosphoric acid, the shape of these pits is strongly affected by the inclination of the dislocations to the surface so that they often exhibit a marked asymmetry. The appearance of the field shown in figure 4, both in the electron microscope and in the optical microscope (figure 5, reflection micrograph, green light) leads to the conclusion that the pits delineate the emergence points of dislocations in a subgrain boundary.

### 3.2. Correspondence Between Etch-Pit Density and Dislocation Density

During this work, the relationship between surface etch pits and internal dislocation arrangements has been examined. As might be expected, etch pits are often found in very thin areas of the crystal where the dislocations have been etched out. Occasionally other pits are found which do not pass through the section, but which could have been associated with a loop or a small crystal void. On the other hand, it is invariably found that, within grains and subgrains, every dislocation which meets the surface is accompanied by an etch pit. At first sight, therefore, there appears to be a good correspondence between dislocation and etch-pit density. In view of our examination of subgrain boundary etching, however, this conclusion must be modified.

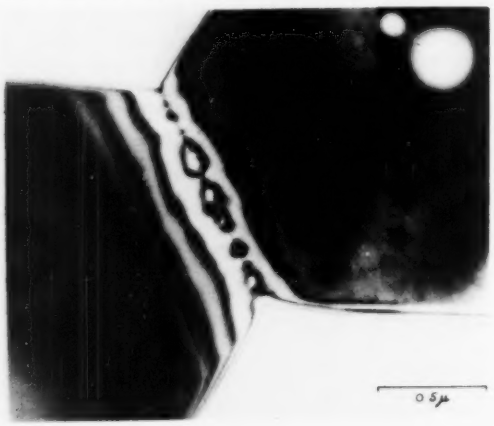


FIGURE 6. *Dislocations perpendicular to the surface in the join between two large hexagonal etch pits in a {0001} section.*

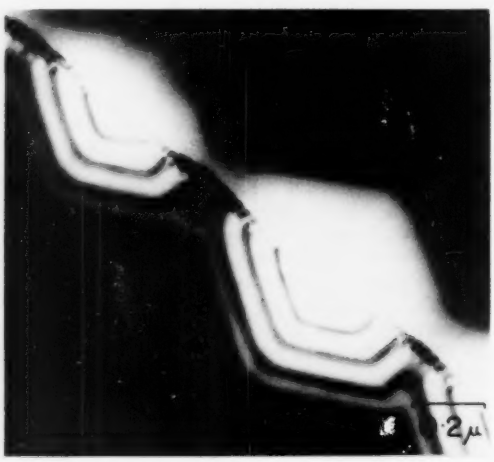


FIGURE 7. *Hexagonal etch pits on a steeply inclined twist boundary in a {0001} section, $30\bar{3}0$ reflection operating.*

For a considerable number of the boundaries investigated it was noted that the etch-pit density along the boundary did not accurately reflect the dislocation spacing. Often the dislocations are grouped within the boundary and there is only one etch pit per dislocation group. The areas between the pits may be slightly grooved but no individual pits are visible in the optical microscope; they are seldom apparent in the electron microscope. The effect is illustrated by figure 6. It shows a number of dislocations, normal to the {0001} specimen surface, in one of the joins between a succession of large etch pits of the type shown in figure 4; the joins had etched to give shallow v-grooves. In figure 6 the slight groove gives rise to several equal thickness fringes. The fringe at the bottom of the groove is discontinuous and follows the array of short dislocation segments. The line of dislocations is parallel to a $<10\bar{1}0>$ direction; thus, they must lie in a $\{1\bar{2}10\}$ plane and they are prism plane dislocations. The lack of correspondence between pits and dislocations along boundaries may be specifically associated with boundaries of mixed character or with composite boundaries formed by the climb of arrays of different ages. Figure 7 shows a twist-type boundary (one set of dislocations showing only weak contrast), with etch pits at regular but infrequent intervals. By tilting the specimen, the extinction fringes could be displaced from one side of the boundary to the other. Locally, the crystal was 17,000 Å thick (calculated from optical interference pattern). A possible explanation may be that the boundary formed as the result of the climb of a twist-net until the latter encountered a preexisting array of dislocations; on etching, only the older dislocations in the composite boundary were attacked.

Although the above examples are boundaries which have been etched in potassium hydroxide, the breakdown in dislocation – etch pit correspondence is not restricted to this etchant. We have noted similar behavior using phosphoric acid as the etchant. Because the etch pits formed with phosphoric acid are poorly defined, however, the result is harder to demonstrate with micrographs. Nonetheless, our observations cast doubt on the validity of etch-pit counts along grain boundaries in sapphire crystals, and this must have an effect on the accuracy of total dislocation density estimates.

### 3.3. Chemical Etching of Impurity-Doped Aluminum Oxide

The etchants used for white sapphire were also effective with ruby, star sapphire ($Al_2O_3 + 0.25$ wt % $TiO_2$), and other impurity-doped materials. The etching effect is more pronounced and the etch pits more clearly defined. The impurity-doped crystals often contain a number of low angle grain boundaries, and these boundaries usually etch into deep grooves. The etching reveals, moreover, that in some materials (e.g., $Al_2O_3 + 0.25$ wt % $GeO_2$) the boundaries often contain many small cavities.

The etching characteristics of two impurity materials are of particular interest:

*Ruby*, $Al_2O_3 + Cr_2O_3$. The etching characteristics have been noted briefly in section 3.1. The production of long etch tunnels is particularly striking. They may penetrate as much as 5 $\mu$ from the crystal surface and narrow to $\sim 500$ Å at the etching tip. Figure 8 is clear evidence that the tunnels follow the paths of dislocations. Well within the crystal, a dislocation is seen continuous with the narrow tunnel.

Recently it has been found that etch tunnels occur in other synthetic nonmetallic crystals. In magnesium fluoride, $MgF_2$, thinned in hot sulfuric acid, Barber [13] has found tunnels as long as $\sim 50\ \mu$, with diameters as small as $\sim 300$ Å. The larger tunnels are now known to result from etching along grown-in dislocations decorated with small magnesium oxide precipitates (which can be seen in the ultramicroscope). The very smallest tunnels are thought to result from etching dislocations with unseen impurity atmospheres. In magnesium fluoride the tunnels have near-constant diameters, whilst in ruby the tunnels are enlarged near the surface. This can be attributed to the different etching rates of the two materials. The tunnels in magnesium fluoride form in a matter of seconds and there is little time for differential lateral spread; in ruby, the tunnels take many minutes to form.

The occurrence of strong etch tunneling in ruby leads us to postulate that, although all compositions of the $Al_2O_3$–$Cr_2O_3$ system are believed to be solid solutions [14], this is not realized in practice. Under the growth conditions for flame fusion crystals, it appears that either impurity atmospheres or microsegregates of chromic oxide occur along grown-in dislocations.

*Star sapphire*, $Al_2O_3 + 0.25$ wt percent $TiO_2$. Crystals were grown and then heat-treated for 24 hr at 1300 °C to produce precipitated or 'star' sapphire. The resulting material contained a high density of precipitate needles, commonly thought to be rutile, $TiO_2$ [15]. Recently Irving [16], using an electron probe analyzer, has found the needles to be an aluminum titanate. The crystals were thinned, under both etching and polishing conditions, and examined. The precipitate needles were not markedly attacked by hot phosphoric acid, and many were retained in even the thinnest regions of the sapphire matrix crystal.

The general appearance of the thinned crystal is shown in the optical micrograph of figure 9. This shows a basal section, the needle axes being parallel to $< 10\bar{1}0 >$ directions. The specimen also exhibited some unexpected features, namely the triangular and bullet-shaped areas visible in the figure. By electron microscopy, the strange appearance of the thinned crystal is easily explained. Parts of a typical precipitated sample, viewed by electron transmission, are shown in figure 10. Figure 10a shows several bullet-shaped lozenges and a number of well defined needles; often needles are seen within the diffuse lozenges. Rounded-off lozenges were often left projecting over the edges of the thinned specimens, as shown in figure 10b, and these were carefully examined. Selected area diffraction, and the appearance of equal thickness fringes, showed that the lozenges and triangles have the corundum structure. Thus they are not actual precipitates, neither are they a direct result of the precipitation process.

Observations on the sharply defined needles suggest that these are the true precipitates. They are usually parallel-sided, but kinked examples are occasionally found. The sharpness of the boundaries defining the precipitate is illustrated in figure 11. This shows the effect of etching a thinned sample in hot concentrated potassium hydroxide ($\sim 250$ °C) for 10 min. Apparently the needle shown emerges on the two crystal surfaces; pits form at both ends and the etchant starts to produce tunnels at *A* and *A'* by attacking the precipitate. Conclusive identification of the needle material by selected area diffraction has not yet been achieved.

FIGURE 8. *Etch pit and etch-tunnel associated with a dislocation in ruby.*

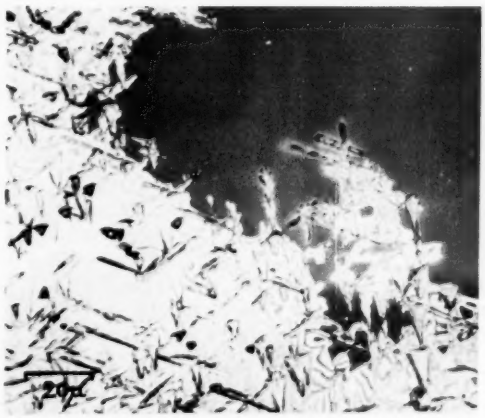

FIGURE 9. *Optical reflection micrograph of thinned heat-treated sample of star sapphire.*

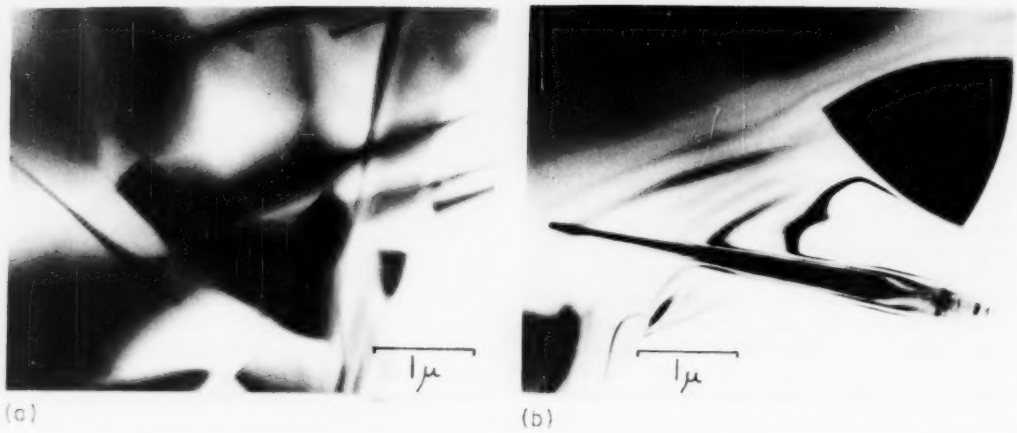


FIGURE 10. *Transmission electron micrographs: (a) showing general appearance of thinned heat-treated sample of star sapphire (b) showing features at edge of thinned crystal.*

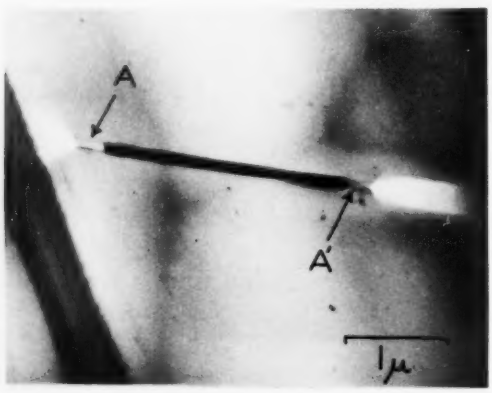


FIGURE 11. *Etch-pits produced at the extremities of a precipitate needle by the action of hot potassium hydroxide.*

The lozenge-shaped and triangular features were judged, from their opacity and from thickness fringes, to be etch hillocks. They result from a local decrease in etching rate around needles. There are three possible explanations for their occurrence: (a) the needles are surrounded by material depleted in solute; (b) the needles are surrounded by material rich in solute; (c) the slowly dissolving needles produce a somewhat insoluble reaction product which adheres to the surrounding surface and thus inhibits attack. Explanation (a) is more plausible than (b) since it is known that impurity-doped material has a higher chemical potential than pure material, and is thus more readily attacked. It is also found, however, that titanium compounds have a tendency to form gummy sols which can markedly affect dissolution characteristics (Barber and Farabaugh [12]); hence explanation (c). These sols are usually in evidence after thinning, however, and there is virtually no evidence for their presence on the star sapphire specimens. It is therefore concluded that the occurrence of the etch hillocks is best explained by the assumption of a solute-depleted zone around the precipitate needles. The occurrence of the bullet-shaped features is easily explained. Any isolated center of solute depletion will decrease the local etching rate and produce a triangular hillock, since this reflects the basic etching habit of the basal plane. After the disturbance is removed, the hillock will slowly shrink and disappear as etching proceeds. If a precipitate needle, and its attendant depleted zone, meets the specimen surface at an acute angle, then the etching center will move with time. Figure 12 shows schematically how the change in the position of a triangular hillock with time will lead to a bullet-shaped hillock.

This adequately explains that elongated hillocks form by the etching action around needles but it does not explain the triangular hillocks themselves. Since there are no needles formed parallel to the <0001> direction, one might suppose that the crystals contain non-needlelike particles of precipitate which produce triangular hillocks. Observations in the optical microscope reveal a number of small triangular precipitates which appear to arise from the contact of two or more embryo needles. Examples are visible

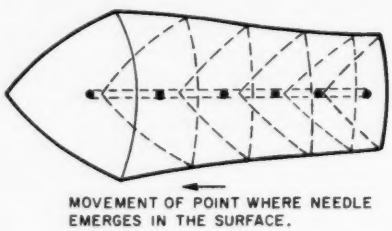


FIGURE 12. *Diagram to show the formation of bullet-shaped hillocks by selective etching around the sites of precipitate needles.*

FIGURE 13. *Optical reflection micrograph taken with oil immersion objective to show small triangular precipitates within crystal of star sapphire.*

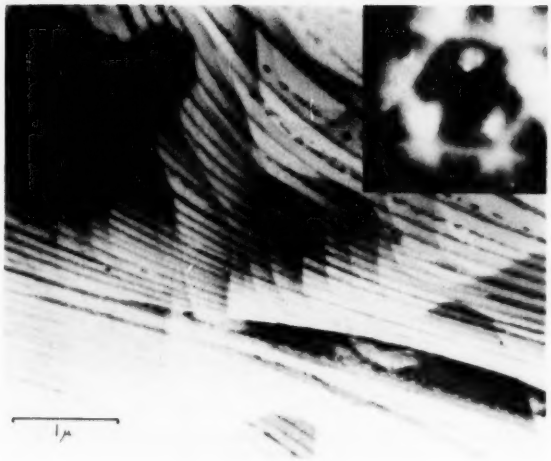


FIGURE 14. *Surface terraces and 'contamination' on a {0001} section thinned by heating in a mixture of argon and nitrogen for 4 min at 1900 °C.*

in figure 13. Further evidence for their occurrence, and incidental confirmation that the hillocks are sapphire, has been obtained by heating and cooling samples in the microscope to dissolve and then re-precipitate needles. These observations, and some relating to dislocations in star sapphire, will be discussed in another publication.

### 3.4. Thermal Etching Observations

To examine the dependence of surface characteristics on internal perfection and surface environment, samples which had been partially thinned by chemical means were subjected to different thermal treatments in gas atmospheres. Figure 14 is a transmission micrograph of a {0001} section after heating in a mixture of argon and nitrogen gases at 1900 °C for 4 min and quenching into liquid nitrogen. A large number of curving surface terraces are to be seen, most of these being decorated by small islands of porous-looking material. From diffraction data, it was concluded that this material is principally $Al_2O_3$, but it may not be the $\alpha$ form. Wachtman and Maxwell [4] found that sapphire rods were covered with a whitish deposit after annealing in argon; from x-ray diffraction data, the deposit was thought to be $\gamma$-alumina. In other specimens held at 1980 °C, terrace decoration was largely absent but large globules were present. There was no evidence to connect these surface features with internal defects. Once again, terraces did not follow crystallographic directions. Occasionally, however, hexagonal plateaus and spirals were found on the surfaces, and whiskers were often found to grow from the centers of the hexagons. Other workers have made similar observations on sapphire platelets grown by the oxidation of aluminum in wet hydrogen.

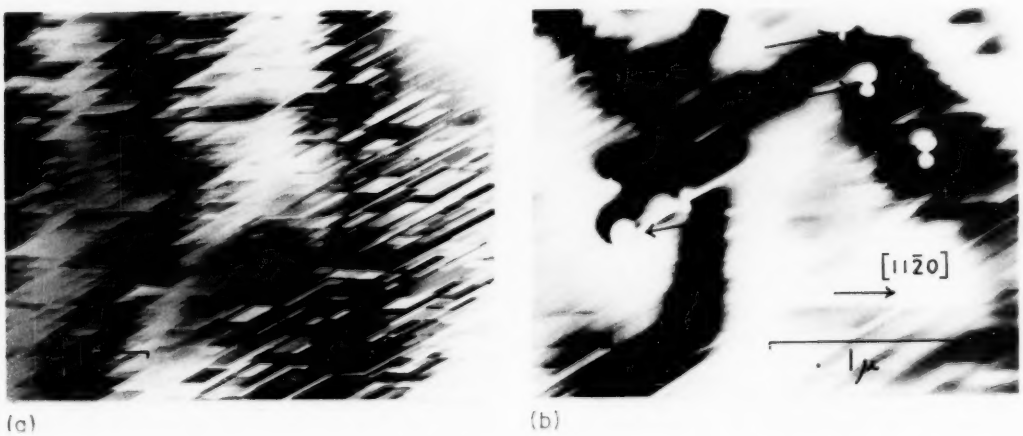


FIGURE 15. *(a) Crystallographic terraces on a {0001} section thinned by heating in dry hydrogen for 90 min at 1450 °C; (b) prism plane dislocations of edge character normal to the surface of a thermally thinned {0001} section.*

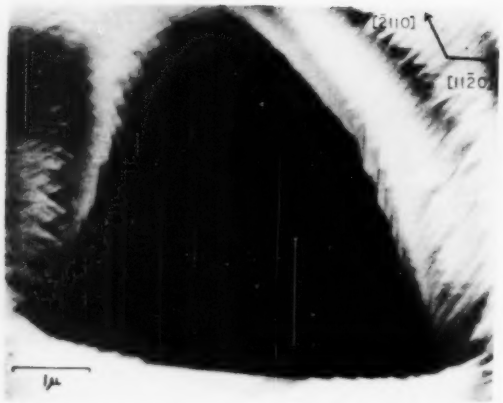


FIGURE 16. *Etch hillock on a basal section thinned by heating in dry hydrogen for 90 min at 1450 °C.*

Diffraction data from the whiskers found in the present work indicates that they were not $\alpha$-aluminum oxide.

In contrast with the foregoing examples, samples thinned in a stream of dry hydrogen for 1½ hr at 1450 °C were free from visible 'contamination,' and moreover, exhibited surface terraces which were strictly parallel to crystallographic directions. Terraces of $<11\bar{2}0>$ and $<10\bar{1}0>$ type are illustrated in figure 15a. The only dislocations observed in these samples were short segments normal to the {0001} planes. These segments did not move during the thinning process, and it must be assumed that they were prism plane dislocations. Examples, some of which are marked by arrows, are seen in figure 15b, near the extinction contours; these dislocations must be edge in character. Compared with similar instances seen in chemically thinned specimens, the dislocations were notable for the marked sharpness of the contrast associated with their strain fields. There were no thermal etch pits associated with the dislocations.

Figure 16 shows a thermal etch pip on another sample thinned in dry hydrogen. The terraces surrounding the hillock show all six possible $<11\bar{2}0>$ and $<10\bar{1}0>$ orientations and the hillock's edges are roughly parallel to $<11\bar{2}0>$ directions. It is believed that these etch pips are centered on spots where surface impurities (for example, small amounts of $AlPO_4$ or $Al(PO_3)_3$ left after chemical thinning) cause the motion of terraces to be impeded and slowed down. Elsewhere the crystal continues to thin. Etch hillocks are not restricted to the surfaces of thermally thinned samples, but can appear after chemical dissolution. Therefore, the hillock shown in figure 16 may have been present in embryo form before evaporation took place, and this treatment served only to enlarge it.

In the course of hot stage work in the microscope, it was possible to observe evaporation *in vacuo* directly. From these experiments, we conclude that the process leads to surface features closely resembling those found after evaporation in hydrogen. Figures 17a and 17b show the same area before and after heating to a temperature of ~1750 °C for a period of about 3 min. In the second figure, many crystallographic terraces are visible and, at the specimen edge, the receding terraces have left frondlike promontories. Traces of the carbon backing film are visible in places; during heating, it shrinks and coarsens. No hillocks were seen on specimens thinned in the microscope. This may be either because the heating period was too short for their formation, or because nucleating particles of contaminant are removed by heating *in vacuo*.

A striking feature of all the thermally thinned samples is the appearance of the associated electron diffraction patterns. The specimens are usually of such a thickness that they produce patterns containing strong Kikuchi lines, which are easily visible against a fairly uniform elastic continuum. Near the primary beam many fine dark deficiency lines are resolved, corresponding to Bragg reflections of very high angle.

FIGURE 17. *Appearance of a {0001} section: (a) before heating in the electron microscope; (b) after heating to ~ 1750 °C for 3 min.*

Such detail is only obtained with the thermally thinned samples. Its significance stems from the fact that the resolution of Kikuchi patterns is normally limited by the lattice strain in regions of the diffracting surface from which the beam emerges. Sample bending as little as 1 part in $10^4$ can destroy detail. Our observations suggest two possibilities: (a) chemically thinned samples are covered with a distorting layer of contaminant, which is absent on thermally thinned samples; (b) thermally thinned samples are more strain-free than normal samples. Of these, we favor explanation (b). The excellent contrast around prism plane dislocations in thermally thinned specimens also suggests that the only internal strains are those localized around defects. It is quite reasonable to expect that unannealed chemically thinned sections, produced from a massive boule or rod, will exhibit some internal strain.

## 4. Conclusions

The nature of etch features on the surfaces of single crystal sapphire have been demonstrated by optical and electron transmission microscopy. Chemical etch pits are found to reveal the symmetry of the etched surface, as anticipated. On the basal plane, pits produced by the action of hot phosphoric acid are three-sided, with the etch-pit edges parallel to $<11\bar{2}0>$ directions. Hexagonal etch pits produced by hot potassium hydroxide are more distinct than the three-sided pits and their edges are parallel to $<10\bar{1}0>$ directions. Within crystal subgrains there is a good correspondence between etch pits and dislocations emerging at the surface. Along subgrain boundaries, the correspondence often breaks down.

Etch tunneling down dislocation lines is sometimes seen in nominally pure sapphire. It is a stiking feature of etched crystals of impurity-doped sapphire, particularly ruby. The tunneling effect is attributed to the presence of impurity atmospheres or even microsegregation at grown-in dislocations.

The chemical dissolution of star sapphire ($Al_2O_3 + TiO_2$) has been studied, and optical observations have been compared with those made in the electron microscope. From these observations it is concluded that the precipitates are surrounded by a zone depleted in solute. On dissolution of the crystal surfaces, the depleted zones lead to the production of etch hillocks surrounding precipitate sites. The hillocks have triangular and lozenge-shaped forms. Triangular hillocks are found to result from dissolution around small precipitates with a triangular profile, while the elongated forms are associated with needles.

The characteristics of crystal surfaces etched in certain gas atmospheres have been studied to see if there is any correlation between internal and surface defects. Under the experimental conditions realized, no correlation is found, although it might be expected for very slow rates of attack. Nitrogen and argon atmospheres (of tank purity) produce 'contaminated' surfaces, exhibiting curving terraces having no relation to the crystallography of the surface. Samples etched in dry hydrogen, or in the vacuum of the electron microscope, show similar features and they are relatively clean. Moreover, they are covered with well defined crystallographic terraces; most of these are parallel to $<11\bar{2}0>$ directions, but there are also many examples parallel to $<10\bar{1}0>$ directions. From comparison of Kikuchi line patterns for chemically and for thermally thinned samples, it is concluded that the heat-treatment effectively removes long-range internal strains. This is further demonstrated by the clarity with which the strain fields are revealed around prism plane dislocations.

Our results confirm that electron transmission microscopy is a powerful method of correlating internal and surface features. Even with a relatively inert material like sapphire, treatments can be devised to etch defect structures selectively and the early stages of attack are easily discerned in the electron microscope.

---

Our thanks are due to W. S. Brower for supplying boules of impurity-doped sapphire, and to A. C. Bonanno for careful preparation of the micrographs. The work was partially supported by the Advanced Research Projects Agency.

## 5. Appendix. Extinction Distances in $\alpha$–$Al_2O_3$

The dynamical theory of electron diffraction, developed in recent years by Heidenreich [17], Howie and Whelan [18], and others has had many successes in explaining the diffraction contrast seen in transmission specimens. In particular, the theory accounts for the equal thickness fringes seen in wedge-shaped crystals when only one set of lattice planes is diffracting. When the incident beam strikes the crystal at almost a Bragg angle, the transmitted and diffracted beam intensities vary with depth of crystal penetration, $z$, as

$$I = \frac{\sin^2 \pi z \, (t_g^{-2} + s^2)^{1/2}}{(t_g^{-2} + s^2)}$$

where $t_g$ is called the extinction distance and $s$ is the distance of the reciprocal lattice points, defined by $\mathbf{g}$, from the surface of the Ewald sphere.

The electron image from a wedge-shaped crystal therefore exhibits extinction contours at intervals corresponding to thickness increments of $(t_g^{-2} + s^2)$. The increment is a maximum $t_0$ when the specimen is exactly oriented at the Bragg angle ($s = 0$).

Unlike some metals, aluminum oxide crystals lack well-characterized defects from which, with the aid of diffraction data, extinction distances could be estimated for various diffracting planes. Moreover, direct comparison of optical and electron interference fringes, used by Frankl [19] for silicon, is less practical for aluminum oxide on account of its refractive index.

Values of $t_0$ have been calculated, therefore, using an expression of Whelan and Hirsch [20]:

$$t_0 = \frac{\lambda E}{V_g}$$

where $E$ is the accelerating potential of the electron beam, $\lambda$ is the wavelength and $V_g$ is the Fourier coefficient of lattice potential, expressed in volts, for the diffracting planes. The Fourier coefficient is a measure of elastic scattering from the partially screened nuclear fields at the atomic centers in the lattice; it can be calculated, therefore, by a correct summation of the electron scattering factors for the individual atoms in the unit cell. With appropriate substitutions, the value of $V_g$ is found to be

$$V_g = \frac{600\ \mathrm{h}^2 d_g^2 \sin^2\theta}{\pi m e V \lambda^2} \Sigma f_j \exp\left(-2\pi i \mathbf{g}\cdot\mathbf{r}_j\right)$$

where $h$ is Planck's constant, $m$ the mass of the electron, $e$ the electronic charge, $V$ the volume of the unit cell, $d_g$ the interplanar spacing associated with the Bragg reflection $\mathbf{g}$ at Bragg angle $\theta$, and $f_j$ the electron scattering factor for the $j$th atom at $\mathbf{r}_j$ in the unit cell. The summation $\Sigma f_j \exp(-2\pi i \mathbf{g}\cdot\mathbf{r}_j)$ is the structure factor for electrons, $F$. The latter, and hence $V_g$, was simply calculated for the rhombohedral cell using the atomic coordinates given by Kronberg [21] and the electron scattering amplitudes, $f_j$, calculated by Ibers as given by Thomas [22]. The latter were obtained using Hartree-Fock screening models for the aluminum and oxygen atoms.

Extinction distances thus obtained, corrected for the relativistic electron momentum are given in the following table:

| Rhombohedral indices | $10\bar{1}$ | $2\bar{1}\bar{1}$ | 111 | 222 |
|---|---|---|---|---|
| Hexagonal indices | $11\bar{2}0$ | $30\bar{3}0$ | 0003 | 0006 |
| Extinction distance, $t_0$ (angstroms) | 1260 | 815 | $\infty$ | 650 |

These values are probably about 10 percent low, owing to a further relativistic correction which has been omitted. Fowler and Marton [23] have recently pointed out that the accelerating potential for electrons, $E$, should be replaced by the 'effective relativistic potential difference' $E^*$, where $E^* = E + \frac{e}{2m_0c^2}E^2$. This correction amounts to $\sim +10$ percent for 100 kV electrons; previously it has been neglected in calculations of extinction distances.

## 6. References


[1] W. G. Johnston, Progr. Ceramic Sci. **2,** 1 (1961).
[2] J. D. Livingston, Acta Met. **10,** 229 (1962).
[3] D. J. Barber and N. J. Tighe, Phil. Mag. **11,** 495 (1965).
[4] J. B. Wachtman and L. H. Maxwell, J. Am. Ceram. Soc. **37,** 291 (1954); **40,** 377 (1957).
[5] M. V. Klassen-Neklyudova, J. Tech. Phys. (U.S.S.R.) **12,** 519, 535 (1942).
[6] R. Scheuplein and P. Gibbs, J. Am. Ceram. Soc. **43,** 458 (1960); **45,** 439 (1962).
[7] M. Seebach, Neues Jahrb. Mineral Geol. **A54,** 420 (1926).
[8] D. L. Stephens and W. J. Alford, J. Am. Ceram. Soc. **47,** 81 (1964).
[9] H. Palmour, J. J. DuPlessis and W. W. Kriegel, J. Am. Ceram. Soc. **44,** 400 (1961).
[10] N. J. Tighe, Rev. Sci. Inst. **35,** 520 (1964).
[11] A. P. Honess, The Nature, Origin and Interpretation of Etch Figures on Crystals (John Wiley & Sons, New York, N.Y., 1927).
[12] D. J. Barber and E. N. Farabaugh, J. Appl. Phys. (in press).
[13] D. J. Barber, J. Appl. Phys. **35,** 3084 (1964); ibid. (in press).
[14] E. M. Levin, H. F. McMurdie and C. R. Robbins, Phase diagrams for ceramists, p. 121 (American Ceramic Society Inc., Columbus, Ohio, 1964).
[15] E. J. Gubelin, Inclusions as a means of gemstone identification, (Gemological Institute of America, 1953).
[16] S. M. Irving, private communication.
[17] R. D. Heidenreich, J. Appl. Phys. **20,** 993 (1943).
[18] A. Howie and M. J. Whelan, Proc. Roy. Soc. (London) **A263,** 217 (1961).
[19] D. R. Frankl, J. Appl. Phys. **35,** 217 (1964).
[20] M. J. Whelan and P. B. Hirsch, Phil. Mag. **2,** 1303 (1957).
[21] M. L. Kronberg, Acta Met. **5,** 507 (1957).
[22] G. Thomas, Transmission Microscopy of Metals, p. 290 (John Wiley & Sons, Inc., New York, N.Y., 1962).
[23] H. A. Fowler and L. Marton, J. Appl. Phys. (in press).


(Paper 69A3-346)

JOURNAL OF RESEARCH of the National Bureau of Standards—A. Physics and Chemistry
Vol. 69A, No. 3, May–June 1965

# Low-Frequency Dielectric Properties of Liquid Boric Oxide

**Kurt H. Stern**

(February 19, 1965)

The dielectric constant and loss of glassy $B_2O_3$ have been measured from 500 to 800 °C over the frequency range 1 to 50 kHz. The material behaves essentially like a nonpolar polymer; no relaxation phenomena could be identified. Over the entire frequency and temperature range $\epsilon'$ lies between 3.1 and 3.2. Losses increase with increasing temperature and decreasing frequency and appear to be due to ionic impurities. The activation energy for conductance is 77.8 kJ (18.6 kcal), independent of frequency.

## 1. Introduction

Boric oxide ($B_2O_3$) is one of the two most extensively studied inorganic glass-forming oxides, the other being $SiO_2$. Many of its physical properties have been measured as a function of temperature [1][1] but the determination of accurate values has been hampered by the great difficulty of preparing the pure, especially water-free, compound.

One aspect of these studies is the elucidation of the vitreous structure, which has even been described in terms of $B_4O_6$ molecules [2], but now is generally considered to be a disordered, three-dimensional network held together by B—O bonds which rupture increasingly as the temperature is raised. Consequently the viscosity decreases, and even at relatively moderate temperatures (800–1000 °C) the material flows like a viscous liquid.

Another interesting property of $B_2O_3$ is its solvent power for a large number of inorganic oxides [3] and salts [4]. It is this latter aspect, together with the low viscosity, which makes it possible—at least in principle—to study dilute electrolyte solutions at high temperatures. Up to now the only molecular solvent used in this temperature range has been high-pressure, supercritical water [5].

In order to interpret conductance data by the classical Debye-Hückel-Onsager methods several solvent properties must be known, principally viscosity and dielectric constant. The former has been measured over a wide temperature range [6], but low-frequency dielectric data are largely lacking. The dielectric constant $\epsilon'$ of a sample of unspecified purity was reported to be [7] 3.2, independent of temperature from 20 to 400 °C; preliminary data by Kruh and Stern [4] between 25 and 570 °C on a not-entirely-waterfree sample showed a marked temperature dependence which is, however, due to an error in calculation. It thus seemed of interest to determine the dielectric constant from a temperature at which liquid flow begins to as high a temperature as our apparatus would permit. This upper cutoff point is largely dependent on the losses which increase markedly with increasing temperature and decreasing frequency. In the present work we report data from 500 to 800 °C.

[1] Figures in brackets indicate the literature references at the end of this paper.

## 2. Experimental Part

### 2.1. Preparation of Anhydrous $B_2O_3$

Baker Analyzed Reagent $H_3BO_3$ was dehydrated in a cylindrical platinum crucible of 170 ml capacity by increasing the temperature to 800 °C over several weeks. After this preliminary dehydration the crucible was cooled and transferred to a long mullite tube. The tube was positioned upright in the furnace with the crucible at its bottom. A rubber stopper with a long quartz tube through it was placed in the tube. When the crucible had reached 1200 °C dry $BCl_3$ gas was passed through the quartz tube and a platinum tube fastened at its lower end which projected into the melt. $BCl_3$ was bubbled through the $B_2O_3$ until HCl evolution had ceased. It was then replaced by dry helium. The melt was finally cooled to room temperature and stored in a desiccator. This procedure removes water completely [8]. A semiquantitative spectro-chemical analysis of the $B_2O_3$ showed that, except for sodium, ionic impurities constituted approximately 0.01 percent.

### 2.2. Cell Design and Construction

In order to eliminate difficulties associated with lead capacitance a three-terminal method was used. The cell was of the immersion type, the entire cell assembly fitting onto the crucible containing the melt (fig. 1).

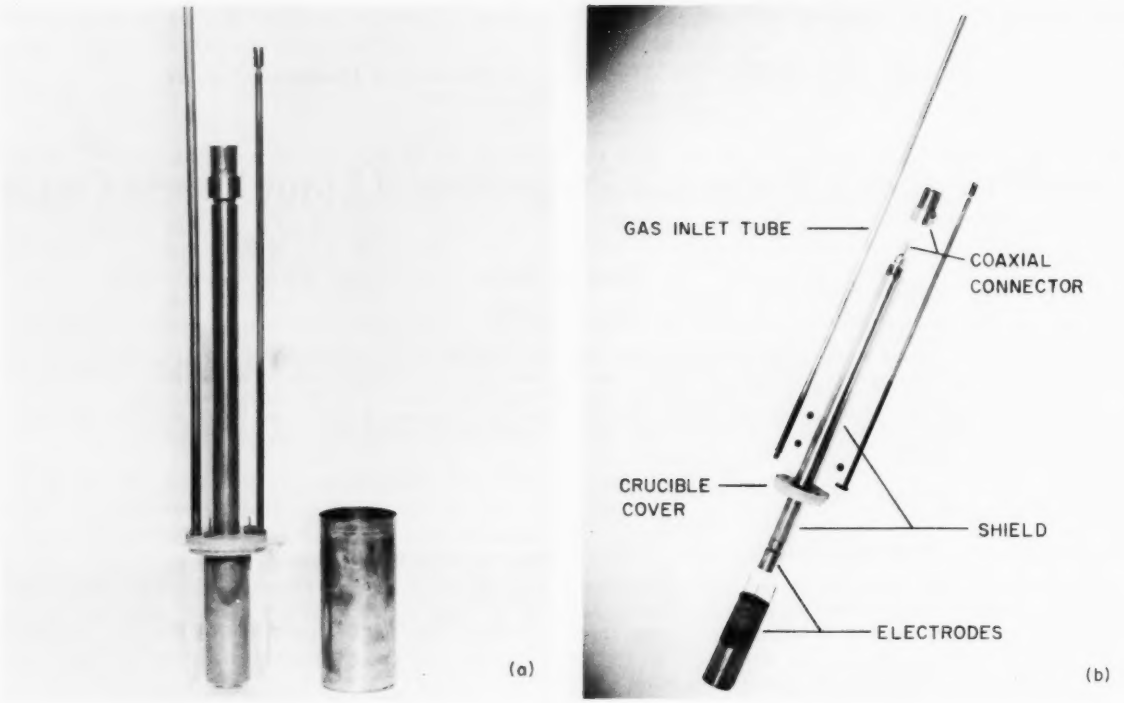


FIGURE 1. *Dielectric Cell.*

(a) Assembled Cell. The glass beaker shows the cell in upright position. Actual Pt beaker used on right.
(b) Exploded view.

All metallic parts were made of heavy-walled nickel tubes and rods; all insulating washers, spacers, etc., were machined from lava stone and fired at a high temperature to remove volatile impurities and to fix final dimensions. This cell is easily assembled and taken apart, its capacitance remaining fixed to within $\pm 0.005$ pF. A photograph of the assembled cell is shown in figure 1a and a partly exploded view in figure 1b. Its capacitance was approximately 2.5 pF.

### 2.3. Dielectric Measurements

The platinum crucible containing the dehydrated $B_2O_3$ was transferred to a well-regulated furnace and heated under dry helium until the glass became sufficiently soft to permit immersion of the cell assembly described previously. A slow flow of dry helium was maintained over the melt surface. The temperature was measured with a calibrated platinum-platinum/rhodium thermocouple whose hot junction was immersed directly in the glass. Dielectric constant and loss were measured with a General Radio Type 1615–A capacitance bridge at each of several constant temperatures between 500 and 900 °C. In each measurement the frequency was varied from as low as the bridge could be balanced to a maximum of 50 kHz. With increasing temperature low-frequency dielectric losses increased so that at the higher temperatures only measurements at the higher frequencies were possible.

The cell was calibrated empty over the same temperature and frequency range as used in the measurements. Above 2 kHz the capacitance was virtually independent of frequency, but it increased noticeably with temperature; e.g., from 2.533 pF at 511 °C to 2.552 pF at 785 °C.

## 3. Results

### 3.1. Treatment of Experimental Data

The quantities measured experimentally are $C_0$ = capacitance of the empty cell, $C_s$ = series capacitance of the filled cell, $D$ = dissipation factor, and frequency $f$. From these, the real and imaginary parts of the complex dielectric constant

$$\epsilon^* = \epsilon' - i\epsilon'' \tag{1}$$

are calculated from the well-known relations

$$C_p = \frac{C_s}{1 + D^2} \tag{2}$$

$$\epsilon' = C_p/C_0 \tag{3}$$

and the conductance

$$G = D\omega C_p \tag{4}$$

where

$$\omega = 2\pi f \tag{5}$$

$C_s$ could usually be determined to six significant figures and $D$ to four, but at high $D$ values the sensitivity of the bridge decreased. Some scatter of unknown origin reduced the precision of $\epsilon$ considerably and therefore dielectric constants are only reported graphically (fig. 3).

Although the cell cannot be calibrated as a conductance cell (the resistance varies with the depth of immersion of the electrodes in the calibrating solution) the specific conductance $\sigma$ can be calculated from the dielectric measurements as follows:

By definition

$$G = \sigma(A/1) \tag{6}$$

where $A$ and 1 represent the area and distance of separation of the electrodes. From eq (3)

$$C_p = \epsilon' C_0 = \epsilon' \epsilon_0 (A/1) \tag{7}$$

where $\epsilon_0$, the permittivity of free space, is $8.85 \times 10^{-14}$ F cm$^{-1}$. From (4), (6) and (7)

$$\sigma = D\omega\epsilon'\epsilon_0 \tag{8}$$

so that $(A/1)$ does not have to be known explicitly.

### 3.2. Dielectric and Conductance Data

A plot of $\epsilon'$ as a function of temperature at various fixed frequencies is shown in figure 2. The large increase of $\epsilon'$ with temperature at 1 and 2 kHz is most likely caused by polarization effects at the electrodes due to ionic impurities in the glass. The decrease of $\epsilon'$ at 50 kHz above 700 °C probably reflects failure of the bridge which becomes increasingly inaccurate above 20 kHz. Although the data scatter considerably, all values of $\epsilon'$ from 5 to 20 kHz lie between 3.12 and 3.20 and exhibit a slight positive temperature coefficient. In figure 3 plots of $\epsilon'$ versus log $f$ at several temperatures are shown.

The temperature dependence of $D$ is shown explicitly for several different frequencies in figure 4. In every case log $D$ is a linear function of temperature, the temperature coefficient $d$ log $D/dT$ increasing very slightly with decreasing frequency. This behavior was also observed by Strutt [9] for a number of $SiO_2-Na_2O$ glasses in which the losses are primarily conductive. If ionic conduction is the primary source of loss in $B_2O_3$, ln $\sigma$ would be expected to be a linear function of $1/T$, independent of frequency. That this is indeed the case is shown in figure 5. From the slope and the relation

$$\sigma = Ae^{-E^*/RT} \tag{9}$$

the activation energy $E^*$ was found to be 77.8 kJ (18.6 kcal) independent of frequency, which is considerbly lower than the 26 kcal/mole found by Mackenzie [6] for the temperature range 850 to 1350 °C. An increase in $E^*$ with temperature is not reasonable. It is possible, however, that the principal impurities giving rise to the conductance are different in the two cases. Ionization of $B_2O_3$ at this low temperature can be ruled out [6].

If the higher activation energy is associated with ionized water transport some special mechanism would have to be postulated which hinders these small ions compared to, for example, sodium. In figure 6 the frequency dependence of $\omega D\epsilon' = \sigma/\epsilon_0$ is shown for the lowest three temperatures. The slight increase with increasing frequency suggests an increased freedom of movement of the ions about their equilibrium positions (short term transient response).

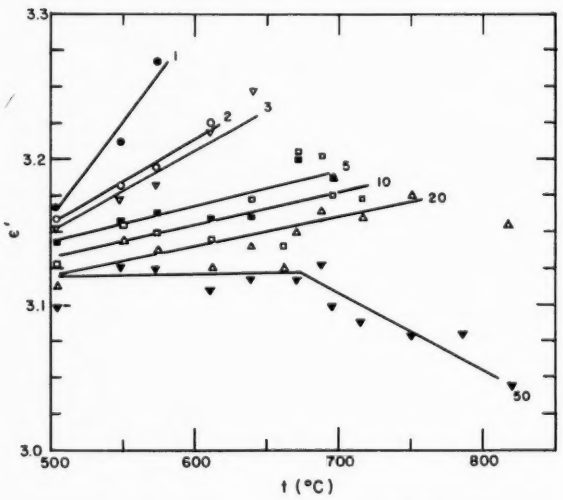


FIGURE 2. $\epsilon'$ *as a function of temperature.*

Frequencies (kHz) to the right of respective curves.

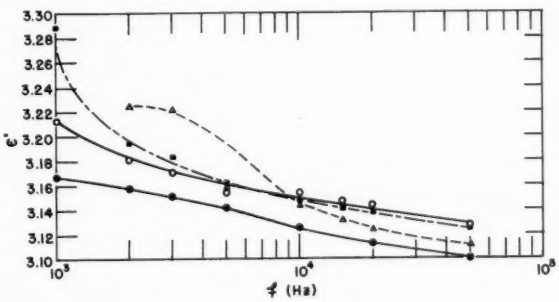


FIGURE 3. $\epsilon'$ *as a function of frequency.*

—●—502.8°, —○—546.5°, ---■---573.8°, --△--611.2°.



766-033 O - 65 - 6

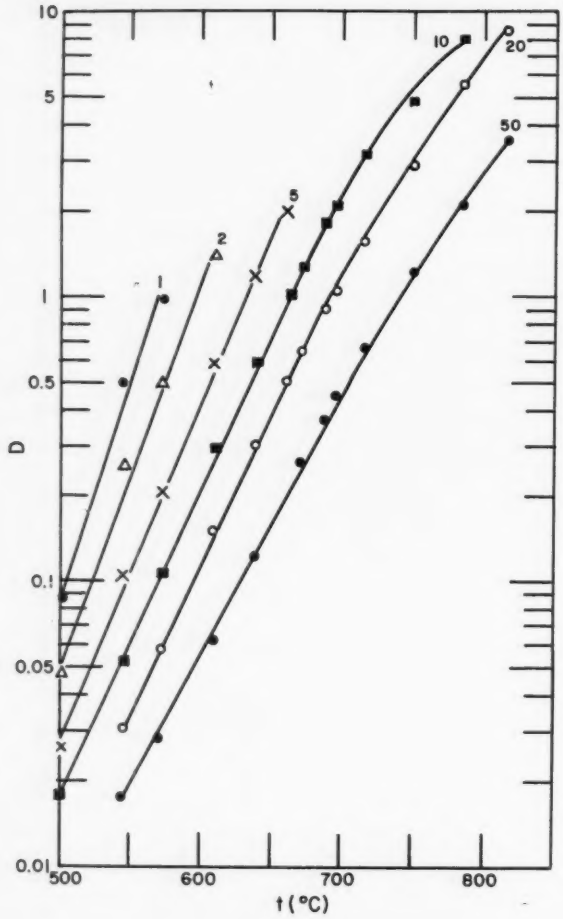


FIGURE 4. D *as a function of temperature.*

Frequencies (kHz) shown at top of respective curves.

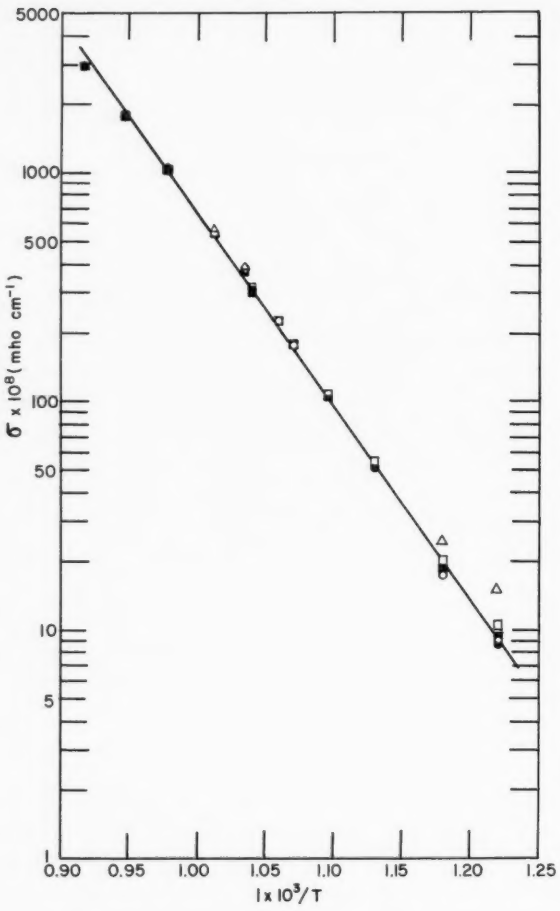


FIGURE 5. *Specific conductivity* $\sigma$ *as a function of* 1/T.

Frequencies in kHz: ● 1, ○ 5, ■ 10, □ 20, △ 50.

## 4. Discussion

The dielectric behavior of $B_2O_3$ found in this study is consistent with previous work on this material. The three-dimensional random network behaves essentially like a nonpolar liquid. There may be a very small dipole relaxation which could arise from a nonstoichiometric distribution of boron and oxygen atoms in some of the clusters which are free to move at elevated temperatures.

The loss appears to be entirely conductive and due to impurities, such as sodium ions, in the melt. We have, however, no good explanation for the difference of the activation energy of conductance between this work and Mackenzie's.

If the behavior of salts dissolved in $B_2O_3$ depends primarily on the dielectric constant of the medium, as is the case with ordinary molecular solvents, extensive ionic association into ion pairs and higher aggregates at even quite low concentrations would be expected. In addition $\Lambda_0$, the equivalent conductance at infinite dilution, should be low because of the high solvent viscosity and can be estimated from the Walden product $\Lambda_0\eta$ obtained for a particular electrolyte in other solvents.

For electrolytes with high-charge density anions which compete with oxygen for boron bonds [4] it is quite possible that only cations would conduct charge. It should be possible to distinguish this possibility by determining $\Lambda_0$ for a number of salts having the same cation. By the same method, the question of oxide ion mobility in the case of dissolved oxides could also be answered.

In any case, it is clear that for such studies the solvent must be dry since at elevated temperatures small amounts of salt can easily hydrolyze in residual water, e.g., $2NaCl + H_2O = 2HCl + Na_2O$.

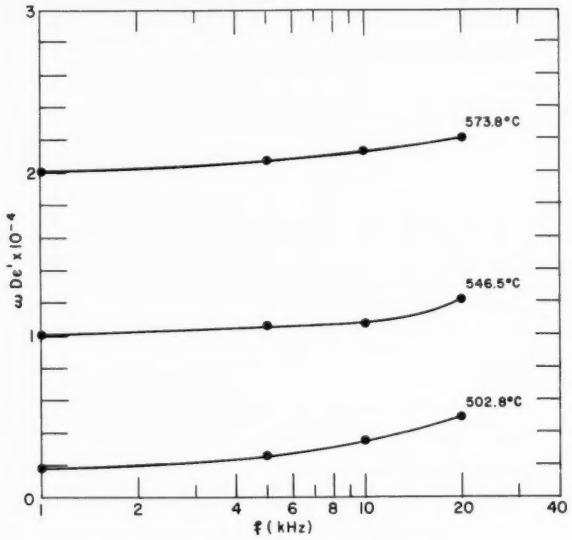


FIGURE 6. $\omega D\epsilon' = \sigma/\epsilon_0$ *as a function of frequency.*

Temperature to the right of respective curves.

A number of authors have presented conflicting evidence as to whether alkali halides react with $B_2O_3$ directly to produce free $Cl_2$ and sodium borate [1]. It is conceivable that these early workers were actually noting the hydrolysis in insufficiently dried $B_2O_3$, but this possibility needs further investigation.

I am greatly indebted for much helpful advise concerning dielectric measurement and cell design to N. L. Brown, A. H. Scott, and W. P. Harris; and to M. Broadhurst for enlightening discussions on dielectric theory.

## 5. References

[1] *cf.* Gmelin, Handbook of Inorganic Chemistry, 8th ed., **13** supplement, pp. 125–136, Weinheim, 1954.
[2] K. Fajans and S. W. Barber, J. Am. Chem. Soc. **74,** 2761(1952).
[3] M. Foex, Ann. Chim. [11], 359(1939).
[4] R. F. Kruh and K. H. Stern, J. Am. Chem. Soc. **78,** 278(1956).
[5] *e.g.*, A. S. Quist, E. U. Franck, H. R. Jolley, W. L. Marshall, J. Phys. Chem. **67,** 2453(1963).
[6] J. D. Mackenzie, J. Phys. Chem. **63,** 1875(1959).
[7] N. P. Begorodicki and V. N. Malysev, Zhurn. techn. Fiz. (USSR) **5,** 612(1939).
[8] A. J. Harrison, J. Am. Ceram. Soc. **30,** 362(1947).
[9] M. J. O. Strutt, Arch. f. Elektrotechnik **25,** 715(1931).

(Paper 69A3–347)

JOURNAL OF RESEARCH of the National Bureau of Standards—A. Physics and Chemistry
Vol. 69A, No. 3, May–June 1965

# Mass Spectrometric Study of the Effects of Nitric Oxide and Other Additives on "Purified" Active Nitrogen

John T. Herron

(Received August 10, 1964)

A mass spectrometric study has been made of the interaction of NO and other additives with "purified" active nitrogen. The observed increase in N atom partial pressure when NO is added is interpreted in terms of a change in the accommodation coefficient of the N atoms.

The metastable $N_2$ species which can be detected with the mass spectrometer can be deactivated with $N_2O$ or $NH_3$, but not with NO, $O_2$, or $NF_3$.

## 1. Introduction

Young and Sharpless [1][1] have stated that the excited species present in active nitrogen, such as those contributing to the pink nitrogen afterglow [2], can destroy nitric oxide and hence lead to a false value for the atom concentration as measured by the NO titration technique [3]. Young, Sharpless, and Stringham [4] have given some detailed results on the effect of adding a variety of compounds both before and after passing nitrogen through a microwave discharge. The magnitude of the effects observed seems to depend on the initial purity of the nitrogen. In untreated "prepurified" grade nitrogen they are not significant.

The recent emphasis on high purity gases, particularly in the study of atomic recombination reactions makes it mandatory that we have a clear understanding of the nature of the interaction of NO and other additives with highly purified active nitrogen.

I wish to report here a mass spectrometric study of the interaction of NO and other additives with active nitrogen.

## 2. Experimental Procedures

The instrument and associated reactors have been described elsewhere [5].

Matheson "prepurified" grade nitrogen was taken at 19.7 psi through copper lines, a glass flowmeter (attached with short Tygon sleeves), and a metal needle valve into the low pressure flow system. On the high pressure side the gas could be passed through a copper coil held at −78 °C, while on the low pressure side it could be passed through a glass coil held at −196 °C before entering the discharge zone (2450 MH electrodeless discharge). The total pressure was varied from 2 to 6 torr [6] at linear flow rates of about 1000 cm/sec.

Reactant gases could be added just before the discharge or at various points after the discharge. The sampling orifice of the mass spectrometer was downstream of the reactant inlets.

The partial pressure of the additives was followed in the usual manner using 58 eV electrons. The relative partial pressures of atomic N and O were measured at reduced electron energies (25 eV nominal) as previously described [5, 7]. The relative partial pressure of metastable $N_2$ was followed at 17 eV (nominal).

## 3. Effects of Additives on the N Atom Partial Pressure

The method of purification used here was not as elaborate as that used in references [1] and [4], and in general the effects observed were proportionally less. Nonetheless, the same general phenomena were observed; the addition of NO, $O_2$, $NH_3$, $NF_3$, or $SF_6$ in varying proportions before the discharge led to about a threefold increase in the partial pressure of the N atoms detected by the mass spectrometer. If added after the discharge, the additives, with the exception of $SF_6$ which had little or no effect, caused about a twofold increase in the N atom partial pressure.

The lower two curves of figure 1 show the relative partial pressures of N and O atoms (in terms of ion current) as a function of the initial partial pressure of NO added after the discharge. It is noteworthy that O atoms are detectable over the entire range.

[1] Figures in brackets indicate the literature references at the end of this paper.

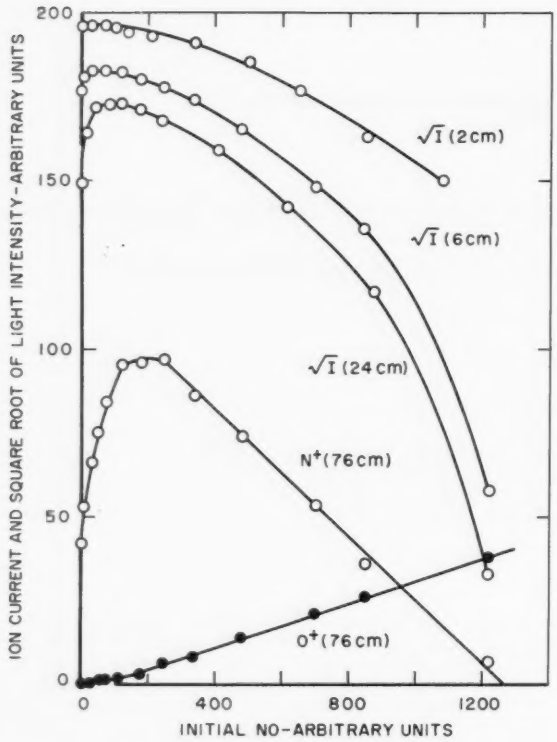


FIGURE 1. *Relative* N *and* O *atom partial pressure from mass spectrometric and photometric measurements as a function of the initial* NO *partial pressure, at various distances from the* NO *inlet.*

The photometric measurements are not corrected for emission from the $NO^+$ formed in the reaction of N with O. (NO inlet located 20 cm below the discharge zone. Total pressure 3 torr.)

Oxygen atoms were also detected when $O_2$ was added after the discharge. If the $O_2$ was partially decomposed in a discharge before addition, then only about ⅓ as much $O_2$ was required to maximize the N atom partial pressure. When $^{15}NO$ was used as an additive, the maximum amount of $^{15}N$ produced (at any point) was no greater than 0.4 percent of the $^{14}N$ originally present. This indicates that, barring some improbable reactions, NO is not decomposed by active nitrogen, but rather reacts via $N + NO \rightarrow N_2 + O$, confirming previous studies on untreated active nitrogen [7, 8].

Some additional experiments were made using a photomultiplier to monitor the nitrogen afterglow intensity (proportional to $[N]^2$) at various points along the reactor when NO was added after the discharge. These data are shown in figure 1. The nonlinearity of $\sqrt{I}$ curves is caused by emission from NO formed by the reaction of N and O atoms [9]. Figure 1 is a composite curve, and there is no absolute connection between each set of data.

No striking difference was observed when reactants were added before, directly into, or after the pink nitrogen afterglow.

## 4. Effects of Additives on Metastable $N^2$ Molecules

Foner and Hudson [10] have shown that metastable $N_2$ molecules in active nitrogen can be detected by means of mass spectrometry. By working at reduced electron energies (17 eV nominal) it was possible in the present work to detect an increase in the ion current at m/e 28 when the discharge was turned on.

If the metastable was generated only in the discharge zone, then its decay in the presence of an additive can be described by the reactions:

$$N_2^* + A \xrightarrow{k_1} \text{products} \qquad (1)$$

$$N_2^* \xrightarrow{k_2} N_2 \qquad (2)$$

Reaction (2) may be influenced by the wall, or may simply represent the radiative decay of the metastable state.

The overall rate of disappearance of $N_2^*$ can be written as:

$$-\frac{d[N_2^*]}{dt} = k_1[N_2^*]\,[A] + k_2[N_2^*]$$

Since $[A]$ is constant under the conditions described here

$$-\frac{d[N_2^*]}{[N_2^*]} = k_1[A]dt + k_2 dt$$

$$\text{or } \log [N_2^*]_t = -\frac{k_1 t}{2.303}[A] - \frac{k_2 t}{2.303}.$$

Here $[N_2^*]_t$ is the relative partial pressure of the metastable species at a fixed time $t$.

The effects of adding $NH_3$ or $N_2O$ to active nitrogen are striking. A plot of $\log [N_2^*]_t$ versus $[A]$ for these additives is shown in figure 2 (in terms of partial pressure). It is obvious that the simple kinetic scheme is inadequate.

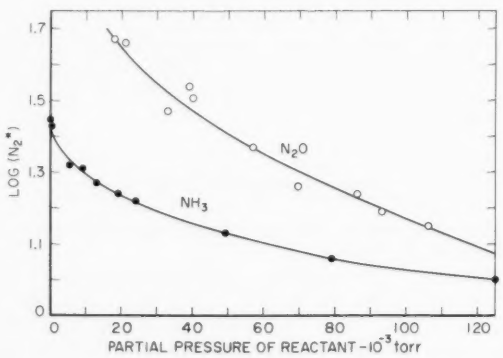


FIGURE 2. *Relative partial pressure of metastable* $N_2$ *as a function of the partial pressure of* $NH_3$ *and* $N_2O$ *additives (total pressure 3 torr).*

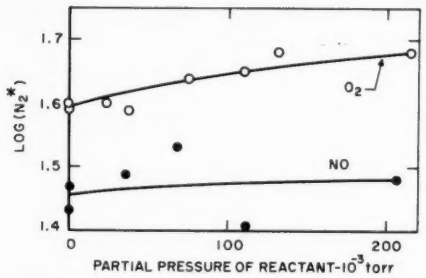


FIGURE 3. *Relative partial pressure of metastable* $N_2$ *as a function of the partial pressure of* NO *and* $O_2$ *additives (total pressure 3 torr).*

The addition of $O_2$ or NO caused a shift in the base line for $N_2^+$ so that small effects are difficult to determine. A plot of log $[N_2^*]_r$ versus $[A]$ for these additives is shown in figure 3. It would appear that neither of them appreciably deactivates the metastable species [11]. The same observation was made for $NF_3$.

## 5. Discussion

Examination of figure 1 shows that the maximizing effect of NO on the N atom partial pressure increases as the distance between the point of addition and the point of detection is increased. Since the NO+N reaction is so rapid that all the NO would be consumed within a distance of about 5 cm from the point at which it was added in the flow system used in this work, it is unlikely that NO itself could be connected with effects observed further downstream. It is more likely that O atoms are the responsible species. This is supported by the observation that partially decomposed $O_2$ is more effective than ordinary $O_2$ in maximizing the N atom partial pressure.

If a catalytic reaction between O atoms and some N atom precursor is invoked, the reaction is either relatively slow, or the precursor concentration must increase with distance (time). The latter possibility seems highly improbable, while the former would predict a shift in the position of the N atom maximum to higher initial NO partial pressure as the distance was reduced and not to lower initial NO partial pressure as observed.

A better explanation for the shapes of these curves is a change in the rate of disappearance of N atoms on the walls occasioned by a change in the accommodation coefficient. The latter effect is probably due to "poisoning" of the walls with oxygen atoms. This explains the nonlinearity of the $O^+$ curve up to the point of maximum $N^+$. Once the walls are saturated with O atoms, the N atom partial pressure begins to decrease linearily and the O atom partial pressure to increase linearily.

The greater rate of recombination of atoms on the walls would also explain the fact that the walls become extremely hot in the case of purified active nitrogen. Enhanced wall activity may also play a significant part in the formation of the "pink" afterglow, since the latter is best obtained in purified active nitrogen and is dependent on wall parameters.

The importance of wall effects was directly observable under certain conditions. Thus, if the reactor was first cleaned with HF, a considerable reduction was observed in both afterglow intensity and detectable N atoms. However, a band about 3 mm deep was observed to form on the walls of the tube about 15 cm from the discharge, and then slowly to move down the tube (at about 3 cm/min). The nitrogen afterglow was distinctly more intense on the upstream side of the band. Addition of $O_2$ to the discharge intensified this effect. When the $O_2$ was shut off, the walls took on a dull red glow.

Although the effects of the other additives used has not been studied in any detail, a similar wall poisoning mechanism is applicable, involving either the additive or its reaction products.

There appeared to be no connection between the maximizing of the N atom partial pressure and the magnitude of metastable $N_2$ partial pressure. The only pertinent observation here was that the metastable partial pressure was somewhat larger in purified nitrogen.

## 6. Conclusion

The number of parameters and complexity of the mechanisms involved makes it difficult to draw firm conclusions about the nature of active nitrogen. It is suggested however, that wall effects play an important part in the "catalytic" production of nitrogen atoms, and in the production of the "pink" afterglow. Further it is observed that the catalytic effect is not connected with those metastable $N_2$ molecules detectable by mass spectrometry, and that the latter are not appreciably affected by the addition of nitric oxide.

## 7. References and Notes

[1] R. A. Young and R. L. Sharpless, Disc. Faraday Soc. **33,** 228 (1962).
[2] J. P. Kaplan, Phys. Rev. **42,** 807 (1932); G. E. Beale, Jr., and H. P. Broida, J. Chem. Phys. **31,** 1030 (1959).
[3] G. B. Kistiakowsky and G. G. Volpi, J. Chem. Phys. **27,** 1141 (1957).
[4] R. A. Young, R. L. Sharpless, and R. Stringham, J. Chem. Phys. **40,** 117 (1964).
[5] F. S. Klein and J. T. Herron, J. Chem. Phys. **41,** 1285 (1964).
[6] A torr is defined as 1/760 of normal atmospheric pressure.
[7] J. T. Herron, J. Chem. Phys. **33,** 1273 (1960).
[8] R. A. Back and J. Y. P. Mui, J. Phys. Chem. **66,** 1362 (1962).
[9] In separate experiments at distances of 2 cm and 24 cm from the NO inlet, the light intensity was monitored using an orange filter to remove most of the NO $\beta$ emission. The use of the filter made the curves more linear beyond the maximum, but had no significant effect on the position of the maximum.
[10] S. N. Foner and R. L. Hudson, J. Chem. Phys. **37,** 1662 (1962).
[11] The reaction $N+NO \rightarrow N_2+O$ leads to the formation of $N_2$ predominantly in the 4th or higher vibrational levels (D. E. Morgan, L. F. Phillips, and H. I. Schiff, Disc. Faraday Soc. **33,** 118 (1962) and therefore might contribute to the measured metastable peak. In separate experiments the $N^{14}N^{15*}$ generated by the reaction of $N^{15}O$ with N has been studied. The magnitude of this contribution was about 5 percent of that produced directly in active nitrogen.

(Paper 69A3-348)

JOURNAL OF RESEARCH of the National Bureau of Standards—A. Physics and Chemistry
Vol. 69A, No. 3, May–June 1965

# Synthesis and Ring Structure of 7-Acetamido-7-deoxy-L-*galacto*-heptulose

**Emma J. McDonald***

(January 8, 1965)

7-Acetamido-7-deoxy-L-*galacto*-heptulose was prepared by oxidation of 1-acetamido-1-deoxy-D-*glycero*-D-*galacto*-heptitol with *Acetobacter suboxydans*. The new acetamido-deoxy-L-heptulose was shown to be a pyranose by comparison with β-D-fructopyranose. The following equations represent the optical rotation of 7-acetamido-7-deoxy-α-L-*galacto*-heptulopyranose in water at 20 °C and 3.5 °C, respectively:

$$[\alpha]^{20}_{D} = -15.5e^{-.0396t} - 97.1,$$

$$[\alpha]^{3.5}_{D} = -11.9e^{-.0101t} - 105.8,$$

where $t$ is the time in minutes after dissolution of the sample.

## 1. Introduction

Several years ago, exploratory work in this laboratory, as well as work by others [1][1], showed that *Acetobacter suboxydans* oxidizes certain acetamido-deoxy-D-alditols to the corresponding acetamidodeoxy-ketoses. According to the Bertrand-Hudson rule [2], one would expect *A. suboxydans* to produce 7-acetamido-7-deoxyheptuloses from eight 1-acetamido-1-deoxyheptitols. This paper reports the preparation and properties of a new heptulose, 7-acetamido-7-deoxy-L-*galacto*-heptulose, obtained by oxidation of 1-acetamido-1-deoxy-D-*glycero*-D-*galacto*-heptitol.

## 2. Results and Discussion

The new ketose (I) is closely related to D-fructose (II) and perseulose (III). The optical rotations and the magnitude and direction of the mutarotations given in table 1 can be used for the assignment of structure. Isbell and Pigman [3] established that crystalline D-fructose is a β-D-pyranose and that its mutarotation arises from a pyranose-furanose interconversion. The molecular rotation of I (-28,300) does not differ greatly from the molecular rotations of II (−23,800) and III (−21,400), but differs widely from the molecular rotation (+3,060) of D-fructofuranose (Hudson's "α-fruc-

TABLE 1. *Optical rotation of certain ketoses*

| Ketoses | Temp | Specific rotation | | $k$[a] | $[\alpha]_D = Ae^{-kt} + C$ | Solvent | References |
|---|---|---|---|---|---|---|---|
| | | Initial | Final | | | | |
| | °C | | | $min^{-1}$ | | | |
| 7-Acetamido-7-deoxy-α-L-*galacto*-heptulopyranose (I) | 20 | −112.6 | −97.1 | 0.0172 | $[\alpha]^{20}_D = -15.5e^{-.0396t} - 97.1$ | $H_2O$ | [b] |
| | 3.5 | −117.7 | −105.8 | .0044 | $[\alpha]^{3.5}_D = -11.9e^{-.0101t} - 105.8$ | $H_2O$ | [b] |
| β-D-Fructopyranose (II) | 20 | −132.2 | −92.4 | .055 | $[\alpha]^{20}_D = -39.8e^{-.1266t} - 92.4$ | [c] | [3] |
| | 0 | −132.9 | −103.4 | .0090 | $[\alpha]^{0}_D = -29.5e^{-.0207t} - 103.4$ | [c] | [3] |
| α-L-*galacto*-Heptulopyranose (III) (perseulose) | 20 | −102 | −86 | .059 | ..... | $H_2O$ | [13] |

[a] $k = 1/t \log (r_0 - r_\infty)/(r - r_\infty)$. Measurements conducted as described in reference [12].
[b] New measurement.
[c] 0.001*N* potassium acid phthalate.

*Retired. Inquiries concerning this paper should be directed to the Division of Analytical Chemistry, National Bureau of Standards, Washington, D.C. 20234.

[1] Figures in brackets indicate the literature references at the end of this paper.

tose" [4]). One would expect small differences in molecular rotation because of differences in the substituents on C-6. The parallelism in the molecular rotations, however, is sufficient to indicate that the three compounds have similar structures. Compounds I, II, and III also show marked parallelism in the magnitude and direction of mutarotation. In each instance, the optical rotation decreases rapidly at a unimolecular rate. The rate for I (approximately one-third that for II and III) is not surprising because of the differences in the substituents on C-6. The effect of a change in temperature on the equilibrium rotation of I and II is much the same. In each instance, lowering the temperature shifts the equilibrium in the direction of the isomer known in the crystalline form. From these considerations (molecular rotation, mutarotation, and effect of temperature), it follows that I is a pyranose and that it has the configuration corresponding to that of β-D-fructopyranose. According to accepted nomenclature, anomers in the L-series having the same configuration for the anomeric carbon as a β-D-pyranose are designated as α-L-pyranoses, and I is named 7-acetamido-7-deoxy-α-L-*galacto*-heptulopyranose. Presumably, the mutarotation of I (like that of β-D-fructopyranose) arises from a pyranose-furanose interconversion.

The infrared absorption of I (fig. 1) shows bands at 6.02, 6.38, and 7.7 μ indicative of the free amido group. Hence, the nitrogen of the amido group is not part of a ring as it is in certain 5-acetamido-5-deoxypentoses [5 to 8].

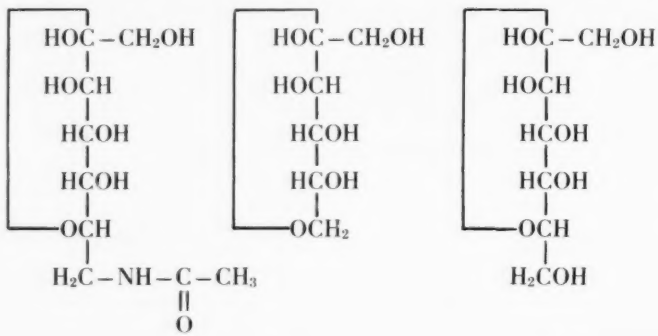


I II III

I. 7-Acetamido-7-deoxy-α-L-*galacto*-heptulopyranose.
II. β-D-Fructopyranose.
III. α-L-*galacto*-Heptulopyranose (perseulose).

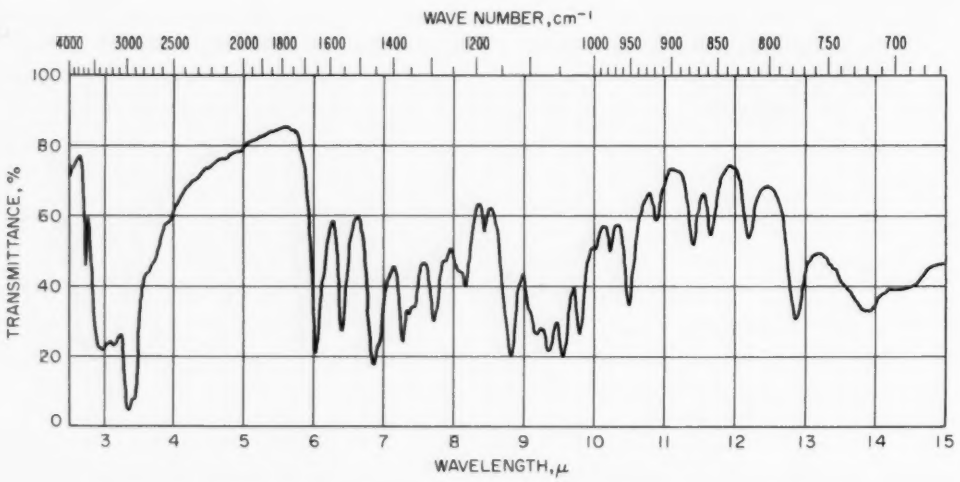


FIGURE 1. *Spectrogram of 7-acetamido-7-deoxy-α-L-galacto-heptulopyranose in Nujol mull.*

Several properties of the new 7-acetamido-7-deoxy-L-*galacto*-heptulose were determined for characterization. With *l*-butanol:pyridine:water (3:2:1) as an ascending developing solvent, the mobility of the compound on Whatman No. 1 paper is 0.88 that of fructose. Color formation with staining reagents sensitive to ketones is as follows: phloroglucinol, violet; urea phosphate, yellow (bright yellow fluorescence); resorcinol, tan (violet fluorescence); orcinol, purple (red fluorescence). The compound reacts with Somogyi's copper-reducing reagent at approximately the same rate as fructose. It melts at 139 to 140 °C and yields a phenylosazone, mp 210 °C.

In conjunction with the synthesis of I, methods for the preparation of 1-amino-1-deoxyalditols were examined. Catalytic reduction of glycosylamines proved to be unsatisfactory because of the instability of the glycosylamines in neutral or slightly acid solution [9]. Reduction of sugar oximes [10] was satisfactory, and this method is recommended for small-scale preparations of 1-amino-1-deoxyalditols from readily available aldoses. Reduction of 1-nitro-1-deoxyalditols, prepared from the lower sugars by condensation with nitromethane [11], proved to be the most satisfactory method; reduction takes place readily and gives the amines in high yield.

## 3. Experimental Procedures

### 3.1. 1-Nitro-1-deoxy-D-*glycero*-D-*galacto*-heptitol

Nitromethane was condensed with α-D-mannose and the resulting 1-nitro-1-deoxy-D-*glycero*-D-*galacto*-heptitol and 1-nitro-1-deoxy-D-*glycero*-D-*talo*-heptitol were separated by the procedure of Sowden and Schaffer [11].

### 3.2. 1-Acetamido-1-deoxy-D-*glycero*-D-*galacto*-heptitol

A slurry consisting of 2 g of 1-nitro-1-deoxy-D-*glycero*-D-*galacto*-heptitol, 0.65 g of 10-percent palladium on carbon, and 50 ml of water was shaken for 1.5 hr, at room temperature, with hydrogen under a pressure of 30 psi. The resulting suspension was filtered, and the filtrate was evaporated to dryness under reduced pressure. A solution of the residue, crude 1-amino-1-deoxy-D-*glycero*-D-*galacto*-heptitol,[2] in 15 ml of warm water was cooled, treated with 2 ml of acetic anhydride, and filtered. Additional acetic anhydride (2 ml) was added to the filtrate, which was kept for 1.5 hr at room temperature and then treated with ethanol to the point of slight turbidity. After 20 hr, the resulting crystalline, 1-acetamido-1-deoxy-D-*glycero*-D-*galacto*-heptitol was separated and air-dried; yield, 1.65 g; mp, 200 °C (uncor); $[\alpha]^{20}D = -15.5°$ (*c* 2.1, water).

*Anal.* Calcd. for $C_9H_{19}NO_7$: C, 42.7; H, 7.6; N, 5.5. Found: C, 42.7; H, 7.4; N, 5.4.

### 3.3. 7-Acetamido-7-deoxy-α-L-*galacto*-heptulopyranose

1-Acetamido-1-deoxy-D-*glycero*-D-*galacto*-heptitol (5.1 g), D-mannitol (0.25 g), potassium dihydrogen phosphate (0.025 g), and yeast extract (0.25 g) were dissolved in 50 ml of water. Two 25-ml portions, in 125-ml flasks, were sterilized for 20 min in steam under a pressure of 20 psi, cooled, and inoculated with *A. suboxydans*. The reaction flasks were kept at 20 to 30 °C, and the reaction was followed by paper chromatography. After 10 days, the combined product was treated as follows: One ml of a 20-percent solution of zinc sulfate was added, and the mixture was neutralized to phenolphthalein with a saturated solution of barium hydroxide. The suspension was filtered, and the filtrate was deionized with a mixture of cation- and anion-exchange resins, and evaporated to dryness. The residue was extracted with 80-percent aqueous methanol; the solid material (unoxidized 1-acetamido-1-deoxy-D-*glycero*-D-*galacto*-heptitol) was removed by filtration, and the filtered solution was evaporated under reduced pressure. The residue was dissolved in water and lyophilized to remove all solvent. The solid material was dissolved in a minimal amount of methanol, and ethyl ether added to the point of incipient turbidity. After several weeks, crystalline I separated. The compound was recrystallized from methanol; yield, 3.18 g; mp, 139 to 140 °C. The substance exhibits the mutarotation represented in table 1. $[\alpha]^{20}D = -112.6°$ initially, and $-97.1°$ at equilibrium; $[\alpha]^{3.5}D = -117.7°$ initially and $-105.8°$ at equilibrium (*c* 3.3, water).

*Anal.* Calcd. for $C_9H_{17}NO_7$: C, 43.02; H, 6.82; N, 5.58. Found: C, 43.15; H, 6.85; N, 5.6.

### 3.4. 7-Acetamido-7-deoxy-L-*galacto*-heptulose Phenylosazone

7-Acetamido-7-deoxy-L-*galacto*-heptulose (200 mg), phenlyhydrazine (35 mg), acetic acid (200 mg), and water (5 ml) were heated in a boiling-water bath for 2 hr. The resulting phenylosazone was separated by filtration and washed successively with dilute acetic acid, 95-percent ethanol, and ether; yield, 243 mg. After recrystallization from ethanol, the phenylosazone melted with decomposition at 209 °C.

*Anal.* Calcd. for $C_{21}H_{27}N_5O_5$: C, 58.7; H, 6.3; N, 16.3. Found: C, 58.1; H, 6.3; N, 16.1.

### 3.5. 7-Acetamido-7-deoxy-L-*galacto*-heptulose Phenylosotriazole

The phenylosazone of I (191 mg) was refluxed for 2 hr with a solution prepared from 121 mg of copper sulfate pentahydrate and 15 ml of water. The hot suspension was filtered to remove cuprous oxide and unreacted phenylosazone, and the filtrate was passed

[2] In a separate experiment, the reduction product, on treatment with oxalic acid, gave the previously known [11] crystalline 1-amino-1-deoxy-D-*glycero*-D-*galacto*-heptitol oxalate, mp 193 to 195 °C with decomposition; $[\alpha]^{25}D = -13.2°$ (*c* 3.4, water). The direction of optical rotation was not given in the publication cited, but the compound is now shown to be levorotatory.

through a column of mixed cation- and anion-exchange resins. After the eluate had been evaporated under reduced pressure, the phenylosotriazole of I crystallized; the compound was recrystallized three times from hot water; mp, 210 °C.

*Anal.* Calcd. for $C_{15}H_{20}N_4O_5$: C, 53.6, H, 5.99. Found: C, 53.6; H, 5.5.

---

The author expresses her appreciation to H. S. Isbell for suggesting the research problem and for highly valued counsel, and to R. J. Hall and J. K. Taylor for microanalyses.

(Paper 69A3–349)

## 4. References

[1] L. Hough, J. K. N. Jones, and D. L. Mitchell, Can. J. Chem. **37,** 725 (1959). J. K. N. Jones, M. B. Perry, and J. C. Turner, Can. J. Chem. **39,** 965, 2400 (1961); **40,** 503 (1962). J. C. Turner, Can. J. Chem. **40,** 826 (1962).
[2] R. M. Hann, E. B. Tilden, and C. S. Hudson, J. Am. Chem. Soc. **60,** 1201 (1938).
[3] H. S. Isbell and W. W. Pigman, J. Res. NBS **20,** 773 (1938) RP1104.
[4] C. S. Hudson, J. Am. Chem. Soc. **31,** 655 (1909).
[5] S. Hanessian and T. H. Haskell, J. Org. Chem. **28,** 2604 (1963).
[6] H. Paulsen, Angew. Chem. **74,** 901 (1962).
[7] J. K. N. Jones and J. C. Turner, J. Chem. Soc. **1962,** 4699.
[8] W. A. Szarek and J. K. N. Jones, Can. J. Chem. **42,** 20 (1964).
[9] H. S. Isbell and H. L. Frush, J. Am. Chem. Soc. **72,** 1043 (1950).
[10] L. Maquenne and E. Roux, Compt. Rend. **132,** 980 (1901); **135,** 69 (1902). E. Roux, Ann. Chim. Phys., série 8, **1,** 72 (1904).
[11] J. C. Sowden and R. Schaffer, J. Am. Chem. Soc. **73,** 4662 (1951).
[12] H. S. Isbell and W. W. Pigman, J. Res. NBS **18,** 141 (1937). RP969.
[13] R. M. Hann and C. S. Hudson, J. Am. Chem. Soc. **61,** 336 (1939).

JOURNAL OF RESEARCH of the National Bureau of Standards—A. Physics and Chemistry
Vol. 69A, No. 3, May–June 1965

# Publications of the National Bureau of Standards*

## Selected Abstracts

**Excitation of acoustic waves in plasmas,** W. A. Saxton, *Radio Sci. J. Res. NBS/USNC–URSI,* **69D,** No. 4 (Apr. 1965).
This paper reports early results in an experimental study to determine the effects of perturbing weakly ionized gaseous plasmas with acoustic waves emanating from transducers that operate in the audio and ultrasonic frequency ranges. Compact loudspeakers incorporated into cylindrical plasma discharge tubes provide the source of acoustic signals. Modulation of electromagnetic waves by the acoustically-disturbed plasma is measured in a unique rectangular cavity whose output is detected and fed to a wave analyzer. Resultant wave-analyzer responses indicate that the collision frequency is modulated in addition to the plasma frequency, and suggest that the variations in both are proportional to the magnitude of loudspeaker diaphragm deflection, as predicted by simple acoustic theory. Knowing that two forms of modulation occur simultaneously, a calibration scheme was developed to separate the variation $\Delta f_p$ in the plasma frequency from the total response. Measurements to date indicate that $\Delta N_e/N_e = \Delta N/N$ (where $N_e$ and $N$ are electron and neutral-molecule densities, respectively) for slightly-ionized gases which are subjected to low-frequency pressure variations in the order of $10^{-5}$ mm Hg, and that such variations produce plasma-frequency perturbations of 0–140 kc/s at plasma frequencies up to 800 Mc/s.

**Wave interaction in oxygen magnetoplasmas,** K. V. Narasinga Rao, Radio Sci. J. Res. NBS/USNC–URSI, **69D,** No. 4 (Apr. 1965).
Electron cyclotron resonance absorption of microwaves in decaying oxygen magnetoplasmas is utilized to alter the plasma parameters such as the "temperature" and number density of the electrons. The technique of cross modulation of microwaves in partially filled plasma waveguides is used in this investigation. It is shown that for small amplitudes ( ~ 120 mW at 5.3 Gc) of the resonant heating signal the inelastic collision of low energy electrons introduce a barrier for rapid heating the electron gas. For higher incident amplitudes ( ~ 500 mW at 5.3 Gc), not only does rapid heating of the electron gas occur, but also additional electron production and loss mechanisms are observed. The implications of these results on (a) apparent discrepancies in measurements of attachment coefficient by microwave methods, and (b) control of ionospheric plasma parameters by radio wave absorption are discussed.

**Test of the constancy of the velocity of electromagnetic radiation in high vacuum,** P. Beckmann and P. Mandics, *Radio Sci. J. Res. NBS/USNC–URSI* **69D,** *No. 4 (Apr. 1965).*
It is pointed out that Einstein's postulate of the constant velocity of light is verified only indirectly by elementary-particle experiments leaning more or less heavily on present electromagnetic theory, the latter being verified only for low velocities. Direct experiments can be explained by the ballistic theory of light if transparent media, such as gases, reradiate as a secondary source. A direct experiment with coherent light reflected from a moving mirror was performed in vacuum better than $10^{-6}$ torr. Its result is consistent with the constant velocity of light.

**Transmission and reflection of electromagnetic waves by a hot plasma,** E. C. Taylor, *Radio Sci. J. Res. NBS/USNC–URSI* **69D,** *No. 5, (May 1965).*
The relativistic form of the Vlasov equation is used to solve the problem of transmission and reflection of normally incident electromagnetic waves. Transmission and reflection coefficients are derived for a plasma half-space and for a plasma slab, using the assumption that electrons are specularly reflected at the boundaries. These coefficients are functions of the ratio of the electron thermal speed to the vacuum speed of light, indicating that temperature dependence in these cases is a relativistic effect. Nevertheless, it is seen that the nonrelativistic limits of these coefficients differ from those obtained by using the cold-plasma equations since the transition to the zero-temperature limit has a nonuniform character.

**Microwave spectral tables. Diatomic molecules,** P. F. Wacker, M. Mizushima, J. D. Petersen, and J. R. Ballard, *NBS Mono. 70, (Dec. 1, 1964) $2.00.*
For about 1500 spectral lines of diatomic molecules observed by coherent radiation techniques, measured frequencies, assigned molecular species, assigned quantum numbers, and newly computed intensities are given. Molecular data, such as rotational constants, dipole moments, and various coupling constants, determined by such techniques, are also tabulated, as are other molecular constants used in the intensity computations. References are given for all included data. For determination of hyperfine spectra, both Casimir's function and the intensity splitting factor are given for both integral and half-integral quantum numbers $J$ and $I$, permitting application to additional molecules with unclosed electronic shells and with hyperfine splitting produced by more than one nucleus.

**Microwave spectral tables. Line strengths of asymmetric rotors,** P. F. Wacker and M. R. Pratto, *NBS Mono. 70, Vol. II (Dec. 15, 1965) $3.00.*
Line strengths of asymmetric rotors are tabulated as a function of Ray's asymmetry parameter $\kappa$ for rotational quantum numbers $J$ from 0 to 35. Procedures for interpolation as a function of $\kappa$ and extrapolation to larger $J$ values are discussed.

**On the statistical theory of electromagnetic waves in a fluctuating medium (II) Mathematical basis of the analogies to quantum field theory,** K. Furutsu, *NBS Mono. 79 (Dec. 7, 1964) 35 cents.*
Many analogies to quantum field theory are inherent in the statistical theory of waves. This is due to the fact that basic equations exist in the latter theory which correspond closely to the fundamental equations of the former theory; i.e., to the commutation relations and the Heisenberg equation of motion. A probability density function of waves is introduced here which corresponds to the probability amplitude function in quantum mechanics. The boundary conditions at infinity for this probability density function are then found to be expressed in the same form as the vacuum boundary conditions in field theory. The theory of the statistical Green's functions and their relationships to the expectation values of the physical variables is also extensively developed, using auxiliary external sources of the wave and of the fluctuating medium. It is found that there exists a one-to-one correspondence between the formalism of Green's functions presented here and that used in field theory. The above correspondence may be important for a further development of the statistical theory of waves, just as the advanced techniques of field theory have greatly influenced the development of thermodynamics (or statistical physics).

**On the formulation and numerical evaluation of a set of two-phase flow equation modelling the cooldown process,** S. Jarvis, Jr., *NBS Tech. Note 301* (Jan. 4, 1965) 55 cents.
A model of transient two-phase flow in a pipe is constructed in Eulerian coordinates assuming a single velocity but independent temperatures in the two phases. Experiments on the numerical integration of the system for cooldown problem by both Lax and Courant-Isaacson-Rees methods indicate that a very fine spatial difference net must be used to compensate for the numerical diffusion essential to computational stability if a second surge is to be realized.

**Angular momentum distribution and emission spectrum of** OH ($^2\Sigma^+$) in the photodissociation of $H_2O$, T. Carrington, *J. Chem. Phys.* **41**, *No. 7, 2012–2018 (Oct. 1, 1964).*
When water vapor absorbs light of wavelength less than 1350 Å, an electronically excited OH fragment may be produced. This process has been observed, using wavelengths 1216 Å, 1236 Å, and 1302 Å, and the rotational and vibrational excitation of the product $OH^2\Sigma^+$ has been determined from its emission spectrum. Most of the energy beyond that necessary to produce electronically excited OH goes into rotation of that molecule. Roughly one-third of the OH molecules have one quantum of vibrational energy, and in these molecules too, the highest energetically allowed rotational levels are strongly populated. Knowledge of the energy and rotational angular momentum of the OH allows estimation of the kinetic energy and orbital angular momentum of the H as it flies away from the center of mass. This is interpreted in terms of a two body interaction at large distances.

**Morphology of thermally evaporated zinc cleavage surfaces,** A. W. Ruff, Jr., *J. Chem. Phys.* **41**, *No. 5, 1204–1213 (Sept. 1, 1964).*
The process of thermal evaporation has been studied on (0001) cleaved zinc surfaces. The effects on the evaporated surface structures due to zinc vapor undersaturation, impurities, and crystal dislocations were investigated. For undersaturation ratios between 0.29 and 0.006, evaporation proceeded primarily from localized surface regions resulting in shallow conical evaporation pits. The number density of these evaporation pits was in good agreement with the dislocation density determined by chemical etching. It was concluded that the step sources responsible for the evaporation pits were dislocations terminating at the surfaces. The theory of evaporation from dislocation sites predicts a critical undersaturation similar to that observed experimentally. The interferometrically measured evaporation pit slopes increased with vapor undersaturation in agreement with the theory of Cabrera and Levine near the critical undersaturation. The data extended further into the region of higher undersaturations. The effects of surface impurities were studied by admitting oxygen into the evaporation cell. For a constant vapor undersaturation, the evaporation pit slopes increased at the higher oxygen pressures. This increase could be explained qualitatively in terms of a reduction in step velocity.

**Statistical surface thermodynamics of simple liquid mixtures,** C. A. Eckert and J. M. Prausnitz, *A. I. C. H. E. J.* **10**, *No. 5, 677–683 (Sept. 1964).*
The surface properties of nonpolar liquid mixtures are derived from the application of the grand partition function to a cell model of the vapor-liquid interface. The surface tension and the surface composition are expressed in terms of the activity coefficients in the bulk liquid and pure-component properties. The results are in excellent agreement with existing data for the surface tension of mixtures. This treatment provides a sound theoretical basis for the prediction of surface properties of other liquid systems, and is especially applicable to cryogenic mixtures.

**The accurate measurement of voltage ratios of inductive voltage dividers,** T. L. Zapf, *Acta IMEKO, pp. 317–331 (1964).*
Several methods have been developed at the National Bureau of Standards for the very accurate measurement of audio frequency voltage ratios associated with inductive voltage dividers. Uncertainties in voltage ratio of less than $2 \times 10^{-7}$ have been obtained in measurements with transformer-type capacitance bridges. The attainment of such accuracy has provided a firm base for further investigations on inductive voltage dividers. An inherent major error arises from the interaction between distributed shunt impedances and leakage impedances in the windings. In specific designs of inductive voltage dividers the relative magnitudes of such errors are calculable and are characteristic of the design. A divider may be completely characterized by the designation of the characteristic relative errors combined with an absolute measurement. A method involving complementary measurements has been developed to yield an absolute measurement of the inphase and quadrature components of the voltage ratio characteristic. Single-decade inductive voltage dividers have been constructed with ratio magnitude characteristics and residual errors less than $5 \times 10^{-8}$. This recent work has verified the accuracy of measurements made by other methods.

**Correlation factors for impurity diffusion—Bcc, diamond, and Fcc structures,** J. R. Manning, *Phys. Rev.* **136**, *No. 6A, A1758–A1766 (Dec. 14, 1964).*
A general equation for the impurity correlation factor is derived in terms of effective escape frequencies. This equation applies even when the vacancy jump frequency for association of a vacancy-impurity complex differs from the frequency far from an impurity. Parameters in this equation are calculated for body-centered cubic, diamond, and face-centered cubic structures. In these calculations, it is assumed that vacancy jumps which do not involve a nearest neighbor of the impurity are unaffected by the impurity but that association and dissociation jumps, which do involve nearest neighbors of the impurity, are affected. Analytical expressions for the correlation factor in terms of vacancy jump frequency ratios are obtained. In the bcc and fcc structures, results are given for two cases: (A) where all dissociative jumps are equally likely, and (B) where a vacancy which makes a dissociative jump to a second nearest neighbor site is still partially bound to the impurity but vacancies which make dissociative jumps to other sites are not. In the diamond structure, case A cannot be distinguished from case B. Results for the diamond structure and for case A in the fcc structure differ only slightly from previous more approximate results. A comparison is made between the present random walk method of calculating correlation factors and the pair association method.

**Thermal decomposition of some alkyl halides by a shock-tube method,** W. Tsang, *J. Chem. Phys.* **41**, *No. 8, 2487–2494 (Oct. 15, 1964).*
The decomposition of several alkyl halides have been studied by a comparative rate method using a single pulse shock tube. Rate constants for the elimination of hydrogen halide from the parent molecule are compared with the rate of elimination of hydrogen bromide from isopropyl bromide. The Arrhenius expression for the latter reaction has previously been found to be $k\ (i\text{-}C_3H_7Br) = 10^{13.62}e^{-47,800/RT}\ (sec^{-1})$. On this basis, the following rate expressions have been obtained:

| | |
|---|---|
| $k\,(C_2H_5Br) = 10^{13.19}e^{-53,700/RT}\ (sec^{-1})$ | 740–940 °K |
| $k\,(C_2H_5Cl) = 10^{13.16}e^{-56,460/RT}\ (sec^{-1})$ | 820–1000 °K |
| $k\,(i\text{-}C_3H_7Cl) = 10^{13.64}e^{-51,100/RT}\ (sec^{-1})$ | 750–950 °K |
| $k\,(i\text{-}C_3H_7I) = 10^{13.67}e^{-45,065/RT}\ (sec^{-1})$ | 680–850 °K |
| $k\,(t\text{-}C_4H_9I) = 10^{13.73}e^{-38,080/RT}\ (sec^{-1})$ | 650–760 °K |

These results are compared with the results of earlier low temperature studies. The advantages and reliability of this type of kinetic study are discussed.

**Relaxation of a Lorentz gas with repulsive $r^{-s}$ force law,** H. Oser, K. E. Shuler, and G. H. Weiss, *J. Chem. Phys.* **41**, *No. 9, 2661–2666 (Nov. 1, 1964).*
The relaxation of a Lorentz gas (dilute light particle subsystem in a heavy particle heat bath) has been studied for a repulsive $r^{-s}$ central force law interaction between the light and heavy particles. The Fokker-Planck equation for the velocity distribution functions of the light particle subsystem has been solved numerically for $s = 5, 9, 13, 21$ and $\infty$ for various initial conditions. The dependence of the rate of relaxation and of the form of the time dependent velocity distribution function on the force law parameter $s$ is discussed in light of the above results.

**Modulus of rupture of glass in relation to fracture pattern,** M. J. Kerper and T. G. Scuderi, *Am. Ceramic Soc. Bull.* **43**, *No. 9, 622–625 (Sept. 7, 1964).*
Glass broken in flexure shows a fracture face which normally consists in part of a smooth area that includes the fracture origin. The area of this smooth portion of "mirror" has been found to bear a relationship to the magnitude of the stress causing rupture. This relationship has been studied for eight glasses tested under a variety of conditions. It was observed that the conditions of the glass surface, the test temperature, difference in exposure time to test temperature, and rate of loading, all had an effect on the strength of glass but did not affect the relationship between modulus of rup-

ture and the mirror size. The composition did, however, affect this relationship. This relationship is generally expressed as a power function where the modulus of rupture times the radius of the mirror to the one half power is equal to a constant. This expression is not, however, valid for the full range of the data.

**Mass-spectrometric study of the reactions of O atoms with NO and $NO_2$,** F. S. Klein and J. T. Herron, *J. Chem. Phys.* **41,** *No. 5, 1285–1290 (Sept. 1, 1964).*
The reaction of O atoms with NO and $NO_2$ have been studied using a mass spectrometer to directly measure the O atom partial pressure. The results obtained are as follows:

$$NO + O + M \rightarrow NO_2 + M \qquad k_1(M = N_2) = (1.44 \pm 0.20) \times 10^{15} \exp(1930 \pm 100/RT) cc^2 \text{ moles}^{-2} \text{ sec}^{-1},$$

$$NO_2 + O \rightarrow NO + O_2 \qquad k_2 = (1.95 \pm 0.61) \times 10^{13} \exp.(-1060 \pm 200/RT) \text{ cc. moles}^{-1} \text{ sec}^{-1}.$$

These reactions are discussed in terms of the general mechanism

$$O + XO \underset{B}{\overset{A}{\rightleftharpoons}} (OXO)^* + M \xrightarrow{B} XO_2 + M$$

$$C \longrightarrow X + O_2^*$$

$$D \longrightarrow XO_2 + h\nu$$

From the overall rate constants and previous results on the isotopic exchange rates of $O^{18}$ with $O_2$, NO, and $NO_2$ (J. T. Herron and F. S. Klein, J. Chem. Phys. (1964)) the rates of the elementary reaction steps have been calculated.

**Infrared studies of the photolysis of $HN_3$ in inert and reactive matrices. The infrared spectrum of NH,** D. E. Milligan and M. E. Jacox, *J. Chem. Phys.* **49,** *No. 9, 2838–2841 (Nov. 1, 1964).*
Infrared and ultraviolet observations have been made on the products of the photolysis of $HN_3$ and $DN_3$ suspended in Ar, $N_2$, and $CO_3$ matrices at 4, 14, and 20 °K. Appreciable concentrations of NH (ND) in the ground ($^3\Sigma^-$) state are produced. The vibrational fundamental of NH has been observed directly at $3133 \pm 2$ $cm^{-1}$ in Ar and $N_2$ matrices. The identification of H atoms in the photolysis of $HN_3$ requires that some of the $HN_3$ molecules undergo photolytic rupture at the H–N bond. Consideration is given to the secondary reactions which occur between NH and itself or $HN_3$. It appears likely that HN=NH and/or HN=N–N=NH may contribute to the observed products of these secondary reactions.

**Contributions to the theory of shell corrections,** U. Fano and J. E. Turner, *ch. 4, 49–67, Nuclear Sci. Series Report No. 39, Natl. Acad. Sci.-Natl. Res. Council Publ. 1133 (1964).*
Sum rules pertaining to the inelastic form factor $F_n(\mathbf{q})$ are calculated and applied to the evaluation of shell corrections to the stopping power formula, to order $1/v^4$ in the velocity of the incident particle. Details are given pertaining to the evaluation of the shell corrections in the paper reproduced in Appendix A. Comments are presented regarding the possible generality of a Lindhard-Winther equipartition rule.

**Electrode potentials in fused system. VIII. Oxidation kinetics of silver in sodium chloride,** K. H. Stern and W. E. Reid, Jr., *J. Phys. Chem.* **68,** *No. 12, 3757–3764 (Dec. 1964).*
The oxidation rate of metallic silver in molten sodium chloride has been studied by a galvanic old technique as a function of oxygen partial pressure, o- 1st and temperature (800–900 °K). The results are accounted for by two forward reactions: (A) $2Ag + \frac{1}{2} O_2$ $k_1 2Ag^+ + O^=$, (B) $Ag^0 + Na^+ \overset{k_2}{\rightarrow} Ag^+ + Na^0$. $k_1$ is a linear function of $p_0$ in the range $0 < p \leq 1$ atm. For $p_{O_2} = 1$ at 870° $k_1 = 11.9 \times 10^{15}$, $k_2 = 0.35 \times 10^{152}$ atoms $cm^{-2}$ $sec^{-1}$. With increasing time $d[Ag^+]/dt$ decreases because of the reverse of reaction (A), for which $k_3 = \dfrac{k_1 + k_2}{K_A p_{O_2}^{1/2}}$, where $K_A$, the equilibrium constant for (A), is $8.3 \times 10^{-7}$ on the mole fraction scale. The general differential equation for this system is derived and numerically integrated. The mechanism of the reaction is discussed in terms of absolute reaction rate theory. It is concluded that the rate determining step for (A) is the chemisorption of $O_2$, which is hindered by an adsorbed layer of chloride ions, and that for (B) the formation of $Ag^+$ is rate-determining.

**Election scattering without atomic or nuclear excitation,** J. W. Motz, H. Olsen, and H. W. Koch, *Rev. Mod. Phys.* **36,** *No. 4, 881–928 (Oct. 1964).*
This survey is concerned with the process of single electron scattering by an atom without excitation of the atom or the nucleus. Results are given which pertain to the kinematics, the radiative effects, the polarization behavior, and the cross sections for this process over a wide range of electron energies extending from the nonrelativistic (> 10 kev) to the extreme relativistic regions.

**K-ionization cross sections for relativistic electrons,** J. W. Motz and R. C. Placious, *Phys. Rev.* **136,** *No. 3A, A662–A665 (Nov. 2, 1964).*
Experimental values of the *K*-shell ionization cross section are determined from scintillation spectrometer measurements of the *K* x rays emitted when thin targets of tin and gold are bombarded by 50, 100, 200, and 500 keV electrons. For these energies and atomic numbers, the experimental results show differences with the cross sections given by Burhop's nonrelativistic calculations and by Perlman's relativistic calculations, but show good agreement with the predictions of Arthurs and Moiseiwitsch who employed relativistic free particle wave functions for the projectile electron and nonrelativistic wave functions for the atomic electron.

**Tables of energy losses and ranges of electrons and positrons,** M. J. Berger and S. M. Seltzer, *Natl. Aeronaut. Space Admin. NASA SP-3012, 1–127 (1964).*
Tables are presented for approximately forty materials, and energies between 10 kev and 1000 Mev, which contain the following information: mean energy loss of electrons by collisions with atomic electrons and by bremsstrahlung, the mean range, and the radiation yield (conversion of electron kinetic energy into bremsstrahlung energy). Auxiliary tables contain information about restricted collision losses in water, critical energies (at which the collison and bremsstrahlung losses are equal), and electron-positron differences in regard to energy loss and range. Some comparisons are made between calculated and experimental values of the mean energy loss.

**Tables of energy losses and ranges of heavy charges particles,** W. H. Barkas and M. J. Berger, *Natl. Aeronaut. Space Admin. NASA SP-3013, 1–131 (1964).*
Two-variable proton stopping power and range tables are given as functions of the particle energy $\tau$ and of the mean excitation energy $I_{adj}$ of the medium, for 160 values of $\tau$ between 1 and 5000 Mev, and for 36 values of $I_{adj}$. These tables can be applied to any medium with specified mean exictation energy. By simple scaling, they can also be applied to other heavy particles with mass and charge different from that of the proton. The tabulated values below 8 Mev are based on experimental stopping-power and range data as summarized by a 9-parameter least-squares range formula. Above 8 Mev they are based on the Bethe stopping power theory, except for the shell corrections which are calculated by an empirical formula in the variables $\tau$ and $I_{adj}$ derived form the analysis of experimental data.

**Application of the theory of absorbing Markov chains to the statistical thermodynamics of polymer chains in a lattice,** J. Mazur, *J. Chem. Phys.* **41,** *No. 8, 2256–2266 (Oct. 15, 1964).*
A concept of absorbing Markov processes is employed in order to study the statistical thermodynamics of infinitely long polymer chains, simulated by a random flight on a lattice. These polymer chains interact in the sense that certain chain conformations are associated with intramolecular interactions, defined by short-range, steplike potentials. Various thermodynamic functions are derived from the polymer partition function, which, in turn, is obtained from the largest eigenvalue of the matrix of transition probabilities. The thermodynamic functions of this simplified polymer model are evaluated for some lattice models and for different forms of the interaction potentials. The results thus obtained are then compared with more accurate, but much more lengthy, Monte Carlo or direct-counting computations.

## Other NBS Publications

**J. Res. NBS 69C (Eng. and Instr.), No. 2 (Apr.–June 1965), 75 cents.**

Temperatures of thermocouple reference junctions in an ice bath. F. R. Caldwell.

Superimposed birefractory plates. L. H. Adams and R. M. Waxler.

A self-calibrating instrument for measuring conductance at radio frequencies. L. E. Huntley.

Exact inductance equations for rectangular conductors with applications to more complicated geometries. C. Hoer and C. Love.

Common volume of two intersecting cylinders. J. H. Hubbell.

Steady-state heat conduction in an exposed exterior column of rectangular cross section. B. A. Peavy.

**Radio Sci. J. Res. NBS/USNC–URSI, 69D, No. 4 (Apr. 1965), $1.00.**

Waves in Plasma Papers

Dispersion of waves in a cold magnetoplasma from hydromagnetic to whistler frequencies. H. G. Booker and R. B. Dyce.

Study on the guiding mechanism of whistler radio waves. S. Adachi.

Electromagnetic waves along an infinitely long and thin conducting wire in a magneto-ionic medium. Y. Mushiake.

Use of the phase-integral method to determine the reflection properties of a stratified ionosphere. C. Altman.

*E*-mode propagation in a plane-stratified plasma. P. Hirsch and J. Shmoys.

Radiation from an infinite axial slot on a circular cylinder clad with magnetoplasma. P. de Marchin and G. Tyras.

Index of refraction surfaces for plasma waves. T. Yeh and M. H. Cohen.

Impedance of a short dipole in a compressible plasma. K. G. Balmain.

Waves circulating around a rigid cylindrical obstacle in a compressible plasma. J. R. Wait.

Wave propagation in a two component warm plasma. S. R. Seshadri.

Harmonic currents excited by an electromagnetic wave in a plasma. L. Wetzel and T. W. Tang.

Excitation of acoustic waves in plasmas. W. A. Saxton. (See above abstracts.)

Wave interaction in oxygen magnetoplasmas. K. V. Narasinga Rao. (See above abstracts.)

Regular Contributions

Test of the constancy of the velocity of electromagnetic radiation in high vacuum. P. Beckmann and P. Mandics. (See above abstracts.)

Signal degeneration in laser beams propagated through a turbulent atmosphere. P. Beckmann.

High frequency backscatter from the earth measured at 1000 km altitude. R. C. Chia, A. K. Fung, and R. K. Moore.

Observation of NPG VLF transmissions at Tracy, Calif., during path equinox. G. B. Carpenter and A. L. Whitson.

Small magnetic toroid antenna imbedded in a highly conducting half space. G. R. Swain.

**Radio Sci. J. Res. NBS/USNC–URSI, 69D, No. 5 (May 1965), $1.00.**

On electromagnetic radiation from a magnetic dipole with arbitrary orientation embedded in a lossless magneto-ionic medium. H. Motz.

A systematic study of the radiation patterns of a dipole in magnetoplasma based on a classification of the associated dispersion surfaces. R. Mittra and G. L. Duff.

Propagation of vertically polarized electromagnetic waves in a horizontally stratified magnetoplasma. R. Burman and R. N. Gould.

A note concerning the reflection of waves in inhomogeneous layers with asymmetric profiles. R. Burman.

On the terrestrial propagation of ELF and VLF waves in the presence of a radial magnetic field. J. Galejs.

Electron density profiles in cylindrical plasmas from microwave refraction data. B. A. Aničin.

Study of the waves supported by a warm plasma slab. P. R. Caron.

Transmission and reflection of electromagnetic waves by a hot plasma. E. C. Taylor. (See above abstracts).

Radiation from electrons in a magnetoplasma. H. B. Liemohn.

Radiation from a uniformly moving charge in an anisotropic, two component plasma. S. R. Seshadri and H. S. Tuan.

---

Sound insulation of wall, floor, and door constructions, R. D. Berendt and G. E. Winzer, NBS Mono. 77, (Nov. 30, 1964), 40 cents. Consolidated Supplement to Building Materials and Structures Report 144 (Supersedes Supplements 1 and 2 of BMS Report 144).

Legibility of alphanumeric characters and other symbols I. A permuted title index and bibliography, D. Y. Cornog, F. C. Rose, and J. L. Walkowicz, NBS Misc. Publ. 262–1, (Dec. 15, 1964), 60 cents.

Radio path length stability of ground-to-ground microwave links, M. C. Thompson, Jr., and H. B. Janes, NBS Tech. Note 219, (Nov. 15, 1964), 45 cents.

An atlas of VLF emission spectra observed with the "Hiss recorder", J. A. Koch and V. C. Edens, NBS Tech. Note 226, (Nov. 13, 1964), 40 cents.

VHF ionospheric scatter system loss measurements European-Mediterranean area, V. H. Goerke and O. D. Remmler, NBS Tech. Note 230, (Dec. 25, 1964), 40 cents.

Disclosures on various subjects; a plumbing vent manifold, a microadjuster, a glass joint or stopcock, and a miniature puller, ed., D. Robbins, NBS Tech. Note 253, (Nov. 30, 1964), 10 cents.

Effect of electrical fields in the gamma radiolysis of propane, P. Ausloos and R. Gorden, Jr., J. Chem. Phys. **41,** No. 5, 1278–1284 (Sept. 1, 1964).

Mass spectrometric investigation of the yttrium chlorine surface reaction, J. D. McKinley, J. Chem. Phys. **49,** No. 9, 2914–2817 (Nov. 1, 1964).

Kinetics of the acid-catalyzed hydrolysis of acetal in dimethyl sulfoxide-water solvents at 15, 25, and 35°, R. K. Wolford, J. Phys. Chem. **68,** No. 11, 3392–3398 (1964).

Simple arc devices for spectral excitation in controlled atmospheres, M. Margoshes and B. F. Scribner, Appl. Spectry. **18,** No. 5, 154–155 (1964).

Collision-induced microwave absorption in compressed gases. III. $CO_2$-foreign-gas mixtures, A. A. Maryott and S. J. Kryder, J. Chem. Phys. **41,** No. 6, 1580–1582 (Sept. 1964).

Making precision measurements of zener diode voltages, W. G. Eicke, Jr., IEEE Trans. Commun. Elec. **83,** No. 74, 433–438 (Sept. 1964).

Ethylene-propylene copolymers: crystallinity, infrared and creep studies, F. J. Linnig, E. J. Parks, and L. A. Wood, J. Appl. Polymer Sci. **8,** 2645–2651 (1964).

The National Bureau of Standards, E. L. Graminski, Capital Chemist **14,** No. 9, 2778–2781 (Dec. 1964).

Sampling and statistical design, W. J. Youden (Proc. Symp. Environmental Measurements, Cincinnati, Ohio, Sept. 4, 1963), Public Health Service No. 999–AP–15, pp. 35–39 (July 1964).

Plastics and the dental market, G. M. Brauer, Plastics World **12,** 12 (Oct. 1964).

NMR studies of asymmetric ethanic rotators: 1,2-disubstituted propanes, H. Finegold, J. Chem. Phys. **41,** No. 6, 1808–1818 (Sept. 15, 1964).

Triplet–state energy transfer from acetone to aliphatic aldehydes in the gas phase, R. E. Rebbert and P. Ausloos, J. Am. Chem. Soc. **86,** 4803–4807 (1964).

The needs of the statistical engineering programs of the National Bureau of Standards, C. Eisenhart, Proc. 9th Conf. Design of Experiments in Army Research Development and Testing, Directorate of Research and Development, U.S. Army Missile Command, Redstone Arsenal, Ala., Oct. 23–25, 1963, ARO–D Report 64–2 (1964).

Impact parameter treatment of vibrational excitation, F. H. Mies, J. Chem. Phys. **41,** No. 3, 903–904 (Aug. 1, 1964).

The inverse multiplier for abelian group difference sets, E. C. Johnsen, Can. J. Math. **16,** 787–796 (Sept. 4, 1964).

Studies on the tungsten-rhenium thermocouple to 2000 °C, D. B. Thomas, Proc. 18th Annual ISA Conf. and Exhibit, Sept. 9–12, 1963, Chicago, Ill., Preprint 57.3.63, pp. 57.3.63–1–57.3.63–9 (1963).

Gas-phase photolysis of methyl radicals with added organic compounds, R. D. Doepker and D. Ausloos, J. Chem. Phys. **41,** No. 6, 1865–1871 (Sept. 15, 1964).

18-cm spectrum of OH, H. E. Radford, Phys. Rev. Letter **13,** No. 17, 534–535 (Oct. 26, 1964).

Low temperature magnetic transitions in lanthanon trichlorides, Physics Letters **12,** No. 1, p. 5 (Sept. 1, 1964).

An investigation of plasma boundaries with electromagnetic surface waves, H. W. Wassink and A. J. Estin, J. Appl. Phys. **35,** 2795–2800 (Oct. 1964).

Effect of particle shape and size distribution in a reinforced polymer, R. L. Bowen, J. Am. Dental Assoc. **69,** 481–495 (Oct. 1964).

Growth of oxalic acid single crystals from solution: solvent effect on crystal habit, J. L. Torgensen and J. Strassburger, Science **146,** No. 3640, 53–55 (Oct. 2, 1964).

Investigation of the hydraulics of horizontal drains in plumbing systems, R. S. Wyly, NBS Mono. 86 (Dec. 18, 1964), 35 cents.

Aluminum nails, CS263–64 (Nov. 1, 1964), 10 cents.

On the pictorial structure of chinese characters, B. K. Rankin, III, W. A. Sillars, and R. W. Hsu, NBS Tech. Note 254 (Jan. 4, 1965), 30 cents.

Characteristics of the earth-ionosphere waveguide for VLF radio waves, J. R. Wait and K. P. Spies, NBS Tech. Note 300 (Dec. 30, 1964), 50 cents.

National standard reference data system, Plan of operation, E. L. Brady and M. B. Wallenstein, NSRDS–NBS1 (Dec. 30, 1964), 15 cents.

Error bounds for asymptotic expansions, with an application to cylinder functions of large argument, F. W. J. Olver, Book, Asymptotic Solutions of Differential Equations and Their Applications, ed. C. H. Wilcox, pp 163–183 (John Wiley & Sons, Inc., New York, N.Y., 1964).

Spectral study of active nitrogen flames exhibiting CN "tail" bands, R. L. Brown and H. P. Broida, J. Chem. Phys. **41,** No. 7, 2053–2060 (Oct. 1, 1964).

Note on the partition functions, N. Newman, Am. Math. Mo. **71,** No. 9 (Nov. 1964).

Automatic optical design, O. N. Stavroudis, Book, Advances in Computers **5,** 227–252 (Academic Press Inc., New York, N.Y., 1964).

Free-field correction for condenser microphones, W. Koidan and D. S. Siegel, J. Acoust. Soc. Am. **36,** No. 11, 2233–2234 (Nov. 1964).

Infrared spectrum of HCO, D. E. Milligan and M. E. Jacox, J. Chem. Phys. **41,** No. 10, 3032–3036 (Nov. 1964).

A magnetic fixed point for thermometry below 1 °K, J. C. Eisenstein, R. P. Hudson, and B. W. Mangum, Appl. Phys. Letters **5,** No. 11, 231 (Dec. 1, 1964).

Continuum description of a high temperature plasma, L. S. Klein and J. L. Jackson, Proc. VI Intern. Conf. Ionization Processes in Gases, Paris, France, 1963, II, No. 11, 215–216 (June 1964).

Gas thermometer, L. A. Guildner, Encyclopaedic Dictionary of Physics, pp. 405–406 (Pergamon Press, New York, N.Y., 1961).

Configurations $4f^2 6s$ and $4f^2 6p$ in doubly ionized Pr, N. Spector, J. Opt. Soc. Am. **54,** No. 11, 1359–1362 (Nov. 1964).

Photochemical changes in thin-layer chromatograms of polycyclic, aromatic hydrocarbons, M. N. Iniscoe, Anal. Chem. **36,** No. 13, 2505–2506 (Dec. 1964).

Photoelimination of ethylene from 2-pentanone, P. Ausloos and R. E. Rebbert, J. Am. Chem. Soc. **86,** No. 20, 4512 (Oct. 20, 1964).

Second dissociation constant of deuteriophosphoric acid in deuterium oxide from 5 to 50°. Standardization of *p*D scale, R. Gary, R. G. Bates, and R. A. Robinson, J. Phys. Chem. **68,** No. 12, 3806–3809 (Dec. 1964).

Some activities of the cooperative dental research between the Federal Government and the American Dental Association at the National Bureau of Standards, G. C. Paffenbarger, Ann. Dentistry **XXII,** No. 4, 111–126 (Dec. 1964).

Studies of the thicknesses of adsorbed glass finishes by ellipsometry, D. J. Tutas, R. R. Stromberg, and E. Passaglia, SPE Trans. **4,** No. 4, 1–7 (Oct. 1964).

The Statistical Analysis of Experimental Data, J. Mandel, Book, 410 pages (Interscience Publ., Inc., New York, N.Y., 1964).

Proton and fluorine NMR spectra of $HBF_2$, T. C. Farrar and T. D. Coyle, J. Chem. Phys. **41,** No. 9, 2612–2613 (Nov. 1, 1964).

Influence of radiant energy source on bitumen oxidation, K. G. Martin, J. Appl. Chem. **14,** No. 11, 514 (1964).

APS division of electron physics the first 20 years, L. Marton, Phys. Today, pp. 44–50 (Oct. 1964).

Liouville representation of quantum mechanics with application to relaxation, U. Fano (Proc. Lectures on the Many-Body Problems, 5th Intern. School of Physics, Ravello, Italy, Apr. 17–May 4, 1963), Book, Lectures on the Many-Body Problems **2,** 1–294 (Academic Press Inc., New York, N.Y., 1964).

Our measurement system and its future, R. D. Huntoon, Res./Develop. **16,** No. 1, 16–21 (Jan. 1965).

Fracture processes in polymeric solids, I. Wolock and S. B. Newman, Book, Fracture Processes in Polymeric Solids. Phenomena and Theory, ed. B. Rosen, ch. IIC, pp. 235–290 (Interscience Publ. Inc., New York, N.Y., Jan. 1965).

Which measure of precision? The evaluation of the precision of analytical methods involving linear calibration curves, F. J. Linnig and J. Mandel, Anal. Chem. **36,** No. 13, 25A–32A (Dec. 1964).

**Publications for which a price is indicated are available by purchase from the Superintendent of Documents, U.S. Government Printing Office, Washington, D.C., 20402 (foreign postage, one-fourth additional). Reprints from outside journals and the NBS Journal of Research may often be obtained directly from the authors.*



U.S. GOVERNMENT PRINTING OFFICE : 1965 OL—766–033

UNIVERSITY MICROFILMS
313 NORTH FIRST STREET
ANN ARBOR, MICHIGAN
SJR-A-OCT

UNITED STATES
GOVERNMENT PRINTING OFFICE
DIVISION OF PUBLIC DOCUMENTS
WASHINGTON, D.C. 20402

OFFICIAL BUSINESS

PENALTY FOR PRIVATE USE TO AVOID
PAYMENT OF POSTAGE, $300
(GPO)

JOURNAL OF RESEARCH of the National Bureau of Standards
A. Physics and Chemistry

Vol. 69A, No. 3 May–June 1965

## Contents

Page

Electronic structure and magnetic properties of the neptunyl ion. J. C. Eisenstein and M. H. L. Pryce. 217

Heats of transformations in bismuth oxide by differential thermal analysis. Ernest M. Levin and Clyde L. McDaniel. 237

Phase relations between iridium and the sesquioxides in air. S. J. Schneider, J. L. Waring, and R. E. Tressler. 245

Phase equilibrium relationships in the system $Gd_2O_3$–$TiO_2$. J. L. Waring and S. J. Schneider. 255

Acid-base behavior in 50.percent aqueous methanol: thermodynamics of the dissociation of protonated tris(hydroxymethyl) aminomethane and nature of the solvent effect. Maurice Woodhead, Maya Paabo, R. A. Robinson, and Roger G. Bates. 263

Observations of dislocations and surface features in corundum crystals by electron transmission microscopy. D. J. Barber and Nancy J. Tighe. 271

Low-frequency dielectric properties of liquid boric oxide. Kurt H. Stern.. 281

Mass spectrometric study of the effects of nitric oxide and other additives on "purified" active nitrogen. John T. Herron. 287

Synthesis and ring structure of 7-acetamido-7-deoxy-L-*galacto*-heptulose. Emma J. McDonald. 291

Publications of the National Bureau of Standards. 295

Library of Congress Catalog Card Number: 62–37059

For sale by the Superintendent of Documents, U.S. Government Printing Office, Washington, D.C., 20402. Price 70 cents (single copy)
Subscription price: $4 a year; 75 cents additional for foreign mailing.
UNITED STATES GOVERNMENT PRINTING OFFICE, WASHINGTON : 1965